CHEMICAL LOOPING FOR SYNGAS & HYDROGEN PRODUCTION WITH PARALLEL CO_2 ACTIVATION

by

Amey Sudhir More

Bachelor of Chemical Engineering, Institute of Chemical Technology, 2012

Submitted to the Graduate Faculty of

Swanson School of Engineering in partial fulfillment

of the requirements for the degree of

Doctor of Philosophy

University of Pittsburgh

2016

UNIVERSITY OF PITTSBURGH

SWANSON SCHOOL OF ENGINEERING

This dissertation was presented

by

Amey Sudhir More

It was defended on

November 10, 2016

and approved by

Susan Fullerton, Ph. D., Assistant Professor
Department of Chemical & Petroleum Engineering

Gerald Meier, Ph.D., Professor
Department of Mechanical Engineering & Materials Science

Giannis Mpourmpakis, Ph. D., Assistant Professor
Department of Chemical & Petroleum Engineering

Dissertation Director: Götz Veser, Ph.D., Professor,
Department of Chemical & Petroleum Engineering

CHEMICAL LOOPING FOR SYNGAS PRODUCTION WITH PARALLEL CO_2 ACTIVATION

Amey Sudhir More, PhD

University of Pittsburgh, 2016

The anticipated rise in global population and the rapidly growing economies of the developing world will dramatically increase the demand for consumer products, which are derived mostly from commodity chemicals. While the abundant natural gas (>95% CH_4) reserves can potentially enable bulk chemical production, all commercial routes for methane (CH_4) upgrading require its conversion to syngas (mixture of $CO+H_2$) as a first step. Not only are current syngas production technologies highly energy and capital intensive, but they also result in large CO_2 emissions. Overall, rising environmental concerns, increase demand for bulk chemicals and availability of abundant natural gas reserves together motivate the need to develop alternative processes for syngas production with CO_2 utilization.

‘Chemical Looping Combustion’ is a clean combustion technology, which enables fossil fuel combustion with inherent CO_2 capture based on the cyclic oxidation and reduction of an oxygen carrier. While most efforts in chemical looping (CL) are focused on combustion, we demonstrate the application of the “CL principle”—the periodic oxidation and reduction of a metal oxide to couple two independent redox reactions—to the activation of CO_2 via reduction to CO (a chemical feedstock) and upgrading of CH_4 to syngas or hydrogen.

In this work, we investigate and compare CO_2 activation via CL in two different operating modes: In the first scheme, CO_2 reduction is coupled with CH_4 oxidation by using mixtures of Fe and Ni (as alloys or simple physical mixtures) to produce CO and syngas product streams. In the second operating scheme, monometallic Ni carriers are utilized to catalytically crack CH_4, producing pure H_2 streams. The solid carbon deposits are then burnt off with CO_2, overall producing separate CO and H_2 product streams. Our investigations demonstrate the potential of CO_2 as a “soft” oxidant which enables selective oxidation reactions in all the configurations, and thereby establish the potential of chemical looping processes for efficient syngas production with CO_2 utilization.

TABLE OF CONTENTS

LIST OF FIGURES

PREFACE

This work would not be possible without the fatherly tutelage of Dr. Veser. The comprehensive training, unwavering support and the nourishing research environment you have provided over the years has contributed immensely towards my all-round development. You have persistently encouraged an inquisitive, methodical and judicious approach to research, which has taught me to think clearly, plan effectively and execute systematically. I am confident that the valuable lessons you have imparted will serve me well beyond the confines of scientific research.

I want to thank my committee members– Dr. Susan Fullerton, Dr. Gerald Meier and Dr. Giannis Mpourmpakis, for taking out valuable time to employ their vast and diverse expertise for guiding this research.

Finally, I would like to acknowledge all my lab mates, undergraduates, friends, and family for their support!

1.0 INTRODUCTION

Selective catalytic oxidation of hydrocarbons directly contribute to the production of a wide variety of indispensable consumer products and hence represent nearly 25% of the value produced by all catalytic process worldwide[1]. With the world population expected to increase ~30% by 2050[2] along with the rapidly growing economies around the world, it is anticipated that the demand for consumer products would rise substantially. Reports suggest that the per capita chemical sales by 2050 would be ~$2000– a surge of almost 300% as compared to 2012[3]. Naturally, oxidation processes have received immense attention from industrial as well as academics researchers over the past 50 years, with the efforts directed towards improving overall process yields and selectivity. Crude-oil has been the traditional feedstock for bulk chemical production. However, the price volatility of crude oil as well as dependence on foreign imports, has prompted a need to utilize cheap, economically stable and locally available alternatives. Advances in drilling technologies have made large reserves of natural gas economically accessible in the U.S. Although the actual amounts of recoverable gas based on ecological concerns is up for debate, it is clear that the readily available reserves of natural gas have initiated significant interests in developing the infrastructure (pipelines, downstream conversion assets, storage etc.) for utilization of this resource. Natural gas consists mainly of methane (>95%) along-with higher alkanes (C_2-C_4), viz. ethane, propane and butane. In the absence of commercially proven technologies that can directly convert methane to end chemicals, all routes for methane upgrading, currently proceed via its conversion to syngas (a mixture of CO & H_2) as a first step, and from there on, to a wide variety of chemicals and intermediates (Figure 1). Currently, syngas is mainly produced via steam reforming of methane (SRM): $CH_4 + H_2O = CO + 3H_2$. While SRM is a mature technology, it requires huge capital investments and large scale operations[4] for economies of scale benefits. Moreover, the process energy costs contribute nearly 70% to the overall production costs and resulting in large amounts of CO_2 emissions[5]. By now it is well established that anthropogenic CO_2 emissions resulting from a combination power generation as well as inefficient chemical production, have resulted in atmospheric CO_2 levels consistently being over ~400ppm[6]. Overall, the anticipated demand in bulk chemical production, the stricter environmental regulations on commercial processes and the flexibility to utilize locally available natural gas resources, together motivate the development of commercially viable, atom-efficient and carbon neutral process for conversion of methane to syngas.

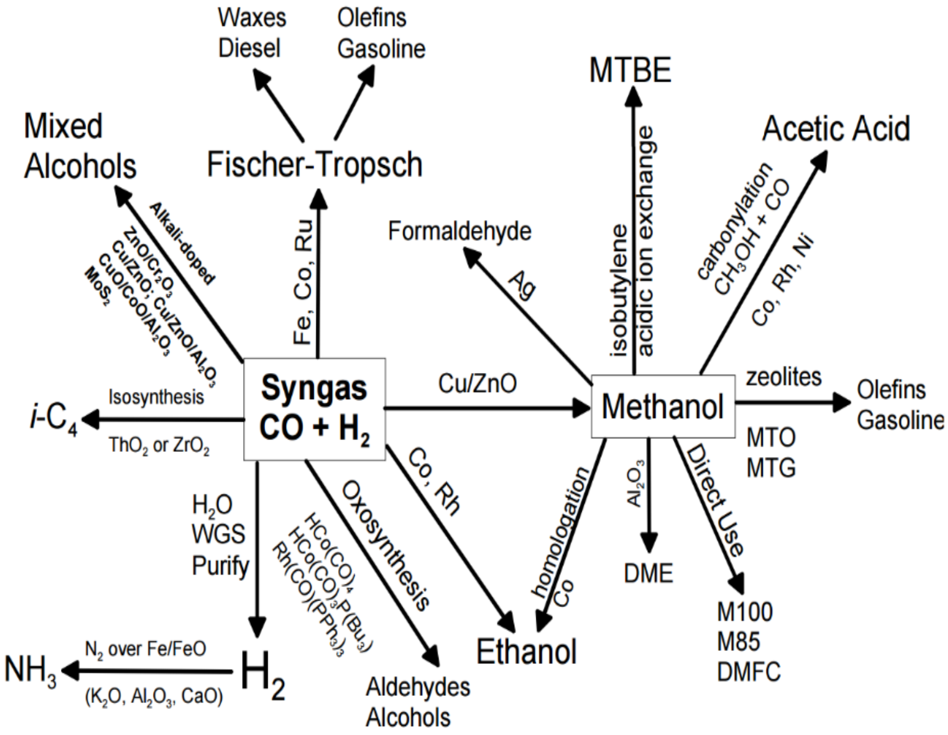

Figure 1. Routes to syngas conversion to a variety of end-chemicals[7]

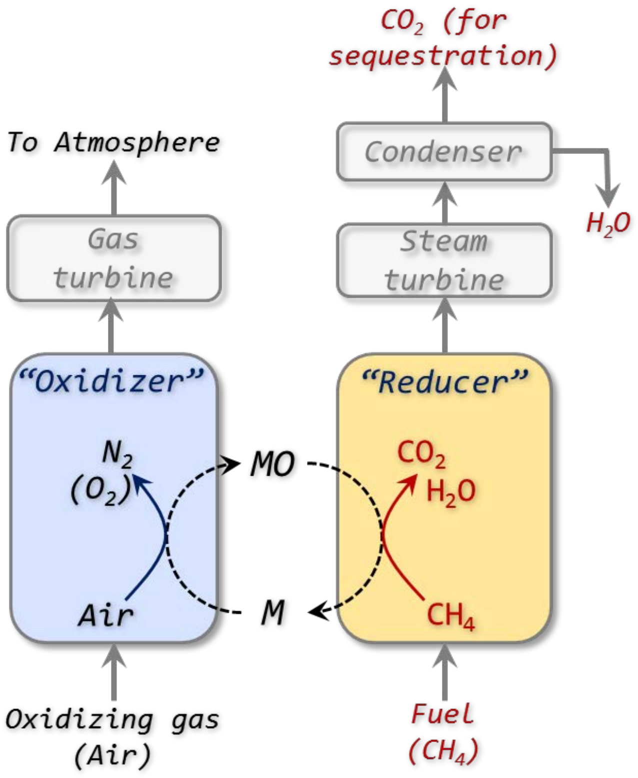

Figure 2. Schematic of chemical looping combustion (CLC)

Chemical Looping Combustion (CLC)[8-12] is a rapidly emerging technology for clean, efficient and robust combustion of fossil fuels (Figure 2). The process utilizes an oxygen carrier, typically a metal oxide, at high temperatures to combust the fuel in a "reducer reactor". The reduced oxygen carrier is then oxidized in an "oxidizer reactor" with air and recycled back to the "reducer"; the term "chemical looping" thus derived from the carrier recycle loop. The resultant product gas stream from the reducer is composed mainly of CO_2 and H_2O allowing for easy separation of CO_2 through simple condensation to yield sequestration-ready CO_2 streams. Furthermore, the separation of the combustion into two distinct yet coupled processes, viz. oxidation and reduction, avoids direct contact between air and fuel thus eliminating problems like NO_x generation which are typical for conventional combustion. Overall, CLC elegantly offers inherent separation of a greenhouse gas: CO_2, while utilizing existing industrial technologies (fluidized bed, fixed bed reactor etc.) without major efficiency penalties as compared to its competitor: oxyfuel combustion. It is important to note that chemical looping does not alter the overall reaction (which is fuel combustion) or the overall reaction enthalpies. The overarching principle of chemical looping is primarily: a convenient "break-up" of a process without affecting the overall process itself, thereby improving the net exergy (or usable energy) extracted from the overall process; Exergy losses typically occur when a gas mixture needs to be separated into its components.

1.1 CHEMICAL LOOPING COMBUSTION

The surge in CLC activities over the past decade was mainly due to the recent focus on developing technologies that offer CO_2 capture without significant energy penalties. Yet, the concept behind CLC: certain metals can take up oxygen from a gas, had been demonstrated by the French chemist Antoine Lavoisier in the 18th century, albeit towards a different goal– to prove mass is always conserved in a reactive process! On the other hand, the Lavoisier-Meusnier iron-steam process established the practical aspects of this finding by producing hydrogen by reacting steam with iron at 600°C. Messerschmidt (1911) and Hurst (1939) successfully operated large scale hydrogen production plants after incorporating periodic operation, by recycling the oxidized iron after reduction with natural gas. However, these initial demonstrations of chemical looping were not able to compete with steam reforming of methane due to availability and stability of oxygen carriers (naturally occurring iron ores).

While the initial interest in chemical looping was exclusively focused on combustion, reforming and partial oxidation via chemical looping (CLR and CLPOM, respectively) has started to attract some attention over the past five years. CLR incorporates CO_2 and H_2O along with CH_4 into the reducer feed, to facilitate syngas production via the steam reforming and dry reforming reactions over Ni carriers. Alternatively, the process feeds are kept unchanged from the original CLC process, but the degree of fuel oxidation is controlled either via use of appropriate carriers or via the ratio of fuel-to-oxygen carrier such that incomplete, i.e. partial oxidation to synthesis gas ($CO + H_2$) results (CLPOM). For example, Ryden et al. studied the use of Ni-based carriers for partial oxidation and steam reforming of methane in a chemical looping process using a CFB configuration[13]. They report near complete methane conversion, albeit at operation with C/O ratios well below the stoichiometric ratio for partial oxidation, resulting in low syngas selectivities. In a follow-up study, they demonstrated that the carrier formulation has significant impact on activity and selectivity, but all Ni-based carriers were plagued by coke formation, which required steam addition to mitigate the problem[14]. Similar problems with coking of Ni-based carriers have been reported before for CLC as well, where again large addition of steam ($H_2O:CH_4 = 2$) was proposed as mitigating strategy (at the expense of process efficiency[15]). Pröll et al. recently also used a Ni-based carrier to produce syngas from methane; while they do not report on coking problems, their syngas selectivities were poor with <60% H_2 selectivity even at optimal conditions[16]. Overall, these studies support the feasibility of a CL-based syngas production process, but point out a key issue: the oxygen carriers showed insufficient activity, selectivity, and/or coking resistance for partial oxidation of methane. The current project aims to fill this gap by developing highly reactive, selective and rationally designed oxygen carries for syngas production.

1.2 DRY REFORMING OF METHANE

Dry reforming of methane (DRM): $CH_4 + CO_2 = 2CO + 2H_2$ utilizes both CO_2 as well as CH_4 while producing the desired chemical intermediate i.e. syngas. Even though, DRM is an endothermic process (ΔH_R = 248kJ/mol), it has potential to be used in sustainable energy production in solar-chemical energy transmission systems, where the heat from the renewable resources like the sun can be used to drive the endothermic reaction forward.

Initial studies conducted by Fischer & Tropsch on dry reforming of methane conducted in the early 20th century suffered from severe deactivation from carbon formation. Subsequent work[17] by Reitmeier et al., analyzed equilibria for the multiple gas-phase reactions occurring in the system viz. Boudouard reaction: $2CO = CO_2 + C$ (ΔH_R = 72 kJ/mol); methane decomposition: $CH_4 = C + 2H_2$ (ΔH_R = -171 kJ/mol); water gas shift: $H_2O + CO = CO_2 + H_2$ (ΔH_R = -41.2 kJ/mol), and their reverse reactions to identify suitable conditions– temperature and reactant ratio, necessary for carbon free operation in a generalized $H_2O/CO_2/CH_4$ system. From the analysis of the reaction free energies, Wang et al. proved that for $CH_4:CO_2 = 1$, carbon formation was thermodynamically inevitable below ~900°C and 1 atm pressure[18]. Nematollahi et al. confirmed this observation and further established that reactant conversion and product yields drop significantly with increasing pressures[19]. Although, it is possible theoretically to operate at conditions with minimal carbon formation, practical considerations dictate addition of H_2O for all dry reforming applications.

Research conducted over the past fifty years attempted to develop stable and coke-resistant dry reforming catalysts with the focus mainly being on Ni as an active component[20]. Rostrup-Nielsen first reported a catalyst with a spinel framework of Al and Mg and some basic Mg remaining on the surface, acting as a promoter in activation of CO_2 and promoting oxidation of surface carbon[21]. This concept of using basic promoters was employed by several researchers although, the mechanism behind this activation was not established yet. To tackle the problem from a different angle, noble metal catalysts like Pt, Rh and Ru, which are active towards dry reforming but have a much lower tendency for coke formation were proposed [22-24]. Since these catalysts were quite expensive for a commercial scale process, the noble metals were alloyed with Ni to improve the stability without greatly affecting the cost.

1.3 PERIODIC PROCESSES FOR DRY REFORMING OF METHANE

Gilliland et al. demonstrated dry reforming of methane in a periodically operated process for the first time more than fifty years ago using Cu based oxygen carriers[25]. The process involved contacting CH_4 with a controlled amount of oxygen (oxygen carriers) such that the C:O ratio was ~ 1, producing CO_2 and H_2O as a first step, followed by the subsequent conversion of these products to syngas via reforming (dry and steam reforming) with the unconverted CH_4 over metallic Cu in the second step. The process was then repeated after oxidation with air. While the generation one of the reactants (CO_2) for dry reforming during the process was a unique configuration, typical problems in conventional dry reforming were only partially addressed; The first step (in an ideal scenario) produces a mixture of gases: CO_2, H_2O and unconverted CH_4, which undergo reforming reactions over a metal catalyst: Cu. It is clear that all the usual problems of dry reforming: carbon deposition, equilibrium limited process and poor selectivity control, would present themselves despite the periodic nature of the process.

Recently, Najera et al. demonstrated an alternative approach to CO_2 activation by incorporating it as an oxidant (instead of air) in the chemical looping configuration and thus enabling its transformation to CO[26]. The reducer utilized H_2 as a fuel such that the overall process: $CO_2 + H_2 = CO + H_2O$, was a demonstration of the reverse water gas shift reaction. While this initial study did not attempt dry reforming of methane ($CH_4 + CO_2 = 2CO + 2H_2$), it served as a harbinger for implementation of the dry reforming process by chemical looping concept (CLDR) – two reactants (H_2 and CO_2) undergoing separate reactions which are connected by a species (oxygen) carrier. More importantly, based on a thorough thermodynamic screening, this work identified iron as a potential metal suitable for a process that uses CO_2 as an oxidant. Huang et al. demonstrated the concept utilizing CH_4 as a fuel to produce CO and H_2O as the overall products by using bimetallic Fe-Ni carriers. Galvita et al. used a physical mixture of Ni catalyst and Fe based oxygen carriers for CO_2 activation to CO in the oxidizer while using a mix of CO_2 and CH_4 (typical for a biogas plant), as fuel in the reducer[27]. Highly functional nanomaterials like Fe-SiO_2 core-shell structures[28], Mg-Fe-Al-O spinels[29] and La based perovskites[30] were also reported with the primary goal of CO_2 activation to CO.

1.4 PROJECT OBJECTIVES AND LAYOUT

Briefly, the current work utilizes the chemical looping approach to: 1) employ lattice oxygen for superior control over partial oxidation reactions; 2) appropriate the chemical inertness of CO_2 for controlled replenishment of the lattice oxygen while enabling its transformation to CO; and 3) demonstrate the principle of “carrier-coupled” processes beyond the current realm of “oxygen” carriers for oxidation processes, thereby advocating the flexibility of this concept for overall process improvement.

The overall research is laid out in a chapter-wise manner, with individual chapters written in a standard scientific research article format i.e., containing introduction, experimental methods, results and discussion, and conclusions (chapters 2-5). Finally, a brief summary encompassing the complete work (chapter 6) and an outlook exploring the future directions of this work (chapter 7) is provided.

2.0 IRON-NICKEL ALLOYS FOR CARBON DIOXIDE ACTIVATION BY CHEMICAL LOOPING DRY REFORMING OF METHANE

The content of this chapter is taken from More et. al., Iron-Nickel Alloys For Carbon Dioxide Activation By Chemical Looping Dry Reforming Of Methane, *Energy Technology*. 2016;*10*(14):1147-1157.

2.1 INTRODUCTION

Dry reforming of methane is conceptually the simplest process that combines CO_2 utilization with methane valorization via the formation of synthesis gas, a widely used feedstock in the chemical industry for the production of synthetic fuels and commodity chemicals[20,31-33]. Dry reforming of CH_4 to produce syngas ($CO+H_2$; R1) has received limited interest industrially in the absence of incentives for CO_2 utilization, since it suffers from catalyst coking issues and produces a H_2-lean syngas with a H_2:CO ratio of 1[18,34]. Autothermal reforming (ATR) and catalytic partial oxidation of methane (CPOM) avoid the coking issues and produce a syngas with more desirable, higher syngas ratios. However, they require an oxygen separation plant which constitutes a major fraction of the overall syngas plant cost (~40%)[35] and do not allow utilization of CO_2.

Dry Reforming: $CH_4 + CO_2 = 2CO + 2H_2$ (R1)

Oxidizer: $Me + CO_2 = MeO + CO$ (R2)

Reducer: $CH_4 + MeO = CO + 2H_2 + Me$ (R3)

Net reaction: $CH_4 + CO_2 = 2CO + 2H_2$ (R4)

"Chemical looping" is an interesting alternate technology for methane conversion which has recently gained much attention as a clean combustion technology (Figure 3a)[8,9,11,12,36,37]. In this "combustion configuration", chemical looping utilizes an oxygen carrier, typically a metal oxide, to combust the fuel in a "reducer reactor" at high temperatures. The resultant product gas stream, composed mainly of CO_2 and H_2O, allows separation of CO_2 through simple condensation of water to yield sequestration-ready CO_2 streams. The reduced oxygen carrier is then re-oxidized with air in an "oxidizer reactor" and recycled back to the reducer reactor. Chemical looping combustion (CLC) thus offers an elegant and efficient path towards carbon capture with minimal energy penalty. However, it does not enable utilization of the captured CO_2 stream.

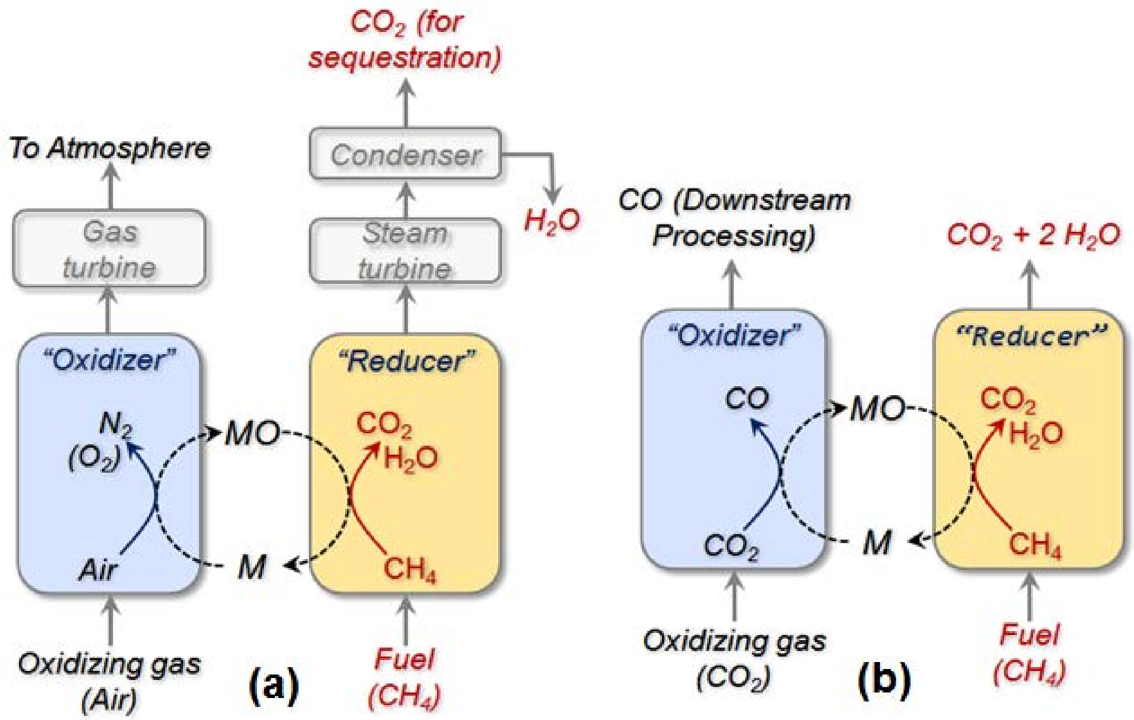

Figure 3. Chemical looping processes: a) combustion and b) dry reforming

We have recently proposed a closely related process, "chemical looping dry reforming" (CLDR;Figure 3b)[26] which utilizes the same approach as CLC and applies it to dry reforming of methane by using CO_2 as oxidant in the "oxidizer reactor". If the oxidation of methane in contact with the oxygen carrier is furthermore carefully controlled, the reducer reactor produces a syngas stream and hence enables simultaneous production of syngas with activation of CO_2 via reduction to CO (R3), depending on the metal present. Although the net reaction (R4) produces syngas at the same stoichiometric ratio as conventional dry reforming (R1 vs R4), the effluent of the reducer is at a syngas ratio of H_2:CO = 2 (desired for typical downstream processes, such as

Fischer-Tropsch or methanol synthesis) with the "excess CO" obtained separately as a concentrated stream at the oxidizer exit.

We have previously conducted a systematic study in which we screened a broad range of metals and identified Fe as the most suitable candidate for this process due to its ability to reduce CO_2, and then demonstrated the feasibility of the process using Fe-based oxygen carrier materials and H_2 as model fuel[26]. Subsequent work by our group and others utilized this property further by developing highly functional nanomaterials like Fe-SiO_2 core-shell structure[28], Mg-Fe-Al-O spinels[29] and La based perovskites[30] with the primary goal of CO_2 activation to CO. However, Fe-based carriers show poor reactivity with methane, hampering the application of this process to methane valorization[38-41]. In contrast, Ni is a well-known catalyst for C-H bond cleavage[32,33,42-45]. We have recently shown that alloying Fe with Ni—resulting in the creation of active Ni sites for CH_4 activation embedded in an iron oxide matrix—can strongly improve the reactivity of the carrier towards CH_4, as demonstrated both for CH_4 conversion via chemical looping combustion[41] and chemical looping partial oxidation[46]. While in these cases the high activity of Ni towards methane activation was utilized to "activate" a carrier composed predominantly of cheap and non-toxic Fe, it seems reasonable to assume that the same concept should be applicable to the CLDR process, where the ability of Fe to capture oxygen via reduction of CO_2 would complement the high activity of Ni for methane conversion. This hypothesis is further supported by prior reports that similar alloys enable catalytic CO_2 decomposition, producing CO or C depending on operating conditions[27,47-50]. Thus, we hypothesized that alloyed Fe-Ni carriers should show strong reactivity with both CH_4 as well as CO_2 and hence enable an efficient CLDR process.

The present work aimed to validate this hypothesis by evaluating the performance of alloyed Fe-Ni oxygen carriers in chemical looping dry reforming. Ceria (CeO_2) is used as carrier support based on its reducible nature which had been shown to enable accelerated redox kinetics and enhanced carrier utilization[42]. Since Fe has multiple oxidation states with varied oxygen availability and thus offers tunable product selectivities with CH4 as a fuel[46], we furthermore employ the inherently slow(er) oxidation kinetics of CO_2 as oxidant to control the carrier oxidation state in order to "fine-tune" the syngas selectivity in the subsequent methane conversion, while simultaneously activating CO_2 via production of CO, a useful and reactive chemical feedstock.

2.2 EXPERIMENTAL SECTION

2.2.1 Material Synthesis

Focus of the carrier synthesis was on a simple, inexpensive and scalable synthesis approach. The alloy carriers were therefore synthesized via a simple wet-impregnation approach. Appropriate quantities of the metal nitrate precursors, $Fe(NO_3)_3.9H_2O$ and $Ni(NO_3)_2.6H_2O$ (both 99+%, Sigma Aldrich), were dissolved in 1mL ethanol. Commercially available CeO_2 powder (99+%, Alfa Aesar) was added to the solution, stirred continuously for 2 hours and dried overnight (90^{o}C). The resulting solid cake was ground and then calcined in air (0.2 SLM) at 800^{o}C for 2hr. In addition to the two monometallic carriers (Fe and Ni), alloy carriers were synthesized with 40 wt% total metal loading at three different Fe:Ni ratios, 67:33, 88:12 and 98:2 (designated as $Fe_{0.67}Ni_{0.33}$, $Fe_{0.88}Ni_{0.12}$ and $Fe_{0.98}Ni_{0.02}$).

2.2.2 Characterization

X-Ray Diffraction Characterization: To confirm the phases present, the synthesized carriers were first analyzed via powder X-Ray diffractometry (Bruker D8) operating at 40kV and 40mA with Cu Kα radiation (λ=1.5418 Å). The data was recorded between 2Θ values of 20^o and 90^o with a scanning rate of 3.5^o/min. The XRD pattern was smoothed with a FFT filter. The phases were identified using the JCPDS database. Average crystallite size was calculated using the Scherrer equation.

Surface Area and Pore Volume: BET (Brunauer-Emmett-Teller) surface area determination was conducted via Nitrogen adsorption/desorption in a Micrometrics ASAP 2020 gas adsorption analyzer. The samples were pretreated by degassing under vacuum for 2hr at 200^oC. All the samples considered in the study had low surface areas of < 5 m^2/g as expected due to initial sintering of the materials.

Electron Microscopy: A High Resolution-Transmission Electron Microscopy (HR-TEM) JOEL JEM-2100F was used to image the particles and conduct EDAX mapping. Bulk metal weight percentages and metal dispersion of the synthesized samples were confirmed by Energy Dispersive X-Ray Analysis (EDAX) performed using an Oxford INCA EDS system attached to a JSM-6510LV SEM.

2.2.3 Reactivity tests

Solid-Phase Conversion: Carrier conversion was determined in a Thermo-Gravimetric Analyzer (SDTQ600, TA instruments). 10-15mg of the carrier powder were loaded into the instrument. The temperature was ramped up to the reaction temperature at 100^oC/min and then held there isothermally for the experimental duration. The gases used were: N_2 (Grade 5, 100sccm), Ar (Grade 5, 20sccm), H_2 (Grade 2, 20sccm) CH_4 (Grade 2, 5sccm) and CO_2 (Grade 2, 20sccm). The carrier gas (N_2) is flown continuously throughout the experiment. The reactive gases H2/CH_4 and CO_2, are used for the reduction and oxidation of the carrier respectively. The purge gas (Ar) is used to flush the system between consecutive reduction and oxidation cycles. For comparison between the various carriers carrier conversion was defined as follows:

$$Carrier\ Conversion = \frac{Sample\ Weight - Reduced\ Weight}{Oxidized\ Weight - Reduced\ Weight}$$

Eq. (1)

The different oxidation states of the sample were calculated by a simple mass balance from the oxidized weights.

Gas-Phase Reactivity: Conversion of the fuel (CH4) and product selectivity was determined using a fixed bed reactor set-up. 100mg of the carrier was packed between two glass wool plugs in a horizontal quartz tube (1/4" ID) enclosed by a furnace (Thermo electron corporation-Lindberg/Blue M). The reactant gases were fed via mass flow controllers at the following flow rates: Ar (99.995%, 5 sccm as a reference for calculations flown throughout the experiment and 20 sccm as purge between cycles), CH_4 (99.995%, 1 sccm) CO_2 (99.999%, 1 sccm) and O_2 (99.999%, 1 sccm). The outlet gas concentrations were measured by a mass spectrometer (Pfeiffer Omnistar QMS 200) and the corresponding molar flow rates (ni) were calculated.

The selectivities and conversion of various gaseous products during the reduction half cycle were calculated using the following formulas:

$$X_{CH_4} = \frac{n_{CH_4,in} - n_{CH_4,out}}{n_{CH_4,in}} \qquad S_{H_2} = \frac{n_{H_2,out}}{n_{CH_4,in} - n_{CH_4,out}}$$

Eq. (2), (3)

$$S_{CO} = \frac{n_{CO_{out}}}{n_{CH_{4,in}} - n_{CH_4,out}} \qquad S_{CO_2} = \frac{n_{CO_{2,out}}}{n_{CH_{4,in}} - n_{CH_4,out}}$$

Eq. (4), (5)

To check the accuracy of the performed experiments, a carbon balance was performed and closed within 10% for all the reported experiments. Carbon balance:

$$n_{CH_{4,in}} = n_{CH_{4,out}} + n_{CO_{2,out}} + n_{CO_{out}} + n_{C_{out}}$$

Eq. (6)

$$n_{CH_{4,in}} = n_{CH_{4,out}} + n_{CO_{2,out}} + n_{CO_{out}} + 0.5 \times (n_{H_{2,out}} - 2n_{CO_{out}})$$

Eq. (7)

For the oxidation half cycle the conversion was calculated as:

$$X_{CO_2} = \frac{n_{CO_{2,in}} - n_{CO_2,out}}{n_{CO_{2,in}}}$$

Eq. (8)

The carbon balance closed within 10%.

2.3 RESULTS AND DISCUSSION

2.3.1 Carrier Characterization

The carriers were first analyzed in an X-Ray Diffractometer (XRD) to identify the phases present in the carriers as-synthesized (Figure 5). As expected, diffractions peaks for the CeO_2 support were detected for all three alloy compositions. For $Fe_{0.67}Ni_{0.33}$, (i.e. Fe:Ni = 2:1) only nickel ferrite $NiFe_2O_4$ is detected, i.e. both metals are only present as the stoichiometric alloy (oxide).

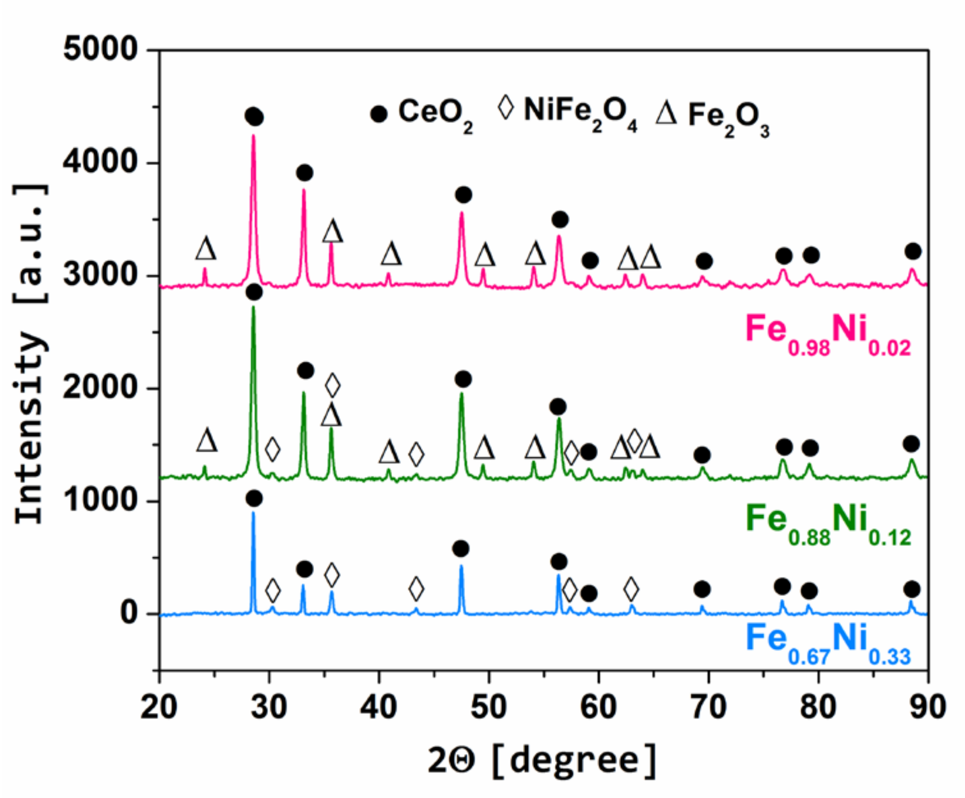

Figure 4. X-Ray Diffraction (XRD) patterns of the as-synthesized alloyed Fe-Ni carriers of varying Fe:Ni ratios denoting the phases formed for each case.

For $Fe_{0.88}Ni_{0.12}$, which contains an excess of Fe, Fe_2O_3 was detected in addition to the nickel ferrite phase, that is, the "excess" Fe forms a separate monometallic oxide phase. For a further increase of the Fe content to form $Fe_{0.98}Ni_{0.02}$, only Fe_2O_3 was detectable by XRD. The absence of detectable Ni-containing phases is likely caused by the small Ni fraction.

The metal weight loading of the materials was determined by energy-dispersive X-ray analysis (EDAX) and was in excellent agreement with the target weight loadings (to within ±2%). The coexistence of Fe and Ni and their uniform distribution on the nanoscale was further confirmed by elemental mapping in TEM (see Figure 5; the element maps of the other samples show similar homogeneities). Thus, all of the synthesized carriers were composed of alloyed Fe–Ni oxide particles of 50–100nm size with ceria particles of a similar size.

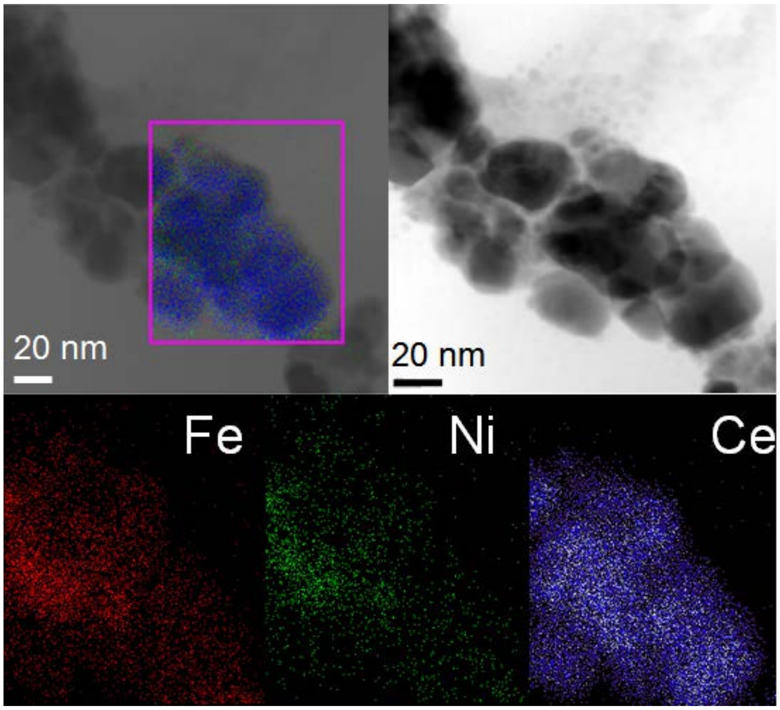

Figure 5. TEM image with (top left) and without (top right) superimposed elemental map and elemental distribution of individual elements in a $Fe_{0.88}Ni_{0.12}$ –CeO_2 calcined at 800ºC in air for 2 hr. This analysis confirms alloying on the nanoscale.

2.3.2 Reactivity of oxygen carriers with CH_4 and CO_2

The reactivity of the materials with CH_4 and CO_2 was evaluated through thermogravimetric analysis (TGA) at 800°C to monitor the carrier conversion. CH_4 and CO_2 were used for carrier reduction and oxidation, respectively. The system was purged with Ar between two consecutive reduction–oxidation cycles to obtain clearly separated oxidation and reduction phases. Note that the carrier conversion (Eq.(1)) is defined such that a conversion of 1 corresponds to the completely oxidized carrier in which all Fe is in the 3+ oxidation state and all Ni is in the 2+ oxidation state, whereas a carrier conversion of zero implies a completely reduced carrier with both Fe and Ni in their metallic states. Thus, the time required for the carrier to go from a carrier conversion of 1 to 0 (or vice versa) is indicative of the carrier reducibility (or oxidizability, respectively).

A comparison of carrier conversions versus time for the reduction half-cycles of all of the carriers tested in this study is shown in Figure 6a. The much higher reactivity of the monometallic Ni carrier with CH_4 compared with that of the monometallic Fe carrier is clearly visible: the Ni carrier is fully reduced in less than 3 min, whereas the reduction takes approximately 50 min for the Fe carrier. The reactivity of the three alloy carriers decreases with increasing Fe/Ni ratio, that is, in line with the reactivity of the pure metals, and a higher Ni content in the alloy improves the overall carrier reducibility.

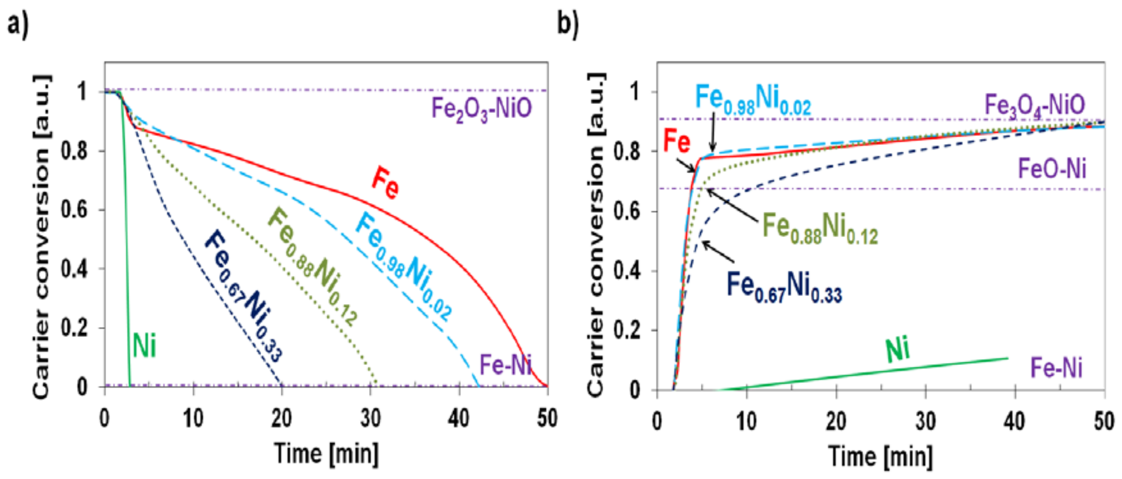

Figure 6. Comparison of overall carrier conversion during thermogravimetric analysis (TGA) of various samples with: a) CH_4 (5 sccm) at 800ºC which shows increasing Ni content leads to enhanced carrier reducibility and b) with CO_2 (20 sccm) at 800ºC which shows increasing Fe content leads to strong improvement in carrier oxidizability. The dashed horizontal lines indicate the calculated carrier weight for specific oxidation states of the $Fe_{0.88}Ni_{0.12}$ alloy.

For $Fe_{0.88}Ni_{0.12}$, which contains an excess of Fe, Fe_2O_3 is detected in addition to the nickel ferrite phase, i.e. the “excess” Fe forms a separate monometallic oxide phase. Further increasing the Fe content to $Fe_{0.98}Ni_{0.02}$, only Fe_2O_3 is detectable in XRD. The absence of detectable Ni-containing phases is likely due to the small Ni fraction.

The metal weight loading of the materials was determined by EDAX analysis and confirmed to be in excellent agreement with the target weight loadings (to within ±2%). Co-existence of Fe and Ni and their uniform distribution on the nanoscale is further confirmed via elemental mapping in TEM (see Figure 5; the elemental maps of the other samples, not shown, show similar homogeneity). All synthesized carriers were thus composed of alloyed Fe-Ni oxide particles of 50-100 nm size with ceria particles of similar size.

Although an enhancement of the carrier reactivity for methane was expected with increasing Ni content, the opposite should be expected for the reactivity of the alloys with CO_2. This is indeed the case, as shown in Figure 6, in which the carrier reactivity versus time in the oxidation half-cycle with CO_2 as the oxidant is summarized. As expected, the monometallic Ni carrier shows only minimal reactivity with CO_2. In contrast, the monometallic Fe carrier is oxidized rapidly up to a carrier conversion of approximately 0.78, which corresponds to the formation of FeO, followed by a very slow deeper oxidation to a carrier conversion of approximately 0.9, which corresponds to the carrier oxidation state of Fe_3O_4. The complete oxidation of the carrier to Fe_2O_3 was not observed, as this oxidation state is thermodynamically inaccessible under these conditions with CO_2 as the oxidant[26]. Interestingly, all of the alloy carriers follow qualitatively the same oxidation curve as that for the monometallic Fe carrier, and the transition from fast to slow oxidation shifts with increasing Ni content towards a more gradual transition at lower conversion.

The oxidation and reduction data are summarized in Figure 7, in which the times required for the reduction and oxidation of all five monometallic and alloy carriers are plotted as a function of the Ni content. The time for reduction is taken as the time for complete reduction of the carrier from its initial, fully oxidized state, whereas the time for oxidation is calculated as the time for oxidation from the fully reduced state to a carrier conversion of 0.7 (i.e., 70 % of full oxidation). The addition of only 2 % Ni causes a steep drop in the reduction time of the alloyed carrier compared with that for the monometallic Fe carrier. A further increase of the Ni content results in a further decrease in the reduction time, that is, the carrier reactivity continues to increase with increasing Ni content. Overall, we observe a strongly nonlinear decrease in the reduction times of the alloyed carriers with increasing Ni content; therefore, a strong synergy exists between the two metals: the addition of Ni does not simply result in a proportionally higher reactivity but also in a strongly enhanced reactivity of the alloy carrier. For the oxidation half-cycle, the monometallic Ni carrier is barely oxidized by CO_2 (in agreement with the thermodynamic constraints) and, hence, it was not added to the plot. In contrast to the reduction phase, a near-linear increase in the oxidation time with increasing Ni content was observed, that is, the reactivity of the carrier towards CO_2 decreases approximately linearly with the Ni content.

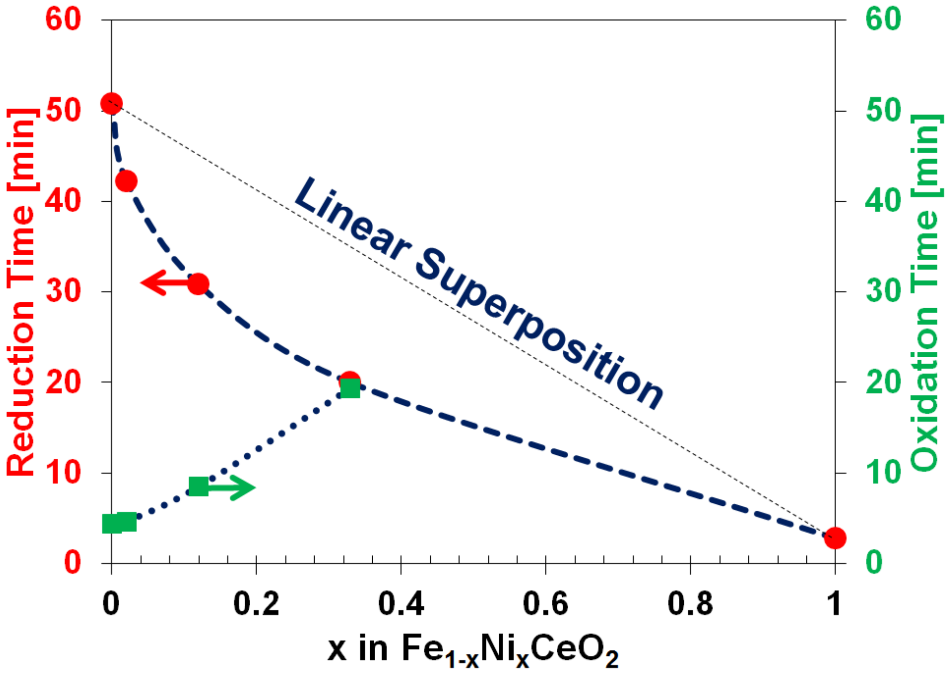

Figure 7. Comparison for reduction (circles and dashed line) and oxidation times (squares and dotted line) for the five carriers in this study (from Figure 6): Increasing Ni content strongly reduces reduction times and linearly increases oxidation times. For comparison, a line connecting the reduction times for the monometallic Fe and Ni carriers is added to the graph, representing the expected behavior for an independent, linear superposition of the reduction behavior of the two metals.

A closer inspection of the oxidation half-cycle of one of the carriers, $Fe_{0.88}Ni_{0.12}$, is shown in Figure 8 (the oxidation behavior of the other carriers is qualitatively identical, as seen above). Mass-balance calculations show that the final carrier conversion corresponds to NiO–Fe_3O_4. This observation is consistent with our previous thermodynamic calculations, which identified Fe_3O_4 as the highest attainable oxidation state of Fe in the presence of CO_2. This final oxidation state is attained for all Fe-containing carriers at approximately the same final time (see Figure 6b). This is remarkable, as our previous thermodynamic calculations showed that Ni cannot be oxidized significantly in a CO_2 atmosphere. Our results indicate that the Ni content in the carriers is oxidized in the presence of Fe; this suggests that oxygen that is “captured” by Fe is effectively “shuttled” to Ni through a solid-state diffusion process. Hence, this process also explains the deceleration in the oxidation process as the Ni content increases (see Figure 6b), as is further made visible by calculating the rate of oxidation versus time during the oxidation half-cycle (Figure 8, dashed line). A distinct transition occurs between an initial, very fast oxidation of Fe to FeO and a subsequent much slower (by one to two orders of magnitude) rate of oxidation of FeO to Fe_3O_4 and Ni to NiO. Note that no further distinction between the oxidation rates for $FeO \rightarrow Fe_3O_4$ and $Ni \rightarrow NiO$ is discernible; this suggests that the “oxygen shuttling” from iron oxide to Ni is likely not rate-limiting and that the oxidation of Ni occurs simultaneously and at comparable rate to that for the formation of the magnetite phase.

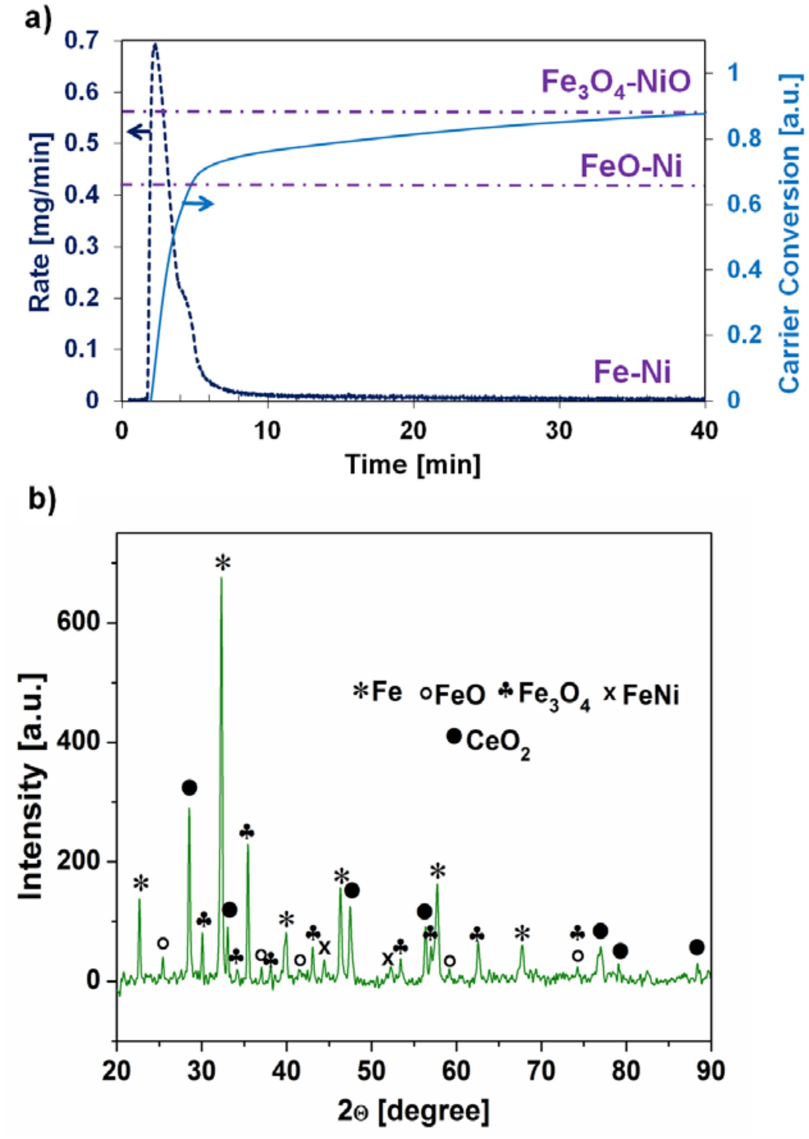

Figure 8. Re-oxidation of $Fe_{0.88}Ni_{0.12}$ by CO_2 at 800ºC in a TGA – a) Rate of oxidation vs time during the oxidation half cycle for $Fe_{0.88}Ni_{0.12}$ in the TGA at 800ºC oxidized by CO_2 (20sccm) shows two distinct regions of oxidation fast & slow, and b) ex-situ XRD after the fast oxidation regime shows multiple oxidation states of Fe.

To further confirm the oxidation states of the two metals, the oxidation was stopped at the time point at which the rate decreased (i.e., immediately after the fast initial oxidation), and the sample was cooled in an inert gas (Ar) and then transferred for analysis. The XRD pattern of the sample (Figure 8b) reveals the simultaneous presence of Fe in three oxidation states, that is, Fe, FeO, and Fe_3O_4, in addition to an Fe–Ni alloy phase. The simultaneous presence of multiple oxidation states is typical for Fe and well-documented for iron oxidation in air. Apparently, this behavior is unchanged for the oxidation with a weaker oxidizing agent such as CO_2. Furthermore, the absence of any oxidized Ni phase confirms that the oxidation of Ni, enabled by Fe, occurs in the “slow” oxidation regime.

Finally, all carriers were analyzed further by XRD at the end of the reduction and oxidation half-cycles in TGA. The results are shown in Figure 9 for $Fe_{0.88}Ni_{0.12}$. $NiFe_2O_4$, which is present in the initial oxidized sample (i.e., after oxidation in air) and is reduced at the end of the reduction half-cycle to an Fe–Ni alloy and excess Fe. Upon re-oxidation of the sample with CO_2, only one diffraction pattern is detected, which agrees with the formation of Fe_3O_4 and $Ni_{0.4}Fe_{2.6}O_4$ phases. A complete overlap between the diffraction patterns of the two oxides (which share the same inverse spinel crystal structure) makes further distinction impossible. However, the absence of any reflections for a separate Ni phase either in the oxidized or reduced state of the carrier supports the mass balance calculations, which suggest that Fe and Ni maintain a close association after the reduction and oxidation half-cycles and that both metals undergo reduction and re-oxidation during the TGA experiments. Furthermore, the stable association between Fe and Ni indicates the excellent stability of the alloys during reduction and oxidation. XRD studies of highly Ni-rich carriers ($Fe_{0.2}Ni_{0.8}$; not shown here) show the presence of excess Ni at the end of the reduction half-cycle in addition to an Fe–Ni alloy phase. Upon re-oxidation in CO_2, the Fe–Ni alloy phase was again oxidized to $Ni_{0.4}Fe_{2.6}O_4$, whereas the separate Ni phase remained in the metallic state; this further confirms that only Ni associated with Fe can be oxidized by CO_2.

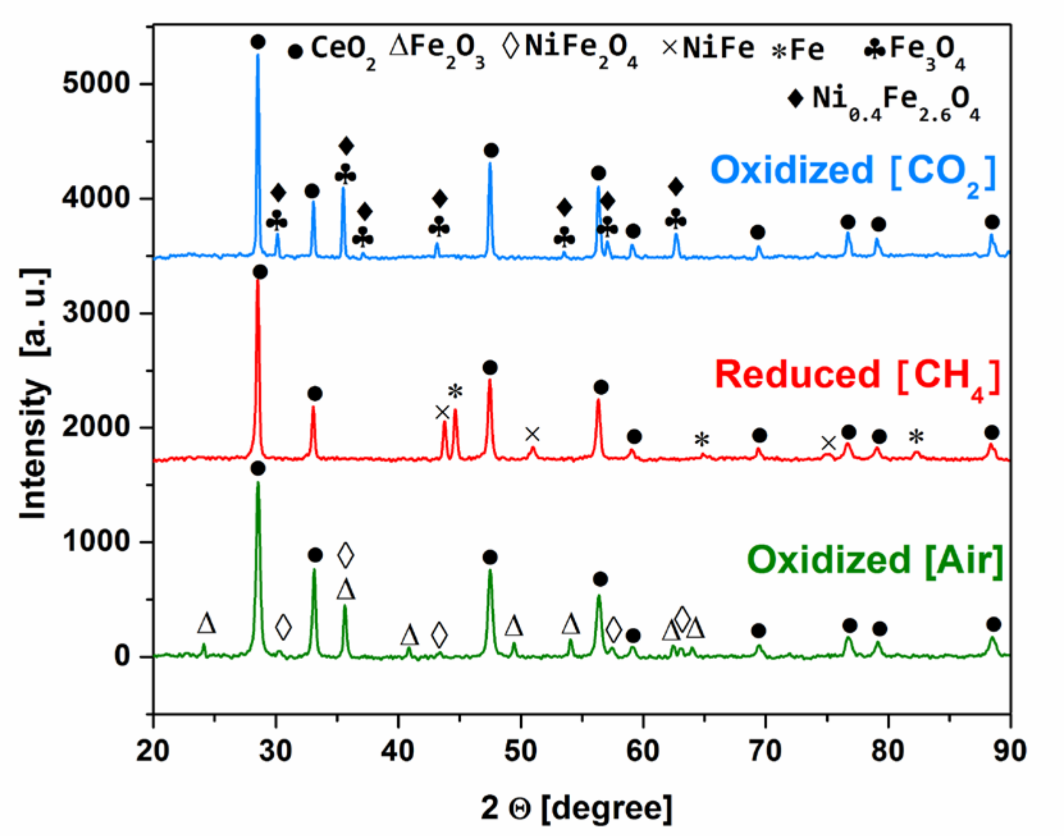

Figure 9. Re-oxidation of $Fe_{0.88}Ni_{0.12}$ by CO_2 at 800°C in a TGA – a) Rate of oxidation vs time during the oxidation half cycle for $Fe_{0.88}Ni_{0.12}$ in the TGA at 800°C oxidized by CO_2 (20sccm) shows two distinct regions of oxidation fast & slow, and b) ex-situ XRD after the fast oxidation regime shows multiple oxidation states of Fe.

2.3.3 Stability of the oxygen carriers

Carriers in chemical looping are required to undergo a large number of periodic reduction--oxidation cycles. The resulting solid-state oxygen transport during uptake and release exerts significant strain on the carrier; therefore, carrier stability is one of the key concerns in chemical looping processes. Hence, the carrier stability was investigated further in multicycle TGA experiments with H_2 and CH_4 for the reduction and CO_2 for the oxidation. Initially, H_2 was chosen as a fuel to avoid complications from possible coke formation, that is, to study the limits of the carrier stability caused purely by the temperature and solid-state redox processes. Following these tests, further test were conducted with CH_4 to determine the effect of the change in fuel. To operate in the fast oxidation regime, the carrier oxidation was kept to a partially oxidized regime (up to conversion ~ 75%). The final oxidation half-cycle was then extended to near-completion (carrier conversion < 0.9) as a further probe for carrier stability. In keeping with our goals to (1) reduce the Ni fraction in the bimetallic carrier and (2) maintain good reactivity towards the fuel and CO_2, $Fe_{0.88}Ni_{0.12}$ was selected for these studies.

2.3.3.1 Cyclic stability with H_2

Extended stability tests (50 cycles) were performed at 800, 900, and 1000 °C. The carrier performed highly reproducibly and robustly at all temperatures (Figure 10a, only the run performed at the highest temperature of 1000 °C is shown). In addition to the constant height of the maxima and minima in the cyclic carrier weight, the calculated rates of reduction and oxidation for the first and the last cycle, which form a much more sensitive indication of stable performance, show excellent agreement and, thus, further support the stability of the carrier (Figure 10b and c). Finally, the XRD analysis of the sample before and after the stability tests showed no changes to the phases present in the carrier. Moreover, the average crystallite size was essentially unchanged at all temperatures (less than 1 % change).

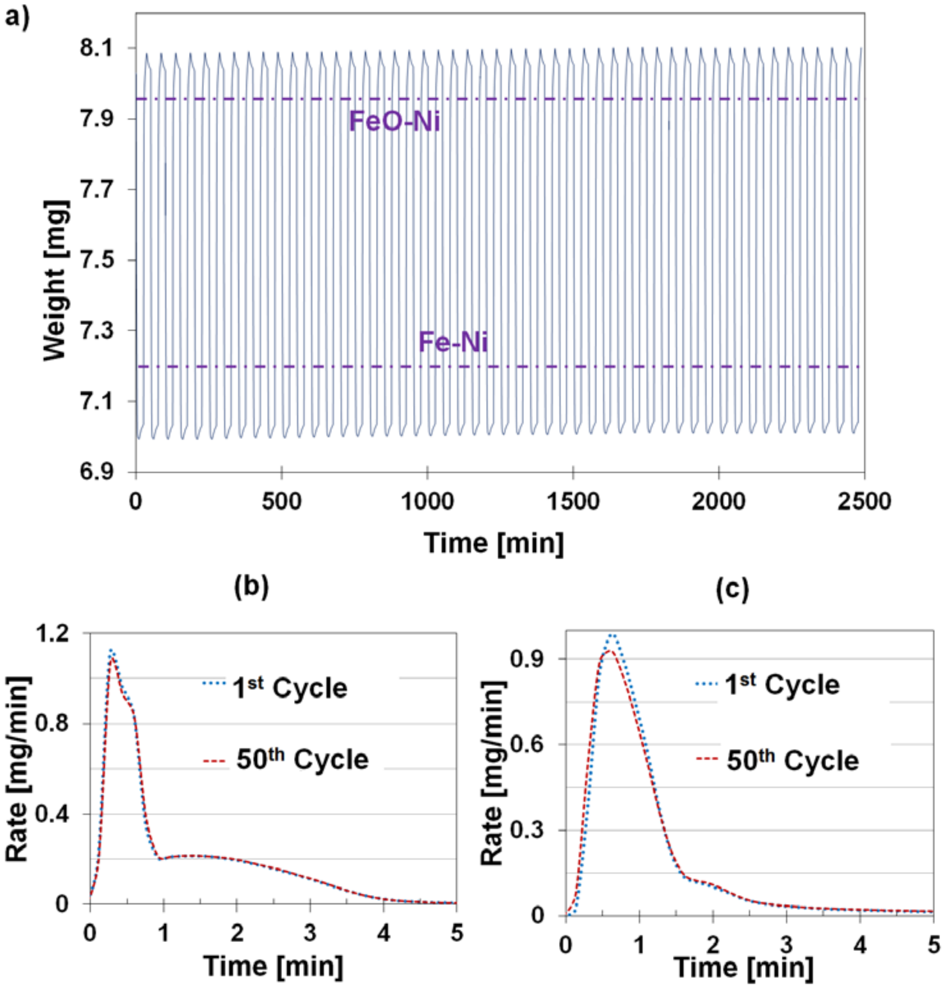

Figure 10. Multi-cycle stability test in a TGA for $Fe_{0.88}Ni_{0.12}$ at 1000ºC (H_2: 20 sccm & CO_2: 20 sccm). The results – a) Stable carrier weight oscillations vs time, and rate comparison between the 1st and 50th half cycle during b) reduction and c) oxidation, indicate robust operation over 50 cycles.

2.3.3.2 Cyclic stability with CH_4

Methane conversion processes are plagued by coking owing to methane cracking. This carbon deposition blocks active sites and, hence, deactivates the oxygen carrier during the reduction process. This can be avoided by stopping the carrier reduction before the carrier is reduced too deeply and catalyzes the non-oxidative cracking reaction. The time at which this occurs depends strongly on the carrier composition. Therefore, the optimal reduction time was first determined through carrier reduction in CH_4 until the onset of coking was observed. These carrier-specific optimal reduction cycle times were then adjusted accordingly for the subsequent cyclic experiments.

Next, preliminary tests were performed at temperatures of 800, 900, and 1000°C to study the effect of temperature on the rates of reduction and oxidation (Figure 11). As expected, higher temperature resulted in a strong increase in the reduction rates as well as increased oxidation rates. Albeit not the focus of the present study, we note that the much stronger increase in the rate of reduction with temperature suggests that the rate-limiting step for this process (presumably the initial H abstraction process) has a significantly higher activation barrier than that for the oxidation step (i.e., the oxygen abstraction from CO_2). The highest temperature, 1000°C, was chosen to further test the stability of the carrier with CH_4.

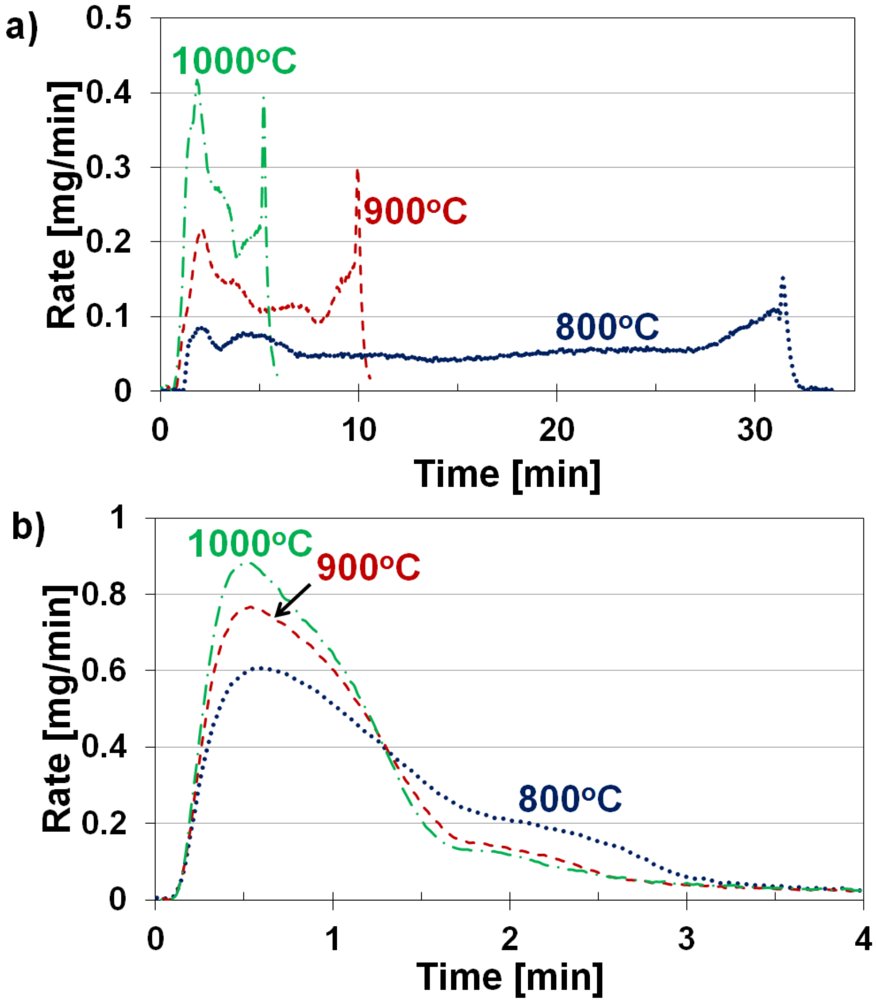

Figure 11. Comparison of rates during: a) reduction (CH_4: 5 sccm) and b) oxidation (CO_2: 20 sccm) of $Fe_{0.88}Ni_{0.12}$ at different temperatures show that increased reaction rates are observed with increase in temperature.

The alloyed oxygen carrier was subjected to ten periodic redox cycles with CH_4 and CO_2. A comparison of the rates of reduction and oxidation again shows good agreement for the first and the last cycles (Figure 12). The slight variation in the reduction kinetics can be ascribed to the small difference in the time at which the flow of CH_4 was stopped for each of the respective cycles (owing to manual operation of this particular set of experiments). Overall, the $Fe_{0.88}Ni_{0.12}$ carrier showed highly stable operation with both H_2 and CH_4 at temperatures as high as 1000°C.

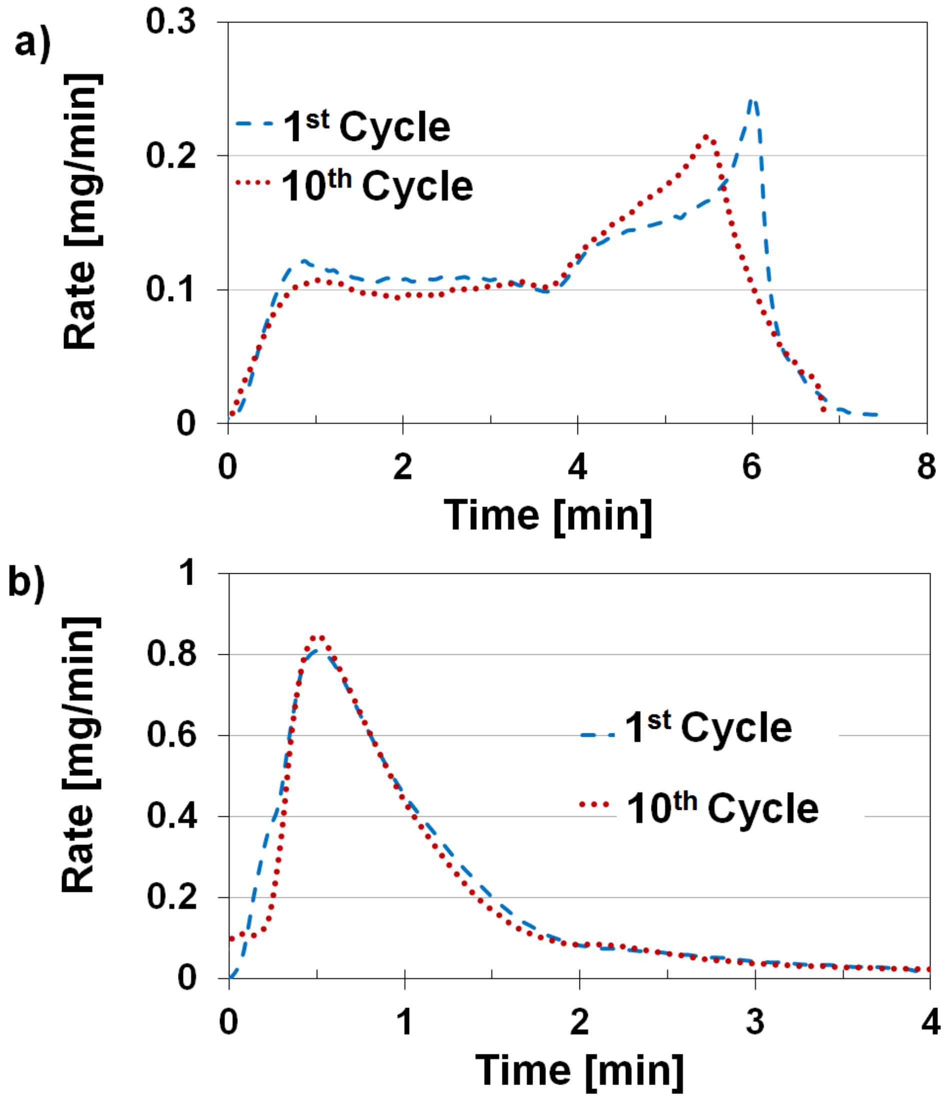

Figure 12. Comparison of rates during: (a) reduction with CH_4 (5 sccm) and (b) oxidation with CO_2 (20 sccm) for the 1st and the 10th cycle for multicycle experiment in a TGA at 1000^{o}C.

2.3.4 Fixed-bed-reactor tests

Although TGA experiments allow us to probe the changes that occur in the solid phase, that is, in the carrier, during reduction and oxidation, they do not yield meaningful information about the conversion and selectivities for the gaseous reactants. For this information, fixed-bed experiments were performed, again with $Fe_{0.88}Ni_{0.12}$ as the carrier. Owing to the strong increase in rate with increasing temperature discussed previously, the fixed-bed experiments were all conducted at 1000 °C.

A typical selectivity profile for the as-synthesized carrier obtained during reduction with CH_4 is shown in Figure 13. The reduction half-cycle shows four distinct phases: (1) total oxidation of CH_4 (t=0–5 min); (2) a mixture of total oxidation and partial oxidation (t=5–8 min); (3) highly selective partial oxidation to synthesis gas (t=8–16 min); and finally (iv) catalytic cracking of CH_4 to produce $C+H_2$ (t>16 min).

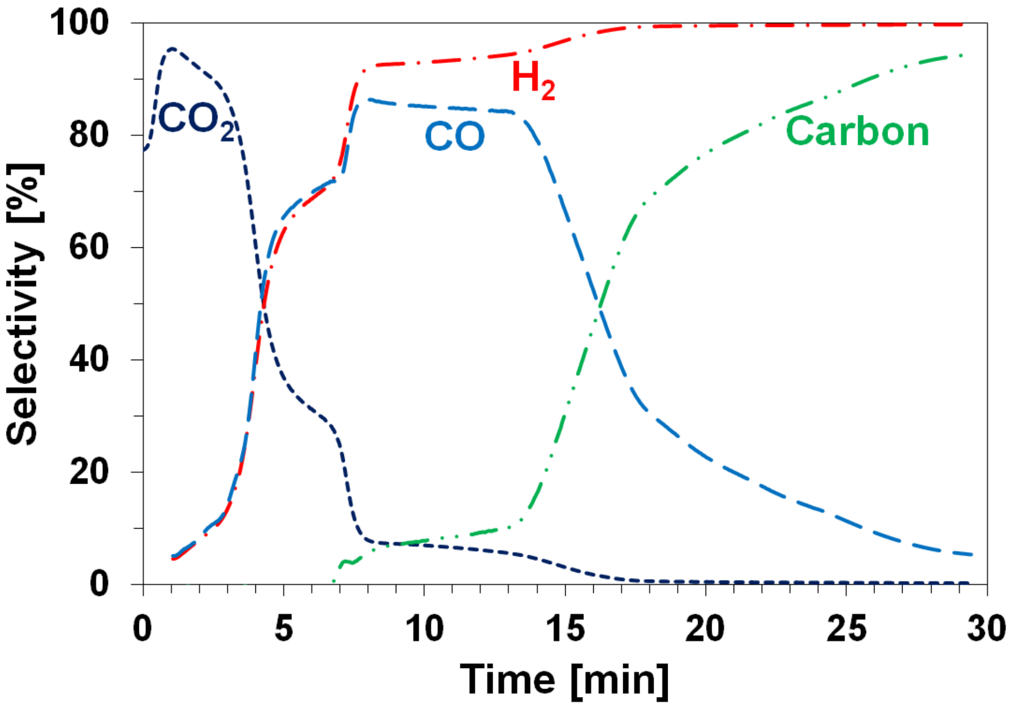

Figure 13. Selectivity towards various products as a function of time during reduction of 100mg of $Fe_{0.88}Ni_{0.12}$–CeO_2 with CH_4 (1 sccm, 16.7 vol%) at 1000ºC.

During the periodic operation, the reduction of the carrier was stopped before the onset of cracking (to avoid coke formation), and the subsequent oxidation of the reduced carrier was conducted with CO_2; this resulted in the formation of CO until CO_2 breakthrough indicated the complete (thermodynamically possible) reoxidation of the carrier. A full cycle is shown in Figure 12: the oxidation half-cycle extends from *t*=0–70 min, and the reduction half-cycle extends from *t*=80–100 min (*t*=70–80 min is the purge phase).

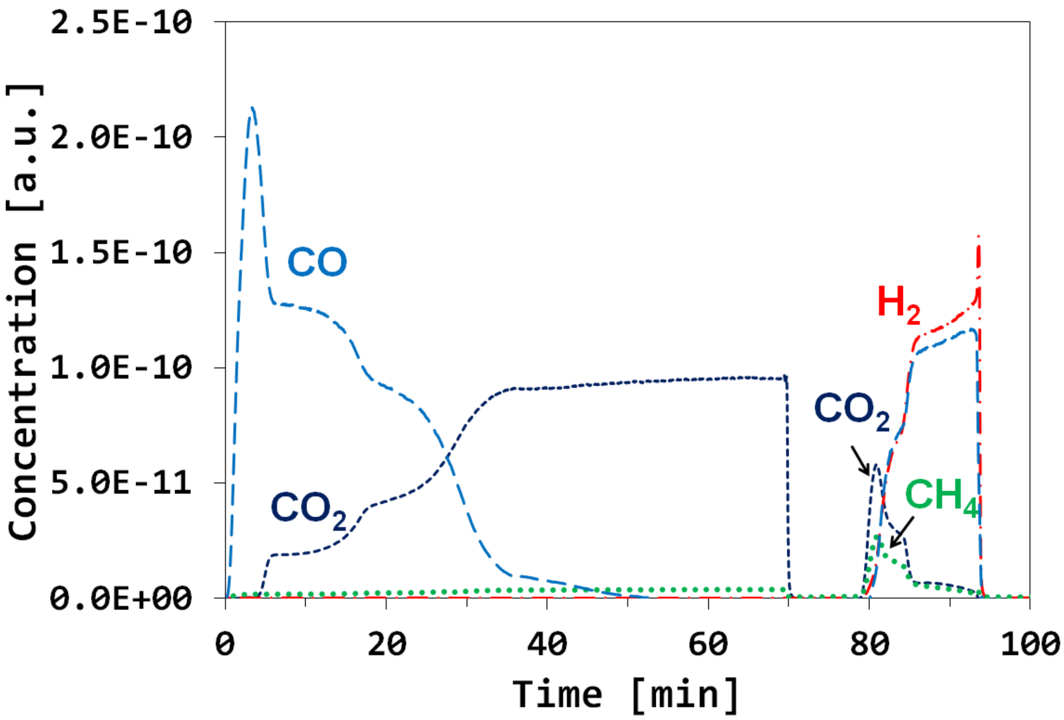

Figure 14. A full cycle of the carrier $Fe_{0.88}Ni_{0.12}$–CeO2 consists of oxidation by CO_2 (1 sccm, 16.7 vol%) and reduction by CH_4 (1 sccm, 16.7 vol%) at 1000°C.

2.3.4.1 Effect of carrier oxidation state on product selectivity

Iron–nickel alloyed oxygen carriers offer different product selectivities during reduction with CH4 depending on the oxidation state of the Fe, as observed earlier. To optimize syngas production, both the final cracking phase and the initial total-oxidation phase must be minimized. The final cracking phase can be avoided by stopping the reduction at the point at which the decrease of CO concentration (t ~ 16 min in Figure 13) indicates the onset of catalytic cracking. On the other hand, to avoid the total-oxidation products formed at the start of the reduction half-cycle, the carrier oxidation must be restricted in the preceding oxidation half-cycle. We have shown previously that this can be achieved through time-controlled oxidation with air as the oxidant[46]. The use of CO_2 as the oxidant facilitates this approach by making use of the kinetic regimes for oxidation with CO_2, that is, by stopping the oxidation of the carrier at the end of the fast kinetic regime to restrict carrier oxidation.

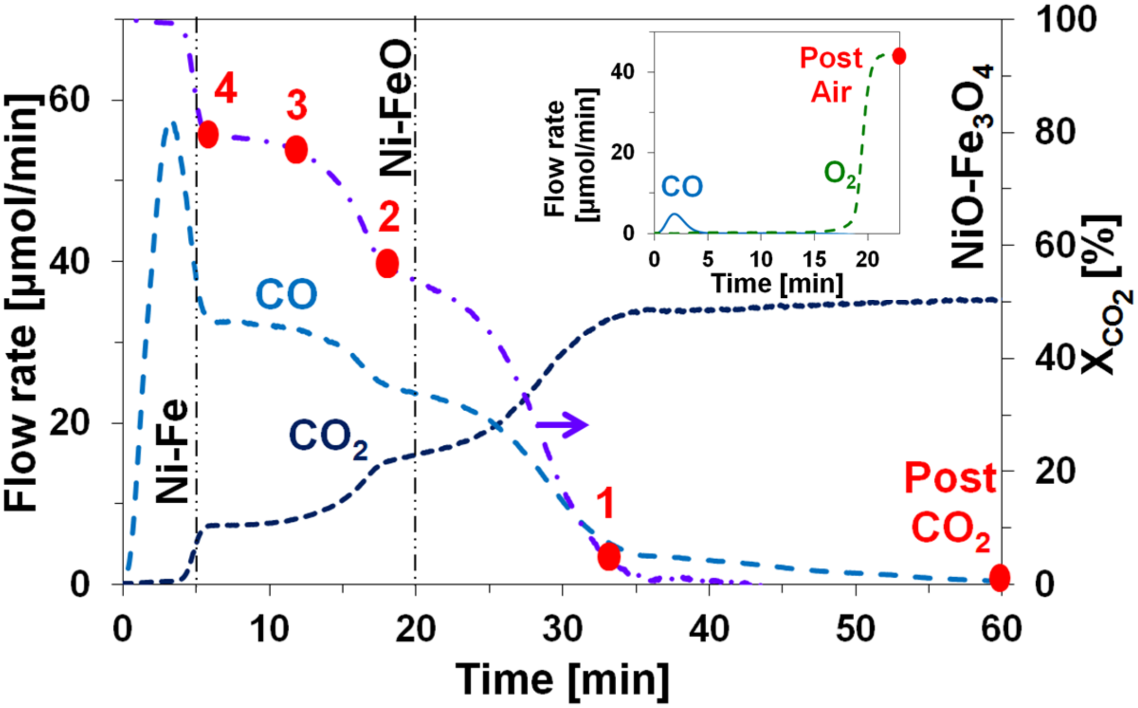

Figure 15. Re-oxidation of $Fe_{0.88}Ni_{0.12}$–CeO_2 by CO_2 (1 sccm, 16.7 vol%) shows two regions of CO_2 conversion (greater than ~60% and less than ~40%) with the red dots denoting the time where re-oxidation was stopped. The inset shows re-oxidation by O_2 (1 sccm, 16.7 vol%). All experiments were conducted post reduction by CH_4 (1 sccm, 16.7 vol%) at 1000°C.

The outlet concentrations of CO and CO_2 as well as the CO_2 conversion obtained during the reoxidation half-cycle are shown in Figure 15. The overall oxidation cycle consist of two coarse regimes: high CO_2 conversion (t=0–20 min, X_{CO2} >60%) and low CO_2 conversion (t=25–60 min, X_{CO2} <40%). The high CO_2 conversion regime can be further divided into three sections that correspond to nearly complete CO_2 conversion (t<5 min), approximately 80 % CO_2 conversion (t=5–12 min), and a third regime in which the conversion decreases from approximately 80 to 60% (t=12–25min). In contrast, a single CO peak (which is attributed to carbon burn-off) is observed during the reoxidation of the reduced carrier with O_2 (Figure 15, inset), followed by O_2 breakthrough after the complete oxidation of the carrier, that is, although carrier oxidation with CO_2 is a multistage process, the carrier oxidation with air proceeds through two steps: carbon "burn-off" followed by metal oxidation.

The "staggered" oxidation caused by the inherently slow oxidation kinetics with CO_2 as opposed to O_2 should enable a much finer control of the oxidation state of the carrier. Hence, one should expect that stopping the oxidation half-cycle at various time points during the re-oxidation would control the oxygen uptake by the carrier and, thus, control the product selectivity in the subsequent reduction cycle. This was tested next by stopping carrier oxidation during the oxidation half-cycle (with CO_2) at the times indicated by the numbered red dots in Figure 15. These partially oxidized carriers were then reduced in CH_4 to observe the impact on product selectivity. For comparison, the carrier was also oxidized to completion in air and in CO_2 (denoted by the labeled red dots in Figure 15).

The outlet concentrations of CO_2 and CO during the reduction half-cycle are shown in Figure 16 for comparison after (1) complete oxidation by air ("post-air"), (2) complete oxidation by CO_2 ("post-CO_2"), and (3) suspended oxidation by CO_2 at four different points during the oxidation half-cycle (as indicated in Figure 15). To facilitate the visual comparison, the concentration curves for case (2) and the four points of case (3) were shifted forward on the time axis (offset by 2–6 min) such that the end of the reduction half-cycle (onset of coking) for all cases occurs at the same time as that for the post-air case (*t*~17 min). Interestingly, except for the initial CO_2 formation, the curves for cases (1), (2), and the data point “1” show excellent agreement, which suggests that the methane conversion and selectivity is identical between the three cases once the same degree of carrier reduction is attained, that is, the carrier reactivity is controlled entirely by the degree of initial carrier oxidation. During air oxidation of the carrier, both Fe and Ni are oxidized to their highest oxidation states, Fe_2O_3 and NiO. Therefore, the following reduction half-cycle initially produces only total-oxidation products (represented here by CO_2), followed by syngas production (represented by CO). Notably, the CO_2 production clearly occurs in two stages with an initial large peak (centered at *t*~3 min) and a smaller second peak (centered at *t*~7 min), the nature of which will become apparent in the following.

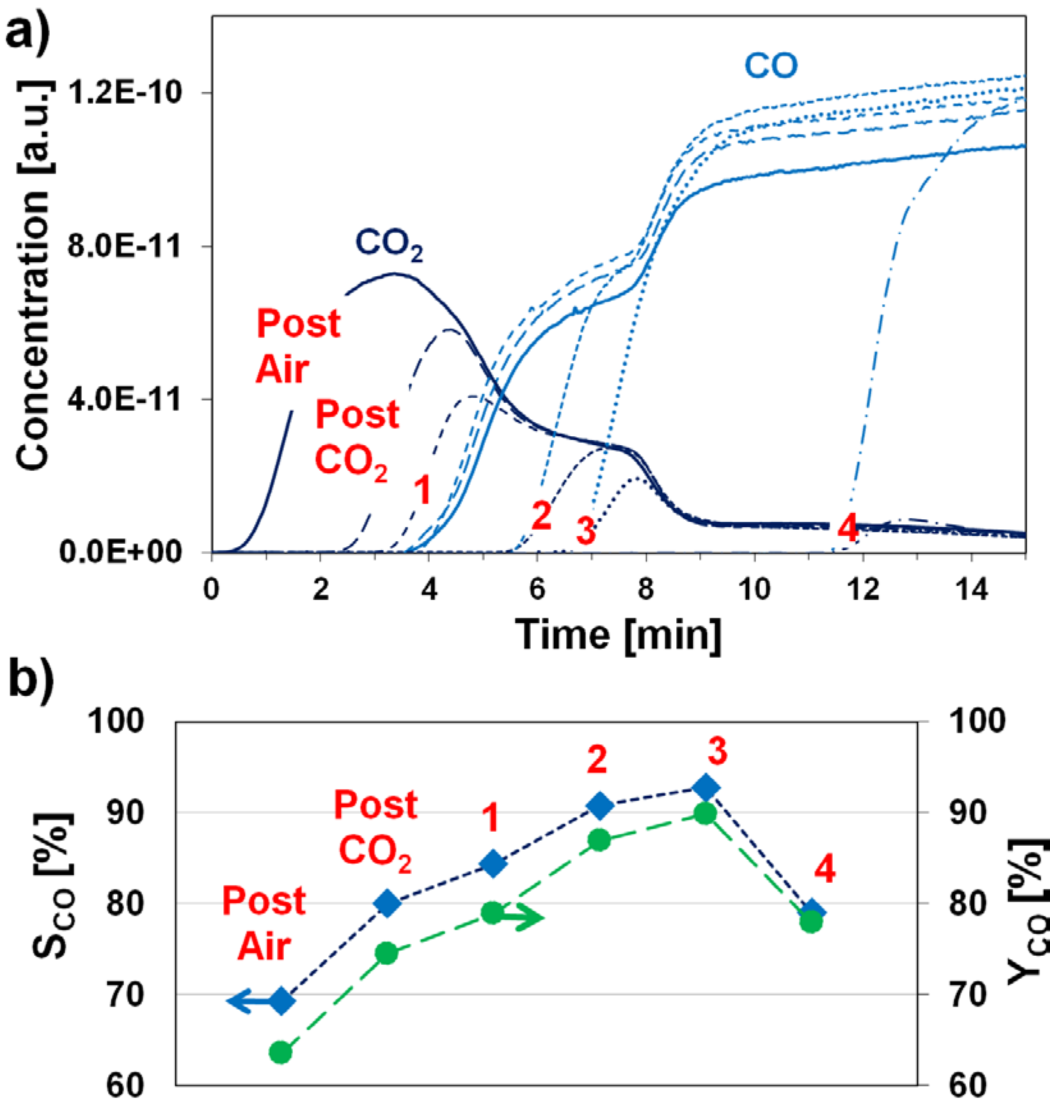

Figure 16. Reduction half cycles with CH_4 (1 sccm, 16.7 vol%) at 1000ºC following different oxidation times indicated by numbered spots according to figure 13. A comparison of a) CO_2 and CO concentration profiles, and b) CO selectivity and yield (indicative of partial oxidation), show increased syngas production is facilitated by controlled oxidation.

If the bed is fully oxidized by CO_2, the oxidation of the metals is limited thermodynamically to Fe_3O_4 and NiO (which is oxidized through solid-state diffusion, as discussed before). Thus, the subsequent reduction half-cycle produces less total-oxidation products, as evidenced by the reduced CO_2 peak, owing to the absence of the $Fe_2O_3 \rightarrow Fe_3O_4$ transition, which is known to produce CO_2 preferentially. Finally, if the oxidation time is limited to the time corresponding to “1” in Figure 15, Ni oxidation to NiO is suppressed, and the initial CO_2 peak in the following reduction is further reduced; this suggests that this part of the total oxidation is largely caused by the Ni content in the carrier. Hence, the results so far suggest that the avoidance of Ni oxidation enhances the selectivity towards syngas formation strongly but is not sufficient to suppress CO_2 formation entirely.

Therefore, the carrier oxidation was further controlled by taking advantage of the stagewise oxidation process to stop the reduction at intermediate time points (points 2–4 in Figure 13). One can see that the CO/CO_2 concentration profiles start to change more dramatically; the first CO_2 peak disappears completely, and the (smaller) second CO_2 peak decreases gradually. Remarkably, although the first, strong CO_2 peak was not accompanied by CO formation, that is, it indicated a completely selective oxidation to CO_2 over the highly oxidized carrier, the second CO_2 peak coincides with the onset of CO formation; therefore, this CO_2 is either the result of parallel total/partial oxidation pathways or, more likely, the result of a sequential reaction in which CO formed in the initial oxidation of CH_4 is further oxidized to CO_2. The extent of the carrier oxidation corresponding to these time points was calculated through an oxygen mass balance with the Fe_3O_4–NiO carrier at *t*~60 min (i.e., post-CO_2 in Figure 15) as the reference point. The calculated oxidation states, Fe--Ni (for *t*~ 5min) and FeO–Ni (for *t*~ 20min), agree closely with time points 4 and 2, respectively, and further confirm that high syngas selectivity can be achieved by restricting the carrier oxidation to FeO–Ni.

For direct comparison, the CO gas-phase selectivity and yield are compared for all of the oxidation scenarios considered here in Figure 16b. Clearly, the selectivity towards partial oxidation increases continuously with the reduced degree of carrier re-oxidation. However, too large a restriction of the carrier oxidation results in undesirable methane cracking and, hence, a strong drop in CO selectivity (whereas methane conversion remains high; see point 4). This is expected as the bed remains partially in the (metallic) state after the oxidation half-cycle, as is evidenced by the subsequent "short" reduction half-cycle (Δt ~5 min).

2.3.4.2 Chemical looping dry reforming operation

Finally, the insights gained allow the development of an optimized CLDR process, which utilizes the controlled oxidation of the Fe–Ni alloy carrier in the "fast CO_2 oxidation regime" in the oxidation half-cycle to enable the highly selective production of syngas streams in the reduction half-cycle. Again, the carrier for the process was $Fe_{0.88}Ni_{0.12}/CeO_2$, which is oxidized at high CO_2 conversions (oxidation stops at time point 3, see Figure 15) and then reduced in CH_4 before the cycle is restarted. A full cycle in this manner is shown in Figure 17.

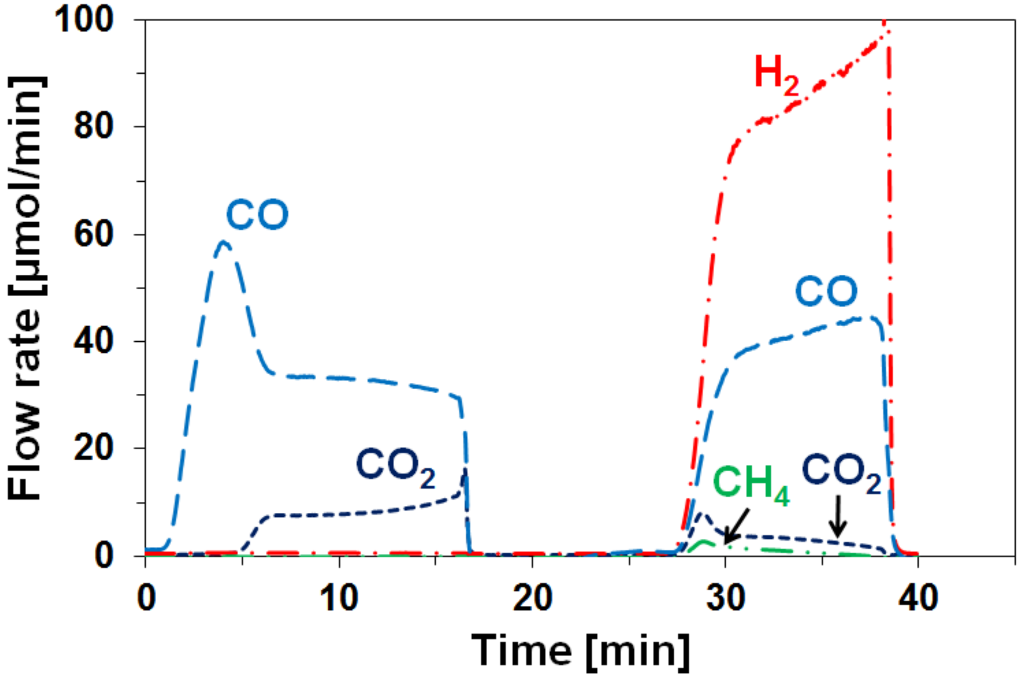

Figure 17. Full CLDR cycle for $Fe_{0.88}Ni_{0.12}$–CeO_2 with restricted oxidation (point 3 in Figure 13) during the oxidation half cycle (CO_2, 1 sccm, 16.7 vol%) and subsequent reduction with CH_4 (CH_4, 1 sccm, 16.7 vol%) at 1000°C.

An inspection of the time-resolved outlet-gas concentration profiles (Figure 18) obtained during the reduction half-cycle for this modified mode of operation reveals a small residual CO_2 peak at the start of the cycle, and this peak decays quickly as the partial oxidation products CO and H_2 are produced. Over the entire half-cycle, the concentration profiles of H_2 and CO essentially overlap (supporting the earlier use of CO as an indicator for partial oxidation), and good selectivity towards partial oxidation ~90^%) was observed over the entire cycle with a H_2/CO ratio of approximately 0.5, as typically desired for the downstream utilization of syngas (note: the selectivity was calculated after the first minute at which the carbon balance closes within 10%). Correspondingly, a negligible amount of carbon is produced over the cycle. It is furthermore noteworthy that this carbon is burnt off by CO_2 in the subsequent oxidation cycle and it adds to the CO produced, that is, it becomes integrated fully into the value stream of the process.

During the carrier reoxidation, a high CO_2 conversion of approximately 90^% is obtained over the oxidation half-cycle. As is apparent from the flow-rate traces (Figure 15), even higher CO_2 conversions may be attainable upon further optimization; however, this was not the intent of the present study. Overall, the modified CLDR operation allows for robust operation with high fuel conversion and product selectivity.

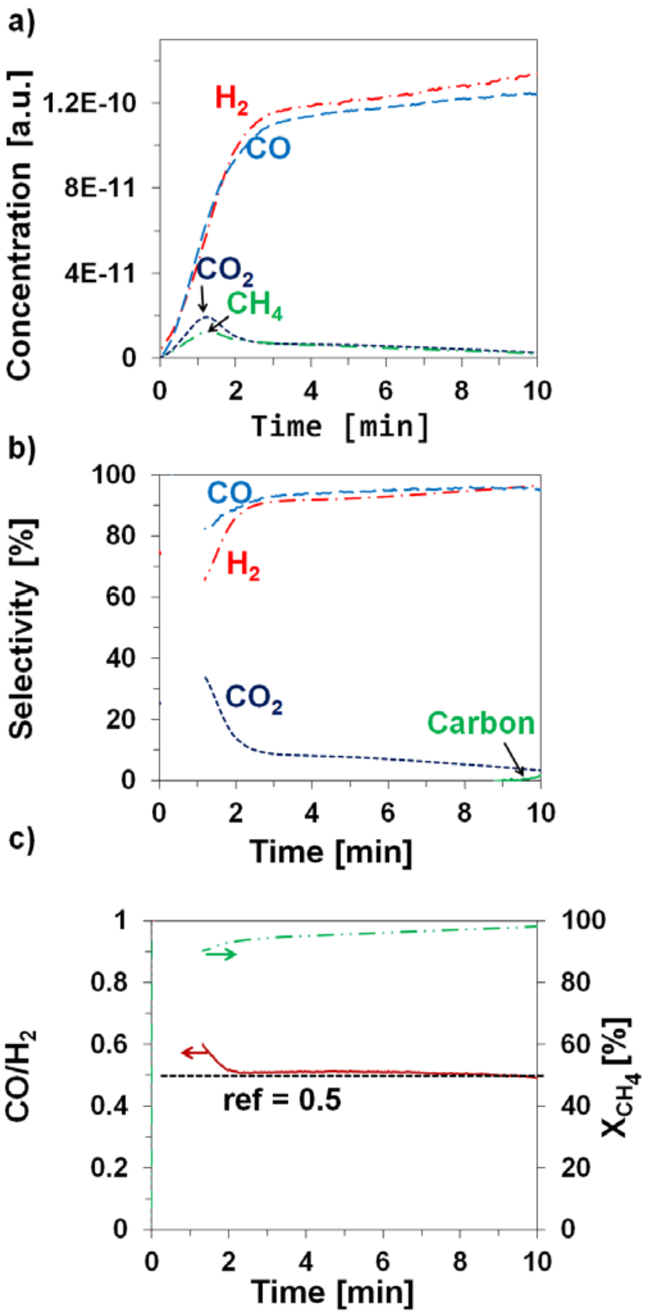

Figure 18. The reduction half cycle of Fe$_{0.88}$Ni$_{0.12}$–CeO$_2$ in CH$_4$ (1 sccm, 16.7 vol%) at 1000°C in the optimized cyclic CLDR operation: a) concentration profiles, b) product selectivity, and c) methane conversion (X_{CH4}) and syngas ratio (H_2:CO) vs time.

2.4 CONCLUSIONS

The abatement of CO_2 emissions from the utilization of fossil fuels is a key challenge of our times. In the present study, we demonstrated that a modified methane dry reforming process through “chemical looping dry reforming” (CLDR) constitutes not only one of the most simple processes for CO_2 activation through the reduction to CO but also increases significantly the efficiency of conventional (catalytic) dry reforming. The process allows for high methane and CO_2 conversions in excess of 90%, the coking issues that typically plague dry reforming processes are avoided, and syngas (at the desired H_2/CO ratio of 2) and excess CO are obtained in inherently separate product streams.

The process is enabled by the combination of Fe and Ni in alloy carriers, which combine the high reactivity of Ni for methane activation with the good selectivity of iron oxides for syngas formation and the ability of Fe to reduce CO_2 to CO. Hence, the combination of these two metals not only enables the process but also introduces strong synergistic effects: the addition of a small amount of Ni into an Fe-based carrier results in the strong enhancement of the reactivity with methane, whereas the presence of Fe enables the oxidation of Ni with CO_2 (which is thermodynamically restricted for pure Ni under the same reaction conditions). The latter indicates a strong coupling of the two metals through oxygen transport in the solid carrier and, hence, suggests that similar effects should exist for many other metal combinations. Therefore, alloyed carriers likely hold much broader potential for redox processes in a “looping” configuration than one might anticipate, as a smart combination of two metals might allow the reconciliation of contradictory demands in the two, coupled half-cycles. Clearly, the stabilities of these alloys under the extreme conditions of these high-temperature redox processes must be considered and might be a limiting factor for many cases. In the present study, the Fe_xNi_y carriers kept their alloyed nature over multiple reduction–oxidation cycles, that is, they showed stable operation without signs of permanent dealloying.

Finally, the product selectivities were dependent on the oxidation state of the carrier, as one would expect. Hence, the use of a weak oxidant such as CO_2 is beneficial, both from a thermodynamic and a kinetic point of view: CO_2 oxidation is much more restricted thermodynamically and, hence, can limit the over-oxidation of a carrier material, and the relatively slow oxidation kinetics allows the oxidation state to be controlled through the oxidation time.

Thus, overall, the present study demonstrated not only that CLDR is a promising process for CO_2 utilization but also that CO_2 can have desirable properties as an oxidant in chemical looping processes and that alloy carrier materials hold vast promise for selective oxidation processes through chemical looping “beyond combustion”.

See Appendix B for an alternative explanation of the alloy oxidation mechanism.

3.0 PHYSICAL MIXTURES AS SIMPLE AND EFFICIENT ALTERNATIVE TO ALLOY CARRIERS IN CHEMICAL LOOPING PROCESSES

The content of this chapter is taken from More et. al., Physical Mixtures As Simple And Efficient Alternative To Alloy Carriers In Chemical Looping Processes, *AIChE Journal.* (in press).

3.1 INTRODUCTION

Over the past few decades, Chemical Looping Combustion (CLC)[8,9,11,12,51] has emerged as a promising technology for efficient combustion with inherent CO_2 capture well within the framework of the existing energy infrastructure. In CLC, a metal oxide–-typically a transition metal--is used as an oxygen source for fuel combustion in a "reducer" reactor, thereby generating only the combustion products CO_2 and H_2O, which can be easily separated to generate a sequestration-ready CO_2 stream. After combustion, the reduced metal is then regenerated in an "oxidizer" reactor (typically with air) and recycled back to the reducer, completing the materials "loop". Thus, CLC bypasses most of the problems of conventional fuel combustion, including NO_x formation and CO_2 separation from dilute gaseous streams, and is currently emerging as a favored solution for large-scale clean combustion applications[52-55].

More recently, the chemical looping scheme has been used successfully beyond combustion towards a broader goal of fuel upgrading to value-added chemicals[11,36,37]. For example, we have demonstrated in recent years that pure H_2 streams can be produced by replacing air with H_2O in the "oxidizer", resulting in chemical looping steam reforming of methane (CLSR)[56], while using CO_2 as oxidant results in its reduction to CO (a useful and reactive chemical feedstock) in a chemical looping dry reforming (CLDR) configuration [26,28]. Similarly, the fuel conversion in the "reducer" reactor can be tailored to produce syngas from methane[57], with CO_2 or air as oxidants, resulting in a chemical looping partial oxidation of methane (CLPOM) process[46].

Although the principle of chemical looping thus has been widely demonstrated for different configurations, significant challenges remain for large scale application. In particular the development of oxygen carriers which are cheap, reactive, as well as chemically and thermally stable over extended cyclic operation at harsh conditions, is paramount for robust process operation. Most of the carriers reported in the literature are supported Fe-, Cu-, Ni-, and Mn- based engineered materials[38,58-60]. Due to their abundance, low cost, and low toxicity, Mn and Fe materials have emerged as the most popular choice for oxygen carriers. However, both materials suffer from slow redox kinetics and correspondingly low fuel conversion[61]. Conversely, while Ni-based oxygen carriers are promising due to their high reactivity with methane and other fuels, the relatively high cost and toxicity of Ni limit their application as oxygen carriers[62]. Finally, Cu- based oxygen carriers have a high oxygen release capacity, yet suffer from agglomeration under typical operational conditions due to the low melting point of Cu[38].

In an attempt to overcome the limitations of these monometallic carriers, the focus has recently shifted towards development of mixed metal oxides. For example, the redox kinetics of Fe based carriers can be significantly improved by addition of small amounts of Ni (i.e. via formation of Fe-Ni alloys), thus offering much enhance reactive performance at lower overall carrier cost and toxicity[41,63,64]. Similarly, addition of Ni helps stabilize the low-melting Cu in Ni-Cu alloys, improving the overall carrier stability at high temperatures[54]. Recent work in our own lab has demonstrated that combining Mn (instead of Ni or Cu) with Fe not only augments the carrier reactivity at reduced cost, but also mitigates the environmental impact of oxygen carriers, further confirming the benefits of mixed metal systems[40]. However, Fe-based alloys form complex spinel structures which are periodically formed in the oxidation half step and broken down in the reduction half step of the cyclic process[41,65-67]. Understanding these lattice structure transformations and the governing oxygen transport and reaction mechanisms is important for rational design of oxygen carriers. While a recent study by Qin et al.[68] provided some insights into nanoscale evaluation for Fe-Ni alloys, the observations are largely limited to post-reaction analysis of the material. Hence, the important physicochemical changes occurring *during* the redox processes, which are representative of the underlying oxygen transport, still remain poorly understood. Moreover, Fe-Mn[40,69] and Fe-Cu[70] alloys have been shown to undergo complex de-alloying and re-alloying processes during redox operation further complicating such analyses.

Physical mixtures of two monometallic carriers potentially offer a much simpler alternative towards rational oxygen carrier design – but at first view do not seem to enable the synergies between the constituent metals as for alloys. However, Johanson et al. already demonstrated a mixture of iron and nickel oxides can yield significantly improved yields of CO_2 in methane combustion compared to the individual oxides[71]. Since the methane feed was diluted with steam (1:1), they hypothesized that catalytic steam reforming of methane over Ni produced syngas which was further combusted (to CO_2 and H_2O) over iron oxide, improving the overall CO_2 yield. Using a similar configuration, Gayan and coworkers reported improved combustion efficiencies for physical mixtures compared to alloys due to suppression of steam reforming when nickel is chemically mixed with iron[72]. While both studies suggest that addition of Ni can improve the performance of iron oxide, the focus of these studies was exclusively on improved power production i.e. total combustion efficiency. Furthermore, the near equimolar steam dilution of the methane feed employed in these studies will simultaneous oxidize metallic iron (as demonstrated previously[56]) which further complicates evaluation of this system. Finally, Moghtaderi and Song investigated binary physical mixtures amongst Fe-, Cu- and Ni- oxides in the presence of CO, H_2 and CH_4 showing enhancement in reduction kinetics as compared to the parent oxides, although the reason for the enhancement remained unclear[73].

The present contribution extends these previous studies by systematically comparing the reactive performance of physical mixtures and alloys for pure CH_4 and identifying the synergistic effects at play. More importantly, we extend the previous investigations by applying physical mixtures towards *selective* (partial) oxidation, i.e. by using an unselective metal as “initiator” and a selective one as the “product guide”. Towards this goal, we synthesize oxides of Fe and Ni supported on ceria, which we have previously shown to strongly enhance oxygen transport and oxygen carrying capacity of supported metals, reduce the carrier sensitivity to coking, and a stabilize both single metal and alloyed carriers[40-42]. The physically mixed carriers are compared with alloyed carriers (with identical metal content) in thermogravimetric analysis to establish differences in the reactivity trends. Multi-cycle tests are then carried out to test the stability of the carriers and further investigated in a fixed bed reactor set-up to test the product selectivity and fuel conversions. Finally, we incorporate a “soft” oxidant (CO_2) to selectively oxidize one of the two carrier components while again enabling CO_2 activation via reduction to CO, and demonstrate the added flexibility of the physically mixed configuration for improving process selectivity.

3.2 EXPERIMENTAL SECTION

3.2.1 Material Synthesis

All carriers were synthesized by a simple wet-impregnation approach. For the alloy carriers, appropriate quantities of the metal nitrate precursors, $Fe(NO_3)_3.9H_2O$ and $Ni(NO_3)_2.6H_2O$ (99+%, Sigma Aldrich), were dissolved in 1mL ethanol. Commercially available CeO_2 powder (99+%, Alfa Aesar) was then added to the solution, stirred continuously for 2 hours and vacuum dried overnight (90^{o}C). The resulting solid cake was ground using a mortar-pestle and then calcined in air (0.2 SLM) at 800^{o}C for 2hr. All alloy carriers were synthesized with 40 wt% metal, with three different Fe:Ni ratios of 98:2, 88:12 and 67:33, respectively. Monometallic Fe and Ni carriers with 40 wt% metal were also synthesized by the same approach. Homogeneous physical mixtures of the two monometallic carriers were produced by mixing solid suspensions (in C2H5OH) of appropriate quantities of each monometallic carrier, followed by drying to evaporate the solvent.

3.2.2 Material Characterization

X-Ray Diffraction Characterization. To confirm the phases present, the synthesized carriers were analyzed by a powder X-Ray diffractometer (Bruker D8) operating at 40kV and 40mA with Cu Kα radiation (λ=1.5418 Å). The data was recorded between 2Θ values of 20^o and 90^o with a scanning rate of 3.5^o/min. The phases were identified using the JCPDS database and the average crystallite size was determined by the Scherrer equation.

Surface area. BET (Brunauer-Emmett-Teller) surface area determination was conducted via Nitrogen adsorption/desorption in a Micrometrics ASAP 2020 gas adsorption analyzer at -196^{o}C. The samples were pretreated by degassing under vacuum for 2hr at 200^{o}C. All samples in this study had low surface areas ($< 5\ m^2/g$), as expected due to initial sintering of the materials.

Electron Microscopy. A Transmission Electron Microscope (TEM) JEOL-200CX was used to image the particles. Bulk metal weight percentages and metal dispersion of the synthesized samples were analyzed by Energy Dispersive X-Ray Analysis (EDAX) performed using an Oxford INCA EDS system attached to a JSM-6510LV SEM.

3.2.3 Reactive Testing

Solid-Phase Reactivity. Carrier reactivity was determined by a Thermo-Gravimetric Analyzer (SDTQ600, TA Instruments). Alumina pans containing 10-15mg of sample powders were loaded into the instrument. The temperature was ramped up to the reaction temperature at 100^{o}C/min and then held isothermally for the experiment duration. The gases used were: N_2 (Grade 5.0, 100sccm), Ar (Grade 5.0, 20sccm), H_2 (Grade 2.0, 20sccm) CH_4 (Grade 2.0, 5sccm) and CO_2 (Grade 2.0, 20sccm). The carrier gas (N_2) is flown continuously throughout the experiment. The reactive gases H_2/CH_4 and CO_2, are used for the reduction and oxidation of the carrier respectively, and the purge gas (Ar) is used to flush the system between consecutive reduction and oxidation cycles. For comparison between the various carriers carrier conversion was defined as follows:

$$Carrier\ Conversion = \frac{Sample\ Weight - Reduced\ Weight}{Oxidized\ Weight - Reduced\ Weight}$$

Eq. (9)

The oxidation states of the samples were calculated from the sample weight by a simple mass balance relative to the fully oxidized sample weights.

Gas-Phase Reactivity. Conversion of the fuel (CH_4) and product selectivity were determined in a fixed bed reactor set-up. 100mg of sample was packed between two glass wool plugs in a horizontal quartz tube (1/4” ID) enclosed by a furnace (Thermo electron corporation-Lindberg/Blue M). The bed temperature was measured by a coke resistant, high-temperature thermocouple (Omega Engineering). The gases used were: Ar (5sccm and 40sccm), CH_4 (Grade 2, 1 sccm) CO_2 (Grade 5.0, 3 sccm) and 20% O_2 in He (Grade 5, 3 sccm). Outlet gas concentrations were measured by a mass spectrometer (Pfeiffer Omnistar QMS 200), and the corresponding molar flow rates (ni) were calculated from the (calibrated) ion currents. The accuracy of the measurement was checked by performing carbon balances over the system and closed to within 5-10%.

For the reduction half cycle the carbon balance was calculated as:

$$n_{CH_{4,in}} = n_{CH_{4,out}} + n_{CO_{2,out}} + n_{CO_{out}} + 0.5 \times (n_{H_{2,out}} - 2n_{CO_{out}})$$

Eq. (10)

The conversion and selectivity of the various gaseous products involved were calculated using the following formulae:

$$X_{CH_4} = \frac{n_{CH_4,in} - n_{CH_4,out}}{n_{CH_4,in}} \qquad S_{H_2} = \frac{n_{H_2,out}}{n_{CH_4,in} - n_{CH_4,out}}$$

Eq. (11), (12)

$$S_{CO} = \frac{n_{CO_{out}}}{n_{CH_4,in} - n_{CH_4,out}} \qquad S_{CO_2} = \frac{n_{CO_{2,out}}}{n_{CH_4,in} - n_{CH_4,out}}$$

Eq. (13), (14)

The major reactions in the system are total oxidation, partial oxidation and catalytic pyrolysis of CH_4:

Total Oxidation:	$CH_4 + 4\ MeO \Leftrightarrow 4\ Me + CO_2 + 2\ H_2O$	(R5)
Partial Oxidation:	$CH_4 + MeO \Leftrightarrow Me + CO + 2\ H_2$	(R6)
Methane Pyrolysis:	$CH_4\ (+\ Me) \Leftrightarrow 2\ H_2 + C\ (+\ Me)$	(R7)

For the oxidation half cycle the carbon balance was calculated as:

$$n_{CO_{2,in}} = n_{CO_{2,out}} + n_{CO_{out}}$$

Eq. (15)

3.3 RESULTS AND DISCUSSION

3.3.1 Oxygen carrier reactivity with CH_4

The reactivity of the oxygen carriers with CH4 was initially studied in a thermo-gravimetric analyzer (TGA) at 800°C. The weight change upon reducing the carrier by CH_4 was recorded and carrier conversion, which is indicative of the oxygen loss/gain for the carrier, was calculated and used to compare all carriers. Results are shown in Figure 19a. Carrier conversion of 1 corresponds to the completely oxidized carrier (where all Fe is in the Fe_2O_3 state and Ni in the NiO state), while carrier conversion of 0 indicates a completely reduced carrier with both Fe and Ni in their metallic states. Thus, the time required for the carrier to undergo complete reduction from carrier conversion of 1 to 0 is indicative of the carrier reducibility. As a reference and to indicate deviations from a simple linear superposition of the reactivity of the two monometallic carriers, a curve representing the reduction times calculated from a linear superposition of the monometallic carriers was furthermore added to the graph (i.e. $t_{calculated} = 0.88*t_{Fe} + 0.12*t_{Ni}$)

The results in Figure 19a show that all carriers in this study were completely reduced by CH_4, although at significantly different rates. As expected, the monometallic Fe carrier took longest for reduction due to the slow reduction kinetics of Fe_2O_3. In contrast, the monometallic Ni carrier was reduced rapidly due to the well-known catalytic properties of Ni. The alloy "inherits" some of this high reactivity of Ni and thus shows higher reactivity than the monometallic Fe carrier. The reactivity is well in excess of a simple, linear superposition of the reactivities of the monometallic carriers (represented by the calculated "$(88\%Fe + 12\% Ni)_{calc}$" curve), thus indicating significant synergies between the two metals in the alloy. We had previously explained this effect by efficient methane activation on Ni centers, followed by oxidation of the dissociated methane on iron oxide (and, for higher Ni content, also partially on NiO). As this mechanism relies on an intimate contact of the Ni and Fe phases, one would expect this acceleration to cease entirely for physical mixtures, in which no direct phase contact between Ni and Fe exists.

Remarkably, the physically mixed carrier (with the same Fe:Ni ratio) not only showed again a strong acceleration over the monometallic Fe carrier, but was in fact reduced also much faster than the respective alloy. Similar observations were seen for other Fe:Ni compositions investigated (not shown here). For comparison, Figure 19b shows the times required for complete reduction of the two monometallic and all three alloy carriers and the respective monometallic physical mixtures as function of their respective Ni content. As expected, the Fe-Ni alloys show a continuous—though "super-linear"—drop in reduction time with increasing Ni content, confirming that the presence of Ni accelerates the carrier reduction and that synergistic effects between Ni and Fe result in a stronger-than-linear decrease in reduction time. This synergy is most pronounced at low Ni content. Reduction times for the physical carrier mixtures are consistently lower than those for the alloys at the same composition. Furthermore, reduction time drops precipitously with increasing Ni content and reaches essentially identical values with the pure Ni carrier for as little as 12% Ni/CeO_2 mixed with 88% Fe/CeO_2. Thus, addition of a small amount of Ni-carrier results in a drastic acceleration of the reduction of the (monometallic!) Fe-carrier present in the mixtures, indicating that the reduction mechanism for the physically mixed carriers must follow a very different mechanism than that for the alloy carriers.

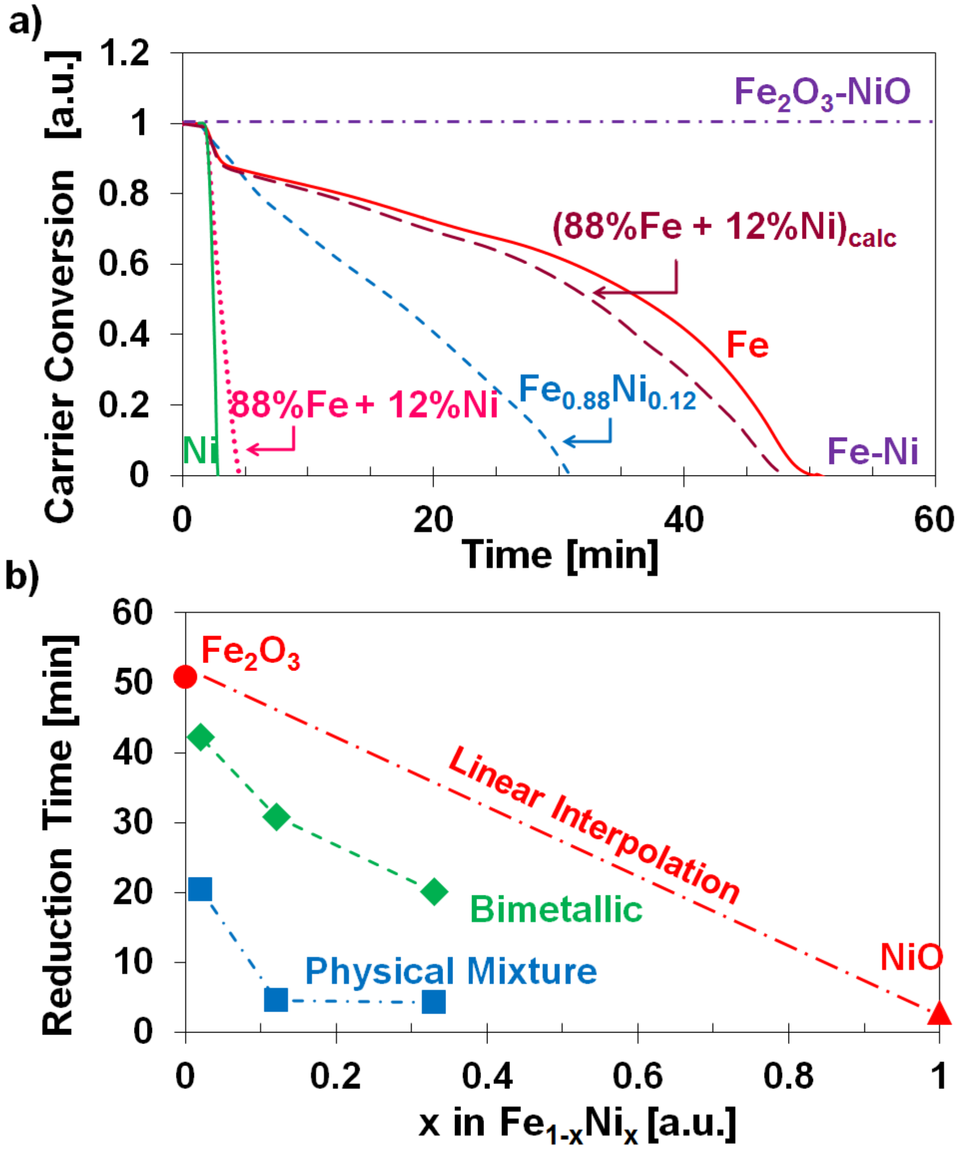

Figure 19. a) Carrier conversion vs time during the reduction half cycle (w/ CH_4) in TGA at 800ºC. The horizontal lines at X= 0 and X=1 represent the fully oxidized and fully reduced states of the two metals (Fe and Ni), respectively. b) Reduction time (w/ CH_4 in TGA at 800ºC) vs Ni fraction for physical mixtures and corresponding alloy carriers. The physically mixtures reduce at a much faster rate than the alloys for all three compositions investigated suggesting an altered reaction mechanism.

3.3.2 Proposed reaction mechanism for Fe-Ni physical carrier mixtures.

The enhanced reduction kinetics of the Fe-Ni alloys can be explained by the lattice associations between the constituent metals i.e. Fe and Ni, which enables a cooperative reaction mechanism through spill-over between surface species and sharing of lattice oxygen. However, in the physically mixed carrier, monometallic Fe_2O_3 and NiO particles are at best in macroscopically close proximity of each other but are neither in microscopic vicinity of each other nor do they share a common lattice. Unsurprisingly hence, the XRD pattern of this carrier shows distinct Fe_2O_3 and NiO peaks, confirming that no unintended cross-contamination of the carriers either during physical mixing or reactor operation resulted in the unexpected formation of an alloy phase (as further discussed below, see Figure 23). Hence, during reduction we can expect the two metal fractions of the mixture to reduce independently of each other. However, due to its inherently faster reduction kinetics, NiO will reduce to metallic Ni much more quickly than the parallel, slow reduction of Fe_2O_3 to Fe[74,75]. After the rapid initial reduction, the resulting metallic Ni will hence readily crack CH_4 to carbon and H_2 while the iron-oxide carrier fraction is in parallel still slowly being reduced to Fe. This should result—after a fast initial reduction phase that mimics that of the monometallic Ni carrier—in a slow, second reduction phase of the physical mixture in a fashion similar to the monometallic iron carrier, accompanied by simultaneous carbon deposition on Ni, which would rapidly deactivate this fraction of the carrier mixture. Clearly, this is not the case (see Figure 19a). In fact, counter to this expectation, the mixed carriers reduce completely and almost as fast as the monometallic nickel carrier, suggesting an interplay between the two carrier fractions which, in the absence of a microscopic ("nanoscale") mixing between the two metals, can only be mediated through the gas phase.

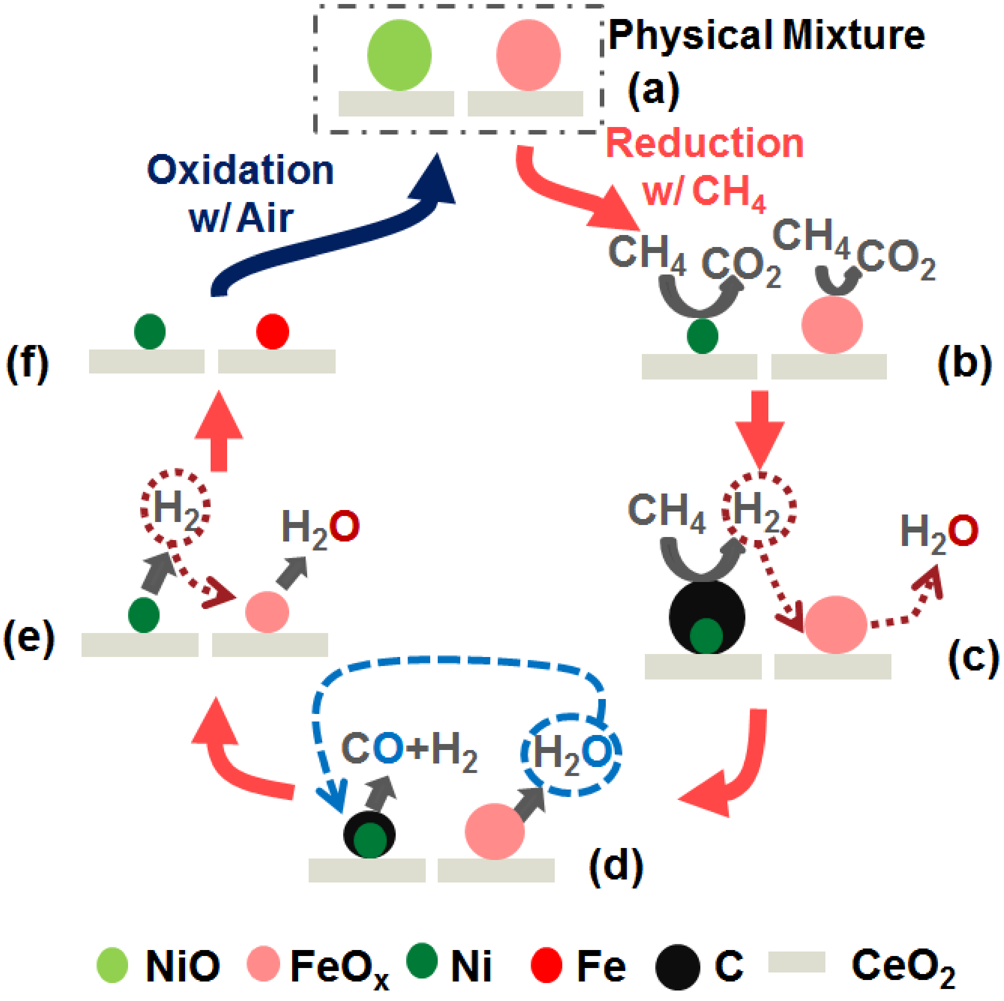

Figure 20. Proposed reaction mechanism for Fe-Ni physical mixture.

It hence seems reasonable that this interaction must occur via gaseous intermediates produced during the reduction of the individual monometallic oxides. Initially, i.e. at high carrier oxidation states, both NiO and FeO_x react with CH_4 to produce CO_2 and H_2O (Figure 20 (a) & (b)). As discussed above, NiO reduces much faster than FeO_x and hence starts cracking CH_4 to carbon and H_2. The hydrogen formed in this step has a much higher reactivity with iron oxides than CH_4, hence drastically accelerating their reduction (Figure 20 (c)). The steam formed during the reduction of iron oxide with H_2 then results in gasification of the carbon deposited on the Ni, thus continuously regenerating the metallic Ni and hence avoiding deactivation of the Ni carrier (Figure 20 (d)). Finally, this gasification step also results in re-generation of the H_2 which continues to reduce the iron oxide carrier (Figure 20 (e)). It should be noted that while CO_2 could conceptually play a similar dual role as gasification agent for carbon (being reduced to CO), followed by re-oxidation in contact with the iron oxide carrier, the slow methane oxidation over iron oxide (which would be the sole source of CO_2 after the initial NiO reduction) suggests that this reaction path is likely only a minor contributor to the overall reaction progress.

This "coordinated" reduction of the carrier can continue—at the rapid rates of Ni catalyzed methane cracking and H_2-mediated FeO_x reduction—as long as there is an oxide component present in the system, i.e. until the oxygen reservoir in FeO_x is depleted. Overall, the cooperative action of these two independent reactions—which occur over two macroscopically separated carrier fractions but are coupled via reactive gaseous intermediates (mainly H_2 and H_2O)—hence results in rapid reduction of both carriers, much in excess of the rate over the corresponding alloy carrier.

3.3.3 Validation of the proposed cooperative reaction mechanism

The validity of the proposed reaction mechanism depends on two main claims: i) The relative rates of reduction of the (monometallic) Fe carrier by H_2 is much faster than reduction with CH_4, and ii) the carbon that is deposited on Ni during CH_4 cracking is efficiently removed via gasification with steam. We hence tested these assumptions in independent experiments.

First, the monometallic iron carrier was reduced separately by three gases– H_2, CO, and CH_4 in a TGA at 800^oC. A comparison of the rates of reduction (Figure 21a) shows that reduction of the monometallic Fe carrier occurs indeed at the fastest rate by H_2 (~2-3 times faster than the rate of reduction with CH_4 in the initial reduction phase (t<2 min), and ~10-times faster in the later reduction phase), followed by CO, which is ~1.5 times and ~5 times faster than CH_4, respectively, (but likely plays a minor role in the process, as discussed above), and finally the slow rate of reduction with CH_4. This result hence confirms the first key assumption of the proposed reaction mechanism.

Next, we tested the hypothesis that the physical mixture of Ni- and Fe-based carriers results in efficient gasification of carbon deposits on Ni by H_2O, suppressing carbon accumulation and subsequent Ni deactivation. Towards this purpose, the physical mixture (88% Fe + 12% Ni) was reduced with CH_4 in a fixed bed reactor and then re-oxidized in air. Figure 21b shows the product trace during re-oxidation. The very small peaks of CO/CO_2 that are detected indicate absence of significant carbon deposition on the carrier during the previous reduction half cycle. Next, a structured bed was prepared in which the upstream part of the bed consisted of a (monometallic) NiO-CeO_2 bed followed by a (monometallic) Fe_2O_3-CeO_2 bed, packed at the same 12:88 ratio as the (random) physical mixture before. Again this structured bed was reduced in CH_4 until the partial oxidation products CO and H_2 (which follow the initial production of total oxidation products over the fully oxidized carriers in both cases) leveled off, and the bed was then again oxidized with air. As shown in Figure 21c, about 10-times more CO and CO_2 was formed during the oxidation phase, indicating an increase on coke formation by about an order of magnitude in comparison to the random physical mixture. Similarly, in contrast to the physical mixture, TEM of the reduced carrier in the structured bed showed presence of carbon nanofibers (capped by Ni nanoparticles), as typical for methane cracking on Ni[74-78]. Again, this observation is consistent with the suggested reaction mechanism, as the separation of the two metals in the structured bed minimizes contact between the (upstream) Ni-fraction of the bed with the steam formed over the (downstream) Fe-carrier.

Overall, the experimental evidence hence supports the proposed mechanism of a gas-phase mediated coupling between rapid methane cracking over Ni followed by equally rapid reduction of iron oxide with H_2. The steam formed in the second step then gasifies the carbon formed on Ni, keeping the reaction loop alive.

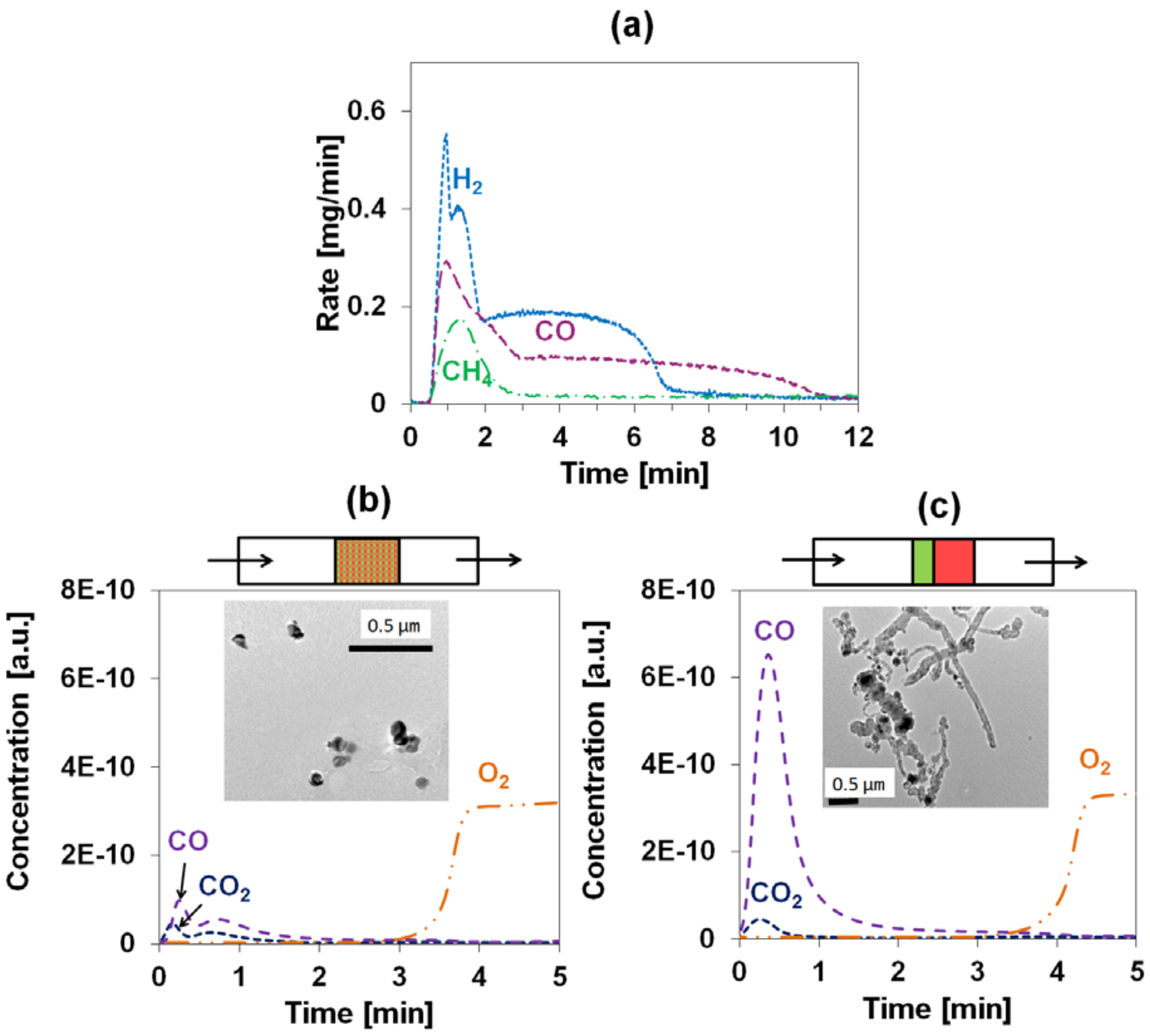

Figure 21. a) Comparison of the reduction rates for the monometallic Fe carrier in presence of either H_2 (dotted), CO (dash), or CH_4 (dot-dash) in TGA (T=800ºC), showing a drastic acceleration of the reduction with H_2 compared to CH_4. b) Fixed-bed reactor re-oxidation of a randomly mixed Fe/Ni carrier bed, and c) of a structured bed in which Ni bed precedes a Fe bed, demonstrating a significant reduction in carbon formation for the randomly mixed bed. The insets in panels b and c show TEM images of the reduced samples, confirming the much enhanced carbon formation for the structured bed.

3.3.4 Evaluation of carrier stability

Chemical looping requires the oxygen carrier to perform a large number of consecutive reduction and oxidation operations in a robust manner at the high temperatures of operation. We first test the stability of the physically mixed carrier bed in cyclic TGA operations, using H_2 as a fuel to avoid complications due to potential carbon deposition when using CH_4 and CO_2 as an oxidant as a means of CO_2 activation via reduction to CO.

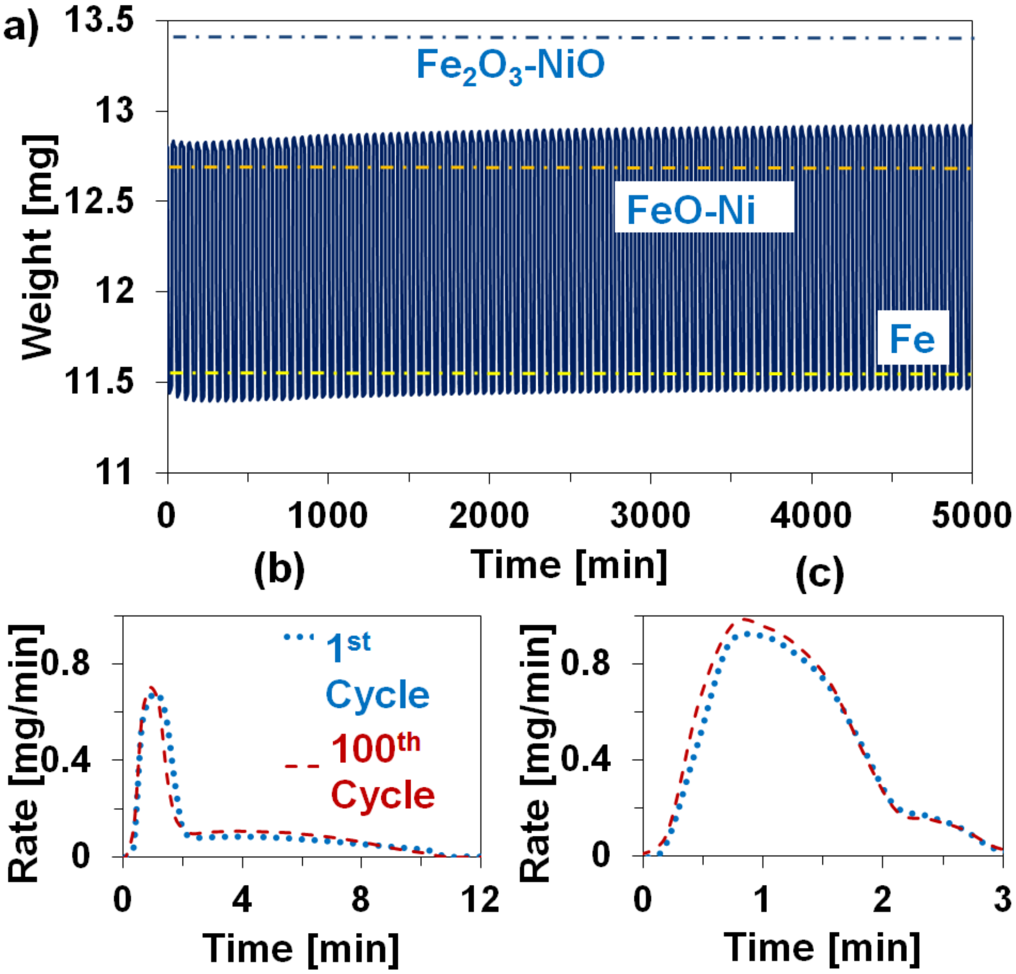

Figure 22. a) Multicycle redox experiment in TGA at 900ºC measuring weight as a function of time (H_2: 20 sccm, Ar: 20 sccm, CO_2: 20 sccm). Comparing the rates of: (b) reduction half cycle and, (c) oxidation half cycle suggest excellent stability over 100 successive cycles.

Figure 22 shows results from a multi-cycle test over 100 redox cycles at 900°C. During the reduction half cycle, H_2 reacts with the lattice oxygen to produce steam, resulting in the loss of carrier mass. The carrier reduces completely, as seen in the weight decrease down to the calculated reduced carrier weight corresponding to (Fe + Ni). The slight drop below this fully reduced weight indicates some reduction of CeO_2 which we have previously shown to be reducible a typical chemical looping operating conditions and hence able to contribute (albeit to a minor degree) to the oxygen carrying capacity of the carrier via $CeO_2 \leftrightarrow CeO_{2-x} + x/2\ O_2$[42]. During the subsequent re-oxidation of the carrier with CO_2, the sample is oxidized at a fast rate to the oxidation state corresponding to FeO-Ni. While further oxidation is possible, the rate becomes very slow and the oxidation phase is hence terminated at this point. This transition to slow oxidation is expected since CO_2—a weak oxidant—is not able to oxidize Ni and oxidizes Fe only up to Fe_3O_4 (due to thermodynamic constraints[26]), following a two-step oxidation, i.e. a fast oxidation from Fe to FeO followed by a much slower step from FeO to Fe_3O_4. We hence restrict cyclic operation to between the states of FeO-Ni and Fe-Ni for the entire experiment.

The results show excellent stability over multicycle operation (the slight upward shift over time is due to instrument drift over the course of the experiment). In particular, the rates of reduction and oxidation for the first and the last cycle, which tend to be highly sensitive indicators of deactivation, are essentially unchanged (Figure 22b & c). Furthermore, the carrier sample shows no sign of sintering over these cycles with average crystallite size (determined via XRD) remaining unchanged at ~39nm. Most significantly, we find no sign of alloy formation via cross-contamination of the two monometallic carriers, which could significantly alter reactivity: XRD analysis after the cyclic experiment shows only distinct phases of Fe_2O_3 and NiO **(**Figure 23).

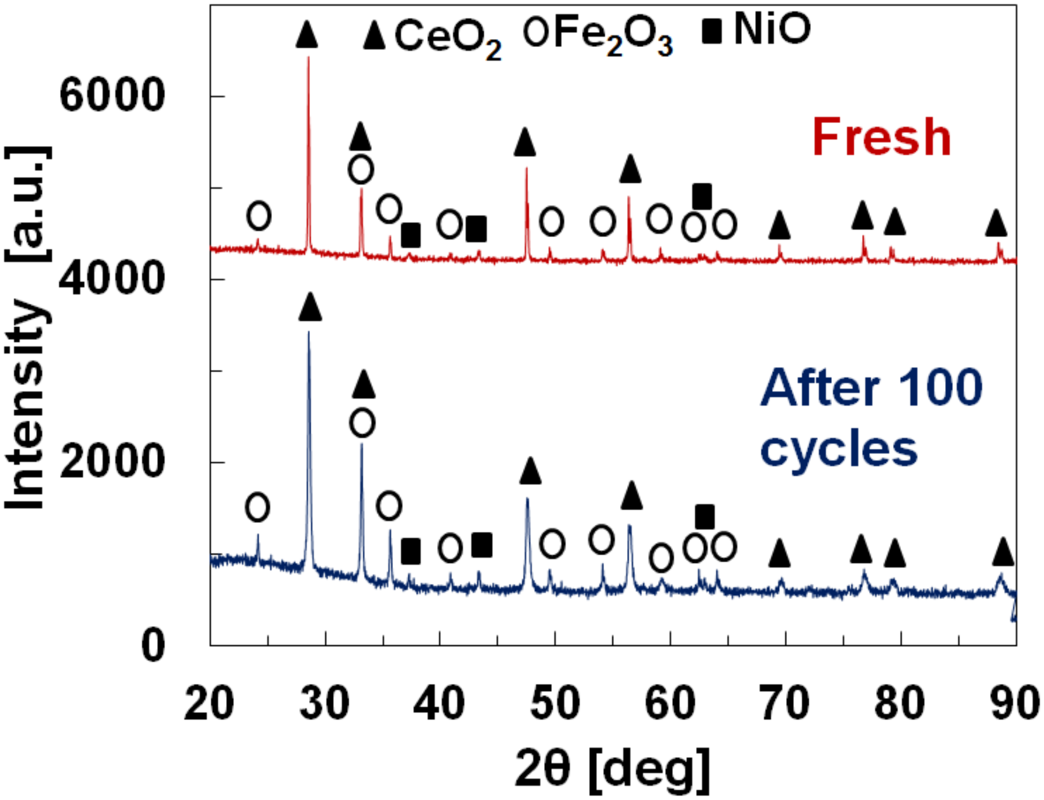

Figure 23. XRD patterns of a physical mixture of 88% Fe + 12% Ni carrier (oxidized in air) before and after multi-cycle TGA experiments. Detection of only separate phases for Fe and Ni confirm absence of unintended alloying due to potential cross-contamination during cyclic operation.

3.3.5 Reactive evaluation in a fixed bed

Following these tests, the stability and selectivity of the carrier in cyclic redox operation with CH4 as fuel was tested in fixed-bed experiments at 900°C. Earlier work had shown that nickel-based carriers are selective only towards total oxidation of CH_4, while the selectivity of iron-based carriers depends on the oxidation state of iron[46]. For the physically mixed carriers, it is expected that the co-operative gas phase mechanism will significantly change the effective overall selectivity as a function of the relative fractions of iron and nickel carrier present in the mixture by coupling between these two monometallic carriers through gas phase intermediates.

As a first step, we hence screened the activity and selectivity of these physical carrier mixtures as a function of Ni:Fe mixing ratio. In order to gain further insight into the importance of the oxidation state of the carrier for activity and selectivity, we conducted cyclic tests both with air and CO_2 as oxidants. Results are summarized in Figure 24.

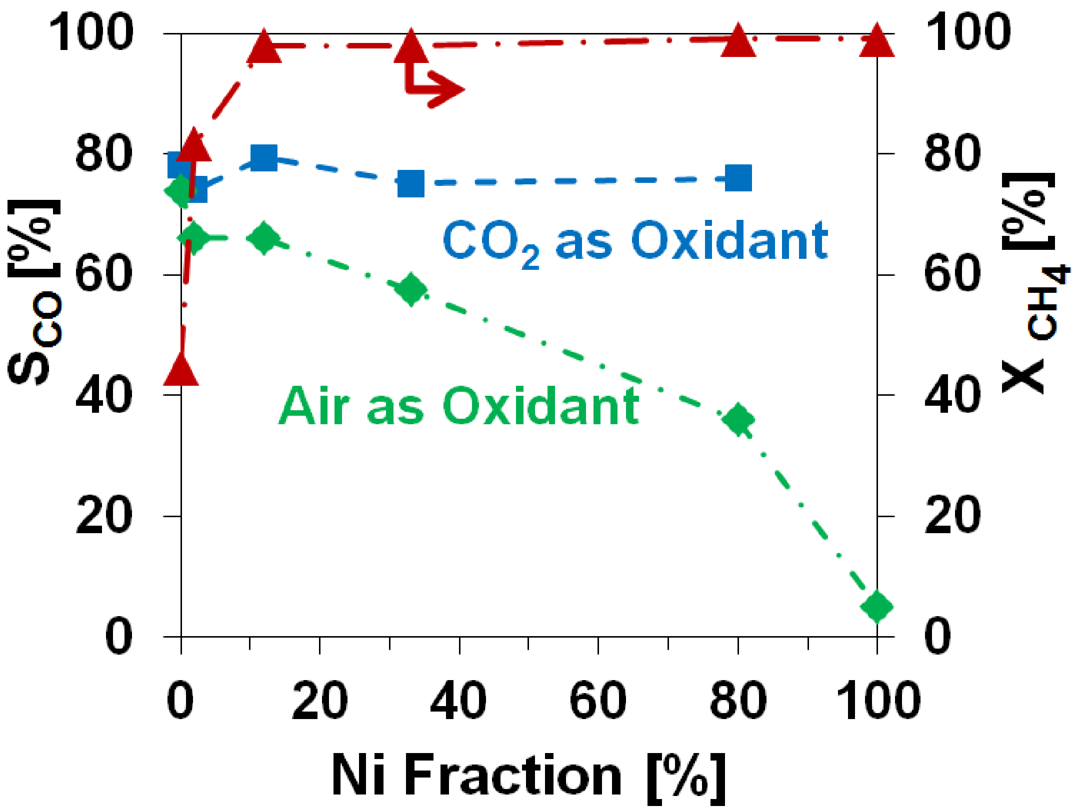

Figure 24. CH_4 conversion (X_{CH4}; triangles) and CO selectivity (S_{CO}; squares for CO_2 oxidation and diamonds for air oxidation, respectively) as a function of Ni fraction for a Fe-Ni physical mixture in a fixed bed reactor at 900°C with CH_4 (1 sccm, 16.7 vol%). The oxidant (air or CO_2) used before reaction with methane has no impact on conversion but strongly impacts selectivity.

Interestingly, methane conversion follows identical trends between the two experiments: Pure Fe carriers show relatively low reactivity with methane and hence low conversion. However, even a small amount of Ni carrier in the mix increases methane conversion dramatically, and in both cases methane conversion is near complete (>95%) for carrier mixtures with >10% Ni. This again reflects the very high reactivity of Ni for methane activation. The fact that the nature of the oxidant plays no significant role, despite the fact that the Ni carrier is oxidized to NiO after oxidation with air but remains reduced (Ni) after oxidation of the bed with CO_2, is in agreement with our earlier finding that the reactivity of Ni supported on ceria does not vary significantly as a function of oxidation state[42]. It also indicates that the role of the Fe carrier for methane conversion is insignificant, as the Fe fraction of the carrier bed is fully oxidized to Fe_2O_3 after oxidation with air but only to FeO after oxidation with CO_2, and the activity of Fe/ceria carriers show a more pronounced dependence of activity on degree of oxidation[41].

In contrast to conversion, the CO selectivity (which represents overall syngas selectivity in these graphs) shows a significant difference between the experiments with the two different oxidants (CO_2 and air): For oxidation with CO_2, which only oxidizes Fe to FeO and leaves Ni in the metallic state, CO selectivity remains essentially unaffected by the Ni content in the bed. While surprising at first, this is in fact fully consistent with the gas-phase mediated cooperative mechanism that we proposed earlier: If methane is cracked over Ni, and subsequent oxygenate formation occurs via oxidation of H_2 with the oxidized Fe carrier and gasification of the carbon deposit on Ni, the product spectrum will not be affected by the oxidation state of the carriers as long as Ni remains in its metallic state, i.e. the oxidation state of the Fe fraction is irrelevant for the syngas selectivity. The relative amounts of Ni:Fe are furthermore irrelevant as long as oxygen is available in the Fe carrier.

Conversely, this suggests that as soon as Ni is being oxidized the process selectivity should drop, since the overall reaction mechanism changes from methane cracking over Ni to methane oxidation over NiO. The latter, however, is highly unselective and produces essentially no partial oxidation products. This expectation is directly reflected in the experimental results, which show a steep drop in CO selectivity with increasing Ni content when using air as oxidant, and a convergence of the selectivities for the experiments with air and CO_2, respectively, for low Ni content in the bed[42].

Overall, these results confirm the proposed coupling mechanism between the two monometallic fractions in the carrier bed, and suggest that a carrier bed with a majority of Fe carrier is preferable not only from a cost and toxicity perspective, but also in order to maximize syngas yields. Use of CO_2 as oxidant furthermore raises selectivies from ~70% (for air as oxidant) to ~80%.

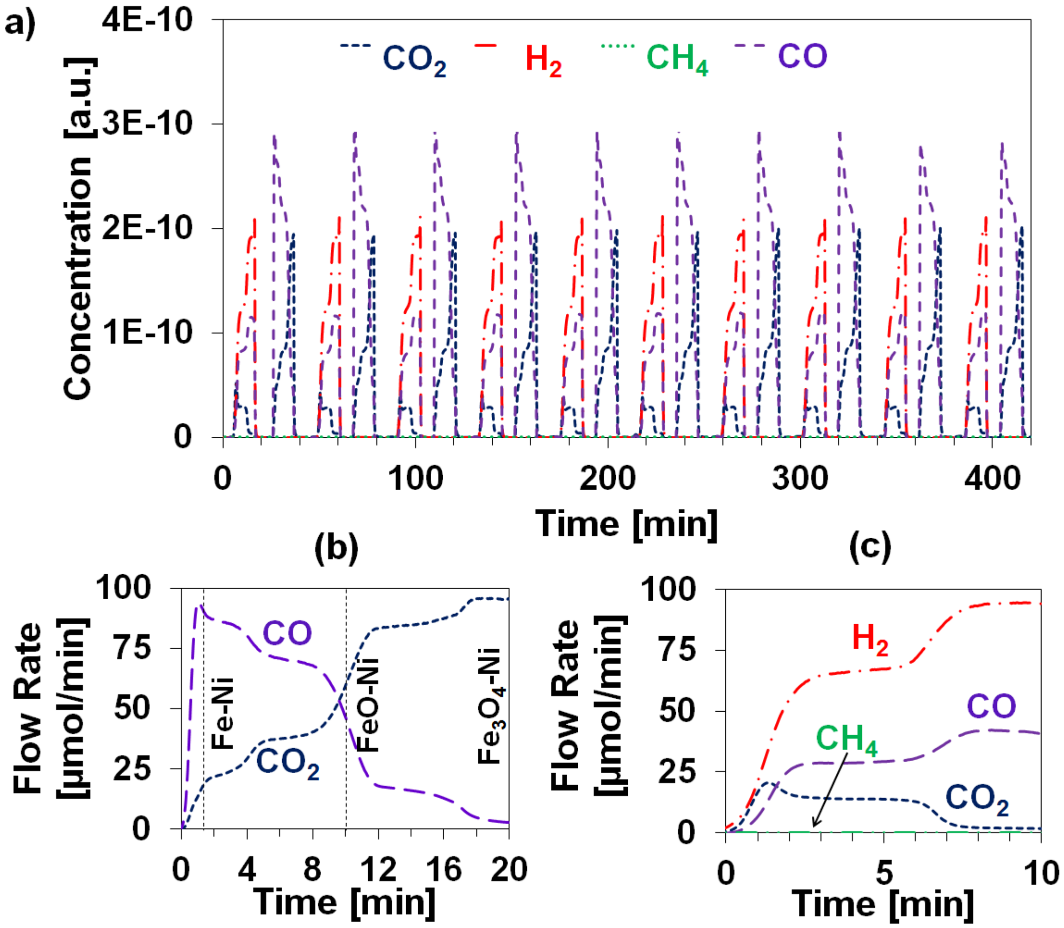

Figure 25. a) Multicycle operation of Fe (88%) + Ni (12%) carrier in a fixed bed reactor at 900°C with CH_4 as fuel (1sccm, 16.7 vol%) and CO_2 as oxidant (3sccm, 37.5 vol%), b) Oxidation of the reduced carrier by CO_2 shows step wise change in the amounts of CO produced. During the cyclic experiments, the carrier oxidation was stopped at t =11min which corresponds to the carrier in the FeO-Ni oxidation state, and c) typical reduction half cycle shows the flow rate traces of the products formed over the oxidized carrier.

Based on these results, we selected the 88% Fe + 12% Ni mixture (which shows the highest syngas yields) for deeper evaluation. Figure 25a shows ten periodic cycles at 900°C with

CH_4 and CO_2 as fuel and oxidant, respectively. Periodic operation was optimized by terminating each reduction half cycle as soon as the CO concentration peaked and started dropping (suggesting that the oxygen reservoir in the Fe carrier was nearing depletion) in order to avoid CH_4 cracking and subsequent carbon carry over. During oxidation, the CO_2 flow was stopped as soon as the rate of oxidation dropped i.e. the carrier oxidation was restricted to the fast oxidation regime (as discussed earlier). To confirm the carrier oxidation states, an extended re-oxidation of Fe-Ni by CO_2 was conducted **(**Figure 25b**).** Initially large amounts of CO are detected along with some unconverted CO_2 followed by a step wise change until negligible amounts of CO are detected. Since oxidation of Ni by CO_2 is thermodynamically limited[26] and Fe can only be oxidized with CO_2 up to Fe_3O_4[57], the physical mixture is in a Fe_3O_4-Ni state when CO production has completely stopped (t = 20min). Using a mass balance, the time points corresponding to the other oxidation states of iron, i.e. Fe and FeO, were calculated and are indicated by vertical dotted lines. Based on these criteria, a reduction time of 10 min and oxidation time of 11 min was determined and used in the multicycle experiments.

The stability of the carrier is reflected in the constant height and shape of the concentration time traces over the ten cycles in this experiment (Figure 25a). At the start of reduction (Figure 25c), CO and H_2 are formed right away at high concentrations, whereas a comparatively small amount of CO_2 is formed in parallel, likely as a result of water-gas shift between H_2O and CO (both Fe and Ni are well-established WGS catalysts). No CH_4 is detectable throughout the cycle indicating very high methane conversion (>99%). It is likely that further improvement in the process parameters can be achieved by optimizing reactor operation. However, such process optimization was not the target of this proof-of-concept study. Nevertheless, the present configuration resulted in excellent methane conversions (>99%) and good syngas selectivity (~68%) with a H_2:CO ratio of ~2.2, i.e. close to the typically desired ratio for downstream processes such as Fischer-Tropsch or methanol synthesis.

3.4 CONCLUSIONS

Recent surge in natural gas production has renewed interest in its industrial utilization to produce value added products. Currently, any utilization route proceeds via syngas a intermediate, i.e. it requires methane reforming or partial oxidation as an initial, highly capital and energy intensive step. We have recently demonstrated that chemical looping can be used to produce syngas from methane via "chemical looping partial oxidation of methane" (CLPOM)[46] and via "chemical looping dry reforming" (CLDR)[26,57], i.e. the chemical looping equivalents of the conventional partial oxidation and dry reforming processes. Both processes were shown in those studies to proceed particularly efficiently over Fe/Ni alloy catalysts, using a reducible (ceria) support. The sensitive control of selectivity via adjusting the Fe:Ni ratio in the alloy indicated the large potential that multimetallic carrier materials might hold for selective oxidation processes via chemical looping. However, the complexity of supported multimetallic redox systems also makes prediction and hence rational a-priori design of such carriers a formidable task.

In the present study, we demonstrate that, surprisingly, the use of simple physical mixtures of two monometallic carriers can yield similar synergies, albeit based on a completely different coupling mechanism: While the alloy carriers in our earlier studies relied on the "shared" use of lattice oxygen between the coexisting metals in the oxide lattice, the physical mixture relies on a gas-phase mediated cooperative mechanism, where the initial activation of one reactant over the first metal is coupled with the subsequent conversion of the intermediates over the second metal. The product from this secondary conversion is then undergoing another reaction step, forming the final product. Specifically, for the present system, we demonstrated that methane is activated via cracking over Ni, resulting in the formation of (solid) carbon and H_2. The intermediate H_2 is then oxidized in contact with Fe_xO_y, and the produced steam then gasifies the carbon on Ni, resulting in the formation of the final products CO and H_2. The overall coupled process allows combination of the high methane activation rates over Ni with the good syngas selectivity over Fe oxides, resulting (without detailed process optimization) in near-complete methane conversion with syngas yields of ~70%.

On a conceptual basis, it seems worthwhile to point out that H_2 effectively acts as a gas phase catalyst, which catalyzes the reduction of the iron oxide and then gets re-formed from H_2O in the gasification of carbon. The present process hence constitutes an intricate coupling of two “nested” catalytic cycles (see Figure 26): Over the entire cyclic process, the proposed net reaction is a metal (oxide) catalyzed dry reforming reaction, broken down into two half steps. Nested into this, the reduction half cycle contains a gas-phase catalyzed solid state reaction in which carbon is effectively oxidized with lattice oxygen from iron oxide with steam (and possibly, to a minor degree, CO_2), which hence play the role of “gas phase oxygen carriers”.

The use of simple physical mixtures in place of alloys is not only cheaper, but opens another window for rational process design which can build on an ever increasing number of published studies on (monometallic) oxygen carriers in chemical looping oxidation processes and on the availability of thermodynamic databases for a large number of metal/oxide systems. We hence expect that this approach will find application to many other combinations of metals and a family of closely related selective oxidation reactions.

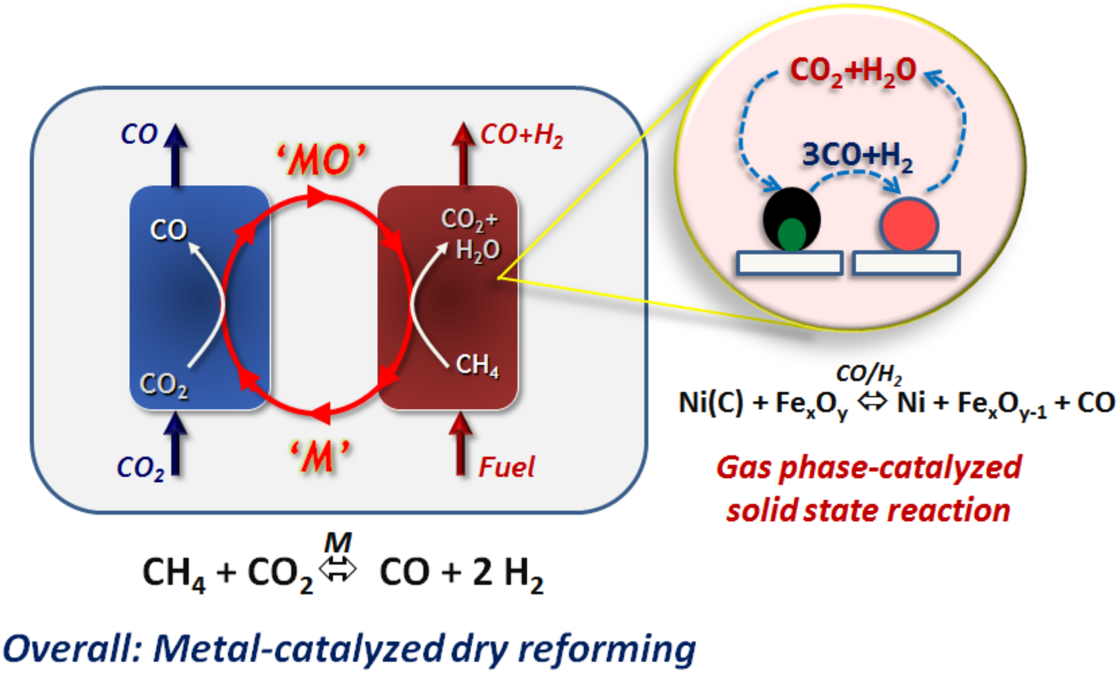

Figure 26. Schematic representation of the two "nested catalytic loops" in the present process: The overall process (left) constitutes a metal (oxide) catalyzed dry reforming reaction, while the reduction half cycle is driven by a gas phase catalyzed solid state reaction between carbon and lattice oxygen from the iron oxide carrier.

4.0 DOPED CERIA SUPPORTS FOR CHEMICAL LOOPING PROCESSES

4.1 INTRODUCTION

The use of reducible supports has been well established in the field of heterogeneous catalysis where reducible oxides, and in particular ceria, are widely used as support for metal nanoparticles in various catalytic redox reactions[79] , including automotive exhaust clean-up (catalytic convertor)[80], water gas shift reaction[81,82] and catalytic methane oxidation[83-85]. It is understood that the promotional effect seen with use of ceria as support is due to strong metal-support interaction[86] and its oxygen buffering capacity, i.e., the facile and reversible release of lattice oxygen via the $Ce^{4+} \Leftrightarrow Ce^{3+}$ transformation[87]. Drawing the analogy between catalysis and CLC on the basis of similar promotional effects, ‘oxygen mobility’ in the support structure of oxygen carrier is crucial for effective utilization of the supported metal. Furthermore, it is well known that the oxygen mobility and oxygen storage capacity in such reducible oxides is a strong function of concentration of oxygen defects in the support structure[88]. Therefore, one can expected that the reactivity of oxygen carriers can be further enhanced by introduction of extrinsic oxygen defects in ceria via doping.

Doping ceria with cations that have smaller ionic radii than Ce^{4+}, such as zirconia (Zr^{4+})[83,89], or with aliovalent dopants such as La^{3+} [84,88] has indeed been reported to promote its redox properties by facilitating oxygen transport in the ceria lattice, where a strong relation between concentration of oxygen defects and oxygen carrying capacity exists[81,90]. Such doping is also known to improve the thermal stability/textural properties of the support oxides[83,84,88,89,91]. Based on work reported in fuel-cell community, the effective dopant size is shown to have a crucial impact on the ionic/oxygen transport and hence the overall electrochemical performance[92]. Inaba and Tagawa show that there exists a critical dopant radius viz. 0.111nm for divalent dopants and 0.104nm for trivalent dopants[93]. This was further correlated with association enthalpy– the energy tax to introduce a dopant into the ceria lattice– which is minimized as a function of the dopant radius[94,95].

However, the effect of ceria doping on redox kinetics and/or carrier stability has not found significant attention in the context of chemical looping to-date. A sole study from the Chalmer's group[96] aimed at investigating the effect of using ceria and 10% Gadolinia-doped ceria (in comparison to conventional non-reducible alumina support) for iron-, copper-, and manganese-based carriers. The authors report that doped ceria particles were more reactive than pure ceria. However the effect of dopant nature on redox behavior, carrier stability, and oxygen carrying capacity of oxygen carriers in CLC was not considered – a significant factor towards understanding the mechanistic functioning of such doped carriers as well as towards determining the optimum dopant required to observe the enhancement effects. In the concentrated solar power (CSP) community, doped ceria has also found some attention recently: Haile and coworkers tested 15% samarium-doped ceria for solar-thermal H_2O and CO_2 splitting chemistry[97], but determining the optimal dopant concentration was again not in the scope of the reported work. In related studies, Li et al. investigated mixed-oxides of Fe-Ce for chemical looping, combining the role of the active metal and the dopant[98,99]. However, poor stability of iron in the ceria lattice and subsequent bleed-out of iron as a separate phase upon heat treatment at high temperatures limited the stability of the carrier and precluded deeper mechanistic insights and derivation of composition-activity correlations. Therefore, a clear understanding for doped ceria based materials in their application to chemical looping processes is lacking to-date.

We have recently reported that addition of La to CeO_2 can strongly influence the redox kinetics of the supported "active" phase–iron oxide[100]. A balance between enhancement of oxygen mobility and lowered reducibility upon formation of a lanthana phase results in a strongly nonlinear dependence of carrier reactivity on the dopant concentration and gives rise to an optimum at low dopant concentrations. Building on this initial work, we hypothesize that the dopant type (i.e. ionic size as well as chemical nature) can further influence the enhancements in oxygen mobility, depending on the degrees of association in the ceria lattice.

4.2 EXPERIMENTAL SECTION

4.2.1 Material Synthesis

The main focus in the synthesis of doped ceria (dopants: Pr, Sm, Gd & La) was not only to attain solid solution of dopant (D)–Ce but also on simplicity of the synthesis procedure to keep the cost of the resulting material low and hence realistic for industrial application. Oxygen carriers were synthesized using a simple and scalable two-step approach. First, doped ceria is synthesized, and then iron is subsequently deposited on the D_x-$Ce_{1-x}O_{2-x/2}$ support by deposition–precipitation.

$D_xCe_{1-x}O_{2-x/2}$ supports with different D concentration (x = 0.02 & x = 0.1) were prepared via a facile hydrothermal synthesis procedure previously adapted in our research group[81]. For example, $La_{0.1}Ce_{0.9}O_{1.95}$ was synthesized by dissolving 0.675 g of $Ce(NO_3)_3 \cdot 6H_2O$ (99+%, Sigma–Aldrich) and 0.075 g of $La(NO_3)_3 \cdot 6H_2O$ (99+%, Sigma–Aldrich) in 8 ml DI water. 30 ml of NaOH (98+%, Sigma–Aldrich) solution (7 M) was rapidly added under vigorous stirring. After 30 min of stirring, the slurry was transferred into a 50 ml autoclave, heated to 100 °C under autogenous pressure for 72 h, and then allowed to cool to room temperature. The product was washed with DI water and collected via centrifugation to remove any ionic remnants until the pH of the solution was 7. Finally, the resulting powder was dried at 100 °C overnight and calcined at 450 °C for 2 h.

Next, Fe-based carriers were synthesized by deposition–precipitation. Briefly, $Fe(NO_3)_3 \cdot 9H_2O$ (99+%, Sigma–Aldrich) was dissolved in DI water, and 40 mL of the 0.06 M precursor solution was precipitated by 0.5 M NaOH at pH of 9–9.5 on 200 mg of the desired support powder suspended in 100 mL DI water. After aging for 2 h, the resulting precipitate was centrifuged, vacuum dried at 100 °C, crushed and finally calcined in air at 900 °C for 2 h in air.

4.2.2 Characterization

X-Ray Diffraction Characterization: To confirm the phases present, the synthesized carriers were first analyzed via powder X-Ray diffractometry (Bruker D8) operating at 40kV and 40mA with Cu Kα radiation (λ=1.5418 Å). The data was recorded between 2ϴ values of 20^o and 90^o with a scanning rate of 3.5^o/min. The XRD pattern was smoothed with a FFT filter. The phases were identified using the JCPDS database. Average crystallite size was calculated using the Scherrer equation.

Surface Area and Pore Volume: BET (Brunauer-Emmett-Teller) surface area determination was conducted via Nitrogen adsorption/desorption in a Micrometrics ASAP 2020 gas adsorption analyzer. The samples were pretreated by degassing under vacuum for 2hr at 200°C. All the samples considered in the study had low surface areas of < 5 m^2/g as expected due to initial sintering of the materials.

Electron Microscopy: A High Resolution-Transmission Electron Microscopy (HR-TEM) JOEL JEM-2100F was used to image the particles and conduct EDAX mapping. Bulk metal weight percentages and metal dispersion of the synthesized samples were confirmed by Energy Dispersive X-Ray Analysis (EDAX) performed using an Oxford INCA EDS system attached to a JSM-6510LV SEM.

4.2.3 Reactivity Tests

Solid-Phase Conversion: Carrier conversion was determined in a Thermo-Gravimetric Analyzer (SDTQ600, TA instruments). 10-15mg of the carrier powder were loaded into the instrument. The temperature was ramped up to the reaction temperature at 100°C/min and then held there isothermally for the experimental duration. The gases used were: N_2 (Grade 5, 100sccm), Ar (Grade 5, 20sccm), H_2 (Grade 2, 20sccm) CH_4 (Grade 2, 5sccm) and CO_2 (Grade 2, 20sccm). The carrier gas (N_2) is flown continuously throughout the experiment. The reactive gases H2/CH_4 and CO_2, are used for the reduction and oxidation of the carrier respectively. The purge gas (Ar) is used to flush the system between consecutive reduction and oxidation cycles. For comparison between the various carriers carrier conversion was defined as follows:

$$Carrier\ Conversion = \frac{Sample\ Weight - Reduced\ Weight}{Oxidized\ Weight - Reduced\ Weight}$$

Eq. (16)

The different oxidation states of the sample were calculated by a simple mass balance from the oxidized weights.

Gas-Phase Reactivity: Conversion of the fuel (CH4) and product selectivity was determined using a fixed bed reactor set-up. 100mg of the carrier was packed between two glass wool plugs in a horizontal quartz tube (1/4” ID) enclosed by a furnace (Thermo electron corporation-Lindberg/Blue M). The reactant gases were fed via mass flow controllers at the following flow rates: Ar (99.995%, 5 sccm as a reference for calculations flown throughout the experiment and 20 sccm as purge between cycles), CH_4 (99.995%, 1 sccm) CO_2 (99.999%, 1 sccm) and O_2 (99.999%, 1 sccm). The outlet gas concentrations were measured by a mass spectrometer (Pfeiffer Omnistar QMS 200) and the corresponding molar flow rates (ni) were calculated.

Carbon Balance:

$$n_{CH_4,in} = n_{CH_4,out} + n_{CO_2,out} + n_{CO_{out}} + 0.5 \times (n_{H_2,out} - 2n_{CO_{out}}) \qquad \text{Eq. (17)}$$

On-stream methane conversion (X_{CH4}) and cumulative carrier ($X_{carrier}$) conversion were evaluated using:

$$X_{CH_4} = \frac{n_{CH_4,in} - n_{CH_4,out}}{n_{CH_4,in}}\,, \qquad X_{Carrier} = \frac{4\sum n_{CO_2,out} + \sum n_{CO,out}}{Total\ mol\ of\ O\ in\ carrier}$$

Eq. (18), (19)

Selectivity of various species (S_i) viz. CO_2, H_2, CO and carbon (C) formation by methane pyrolysis was calculated by the following equations.

$$S_{CO_2} = \frac{n_{CO_2,out}}{(n_{CH_4,in} - n_{CH_4,out})}\,, \qquad S_{CO} = \frac{n_{CO_{out}}}{(n_{CH_4,in} - n_{CH_4,out})}$$

Eq. (20), (21)

$$S_{H_2} = \frac{0.5n_{H_{2,out}}}{\left(n_{CH_{4,in}} - n_{CH_{4,out}}\right)}\ , \qquad S_{Carbon} = \frac{0.5\left(n_{H_{2,out}} - 2n_{CO_{out}}\right)}{\left(n_{CH_{4,in}} - n_{CH_{4,out}}\right)}$$

Eq. (22), (23)

$$X_{Carrier} = \frac{4\sum n_{CO_{2,out}} + \sum n_{CO_{,out}}}{Total\ mol\ of\ O\ in\ carrier}$$

Eq. (24), (25)

As expected, we find that complete combustion, partial oxidation and catalytic pyrolysis of methane are the dominant reactions occurring with the metal oxide (MO):

Complete Combustion: $CH_4 + MO = CO_2 + H_2O + 4M$ (R8)

Partial Oxidation: $CH_4 + MO = 2H_2 + CO + M$ (R9)

Methane Pyrolysis: $CH_4 + M = M + C + 2H_2$ (R10)

4.3 RESULTS AND DISCUSSION

4.3.1 Stability of dopant-ceria solutions

In order to study the effect of various dopants on carrier reactivity, it is essential to first confirm the successful formation of the mixed oxide ($D_xCe_{1-x}O_{2-x/2}$) upon synthesis and further, on deposition of iron. Therefore, the mixed oxides calcined at 450°C, were first subjected to X-ray diffraction to test for possible co-existence of separate ceria and dopant phases which would indicate incomplete incorporation of the dopant into the ceria lattice.

Upon doping Ceria with various dopants (i.e. Pr, Gd, Sm and La), no separate peaks for the respective oxides (PrO_2, Gd_2O_3, Sm_2O_3 and La_2O_3) are detected. The primary peak CeO_2 ($\theta = \sim 28.5^o$) for all the mixed oxides is further compared in Figure 27a. Once again, the vertical dotted line represents the standard X-ray diffraction angle for pure CeO_2. The peak positions for the Pr-, Gd- and Sm- doped supports is virtually unchanged as compared to CeO_2. However, the corresponding peak for La- doped CeO_2 is shifted slightly to lower reflection angles suggesting a partial incorporation of La in the CeO_2 lattice. The peak positions also allow for calculation of the lattice parameters of these support oxides. The dopants La, Sm and Gd are all typically present in the 3+ oxidation state when doped in ceria[91,101,102] and have ionic sizes which are larger than that for Ce^{4+}[103]. It was anticipated that the lattice parameter of CeO_2 would increase, when the dopants with larger ionic sizes viz. Gd^{3+}, Sm^{3+} and La^{3+}, partially substitute cerium atoms in the CeO_2 lattice. Figure 27b shows the average lattice parameters of the various doped oxides as a function of the dopant radius. The calculated lattice parameters for the doped supports increased as compared to the undoped ceria. Moreover, the lattice parameters roughly followed the same trend as the (increasing) ionic radii of the dopants. However, the lattice parameter of Pr-doped ceria is a clear outlier with a smaller lattice parameter despite having a larger dopant radius. This can be explained considering the multivalent nature of Pr– it can be present in the oxidation state of 3+ (majority) as well as 4+ (minority) [104-106]. Moreover, the ionic radius of Pr^{4+} (0.096nm) is very close to that of Ce^{4+} which will potentially result in the overall lattice parameter of the Pr-doped being smaller than expected. Overall, the absence of additional phases of the dopants in the X-ray diffraction patterns can be considered proof enough to confirm the successful formation of mixed oxides.

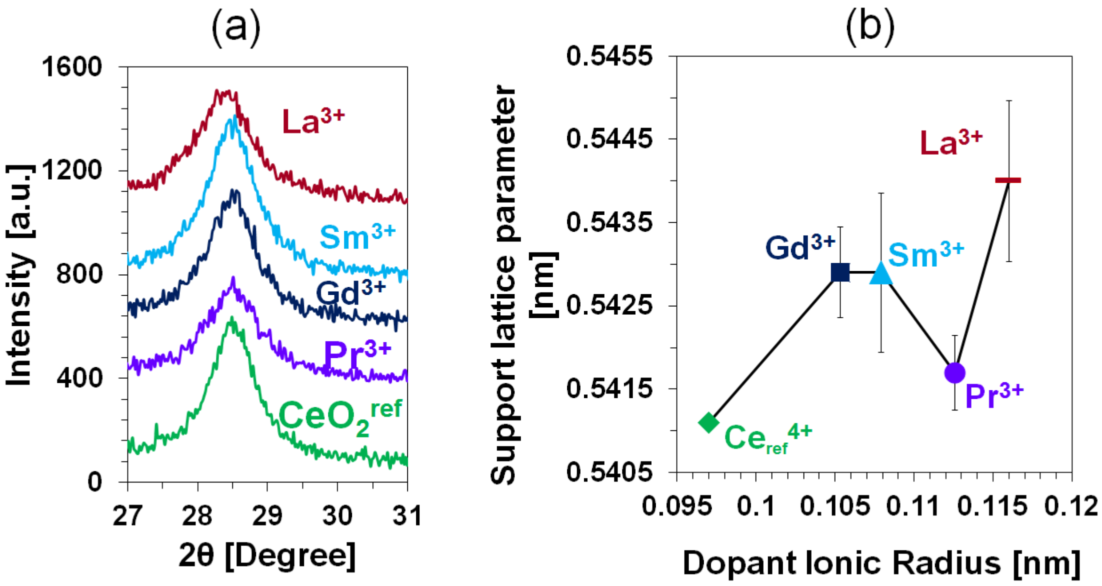

Figure 27. a) X-ray diffraction peaks for ceria (θ = ~28.5°) on addition of various dopants (D^{n+} where D is the dopant, n is the valence) calcined at 450°C in air, show the peak position did not change due to the incorporation of the dopants. b) The average lattice parameter calculated for each of the mixed oxides and plotted against the dopant radius, show a slightly increasing trend.

Upon confirmation of the formation of homogeneous solid solutions of ceria and dopants for all samples, iron was deposited onto the support powders via deposition–precipitation, and the obtained materials were calcined at 900°C. Figure 28 shows typical X-ray diffraction patterns for all Fe–$D_xCe_{1-x}O_{2-x/2}$ carriers after calcination at 900°C. For all the samples, the peaks for Fe_2O_3 are detected in addition to CeO_2. However, for the La- doped sample, XRD shows the appearance of low intensity peaks which indicate formation of $LaFeO_3$. This is expected and has been reported in a previous study done in our lab[100]. The strong interactions between lanthana and iron possibly provide a strong driving force for bleed-out of lanthana which was stable in the ceria structure prior to iron loading. Overall, our results show that for all dopants except La, there is no noticeable interaction between the iron and the dopants which further allows the dopants to remain incorporated in the solid solution.

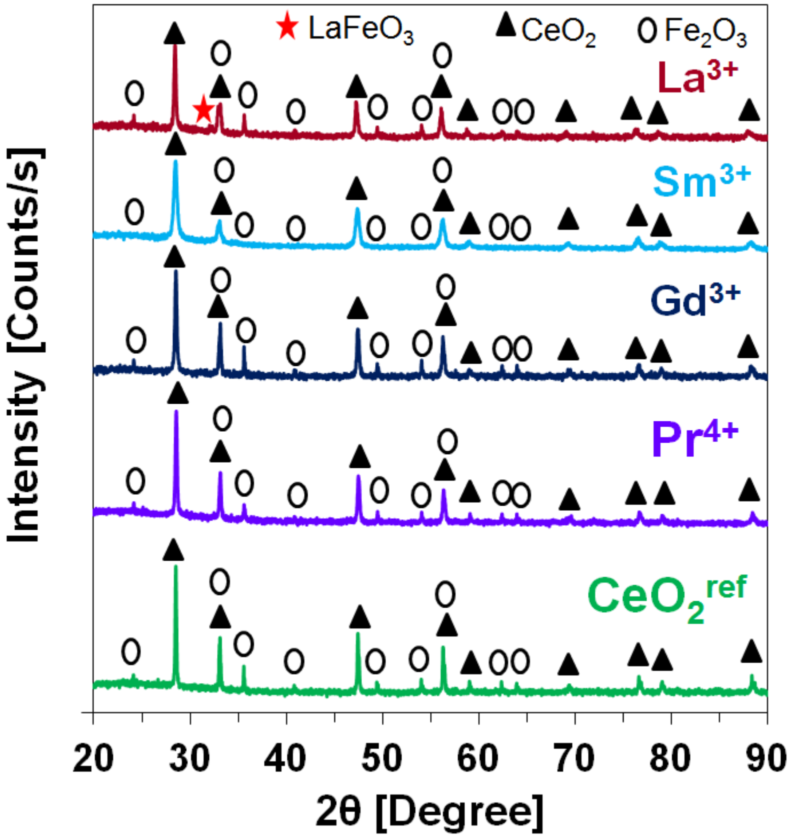

Figure 28. X-ray diffraction patterns of Fe-$D_xCe_{1-x}O_{2-x/2}$ (where D is the dopant) calcined in air at 900ºC for various dopants showing that only La reacts with the supported iron to form a separate phase.

4.3.2 Reactive tests in TGA

After establishing the thermal stability of the oxygen carriers at non-reactive conditions, all carrier materials were subjected to redox cycling in a thermogravimetric analyzer (TGA) at 450^oC. CLC operation was simulated by periodically switching between fuel (carrier reduction) and air (oxidation), separated by a purge phase to avoid direct contact of fuel and oxidizing gas. The aim of these studies was to understand the redox kinetics of the carriers as a function of dopants in the support. Therefore, H_2 was used as model fuel to avoid complications arising due to multiple parallel and sequential reaction pathways in the oxidation of methane, including carbon deposition due to fuel pyrolysis.

Figure 29a shows a redox cycle for the Fe-$Pr_{0.1}Ce_{0.9}O_{1.95}$ carrier in the TGA at 450^oC. The carrier shows rapid loss of oxygen (i.e. reduction) upon exposure to hydrogen. The horizontal dotted lines show the sample weight that corresponds to various oxidation states of the carrier during redox operation i.e. Fe_2O_3, Fe_3O_4, FeO and Fe. It is worth noticing that the various bends in the weight trace agree to an extent with the various oxidation states, suggesting that the rates of reduction are dependent on the oxidation state transitions. The sample weight obtained in the reduced state of the carrier is the expected weight due to full reduction of the iron phase in the carrier (depicted by the bottom-most dotted line in Figure 29a), indicating the complete reduction of the carrier.

Previously, we had observed that the use of (undoped) reducible supports yields very limited contribution to the oxygen carrying capacity; however, the oxygen mobility in the support structure resulted in fast redox kinetics and facilitated complete utilization of the supported metal[42]. Therefore, the impact of doping on the redox kinetics of the overall carrier was evaluated by calculating the rate of reduction of the oxygen carriers. Figure 29b shows the absolute reduction rate (dX/dt) as a function of the degree of carrier reduction (X) for all carriers, where X is defined as: $X = (W_t - W_{red})/(W_{ox} - W_{red})$, with W_t denoting the momentary weight of the carrier, W_{ox} the carrier weight in the fully oxidized state, and W_{red} the carrier weight in the fully reduced state. Importantly, all values are calculated based on the complete reduction of the metal only, thus keeping a consistent reference for the differently doped carriers (which allow reduction of the support to different degrees). Thus, $X = 1$ represents the carrier in its fully oxidized state, while $X = 0$ indicates that the active metal in the oxygen carrier is fully reduced (without any contribution of the reducibility from support). Measurable contributions of the reducibility of the support beyond the full reduction of the metal phase hence result in $X < 0$ due to the additional decrease in the carrier weight.

Overall, all doped carriers show similar trends for the rate of carrier conversion: two zones of reduction with first maxima between $1 < X < \sim 0.9$ and the second extended maxima between $0.9 < X < 0$. The boundaries of the first reduction regime correspond well with the reduction of Fe_2O_3 ($X = 1$) to Fe_3O_4 ($X = 0.88$), indicating that the initial reduction of the fully oxidized iron oxide phase proceeds very rapidly. This is in clear contrast to the undoped carrier where the first peak is completely absent suggesting that the reduction is controlled by the availability of the solid-phase oxygen. Furthermore, the rate of reduction for the undoped carrier during the rest of the cycle is lower than that for all the doped carriers. Hence, addition of dopants improve the transfer of oxygen in the overall carrier and result in improved reduction rates.

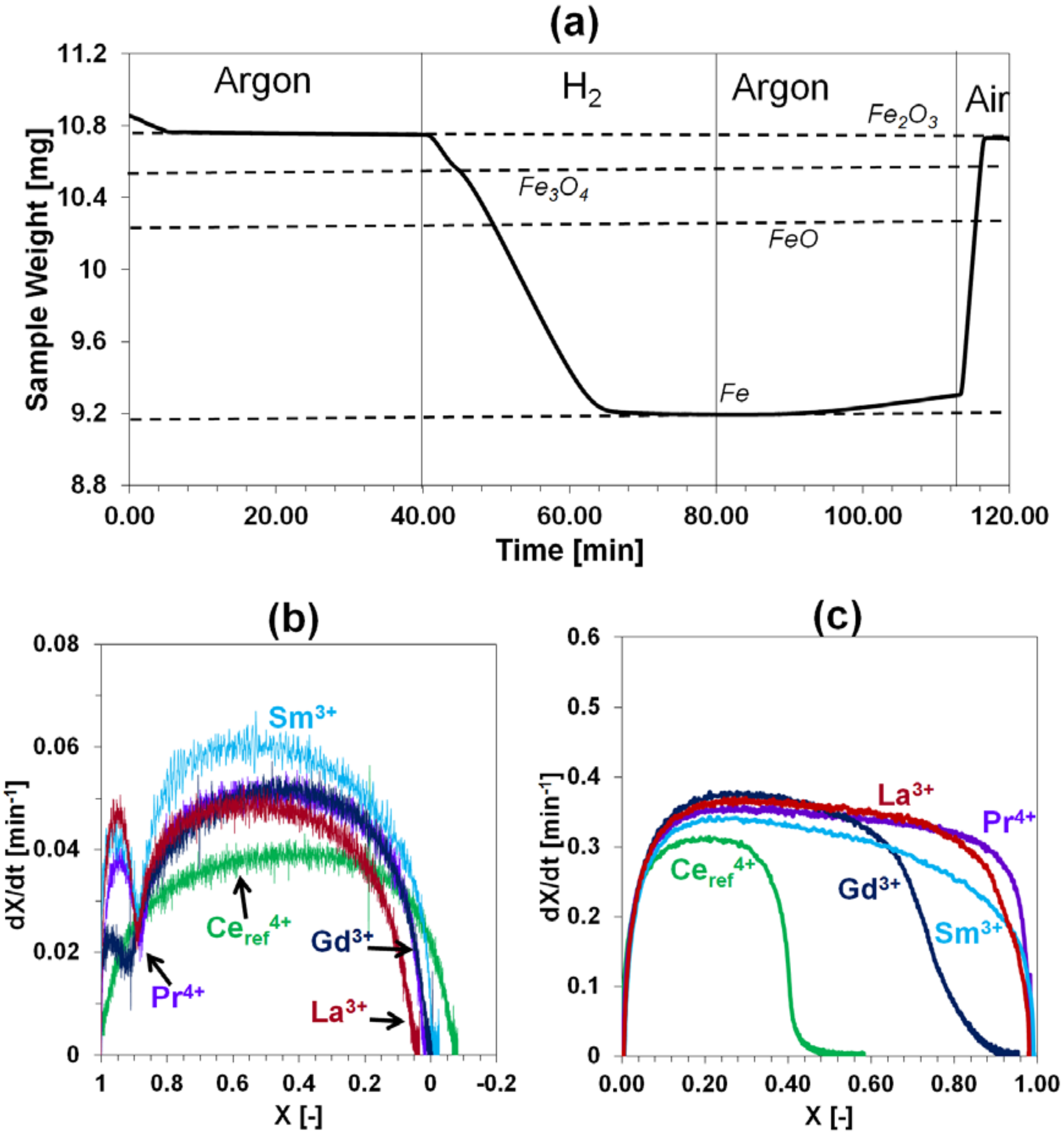

Figure 29. a) Single redox cycle during redox operation of Fe–$Pr_{0.1}Ce_{0.9}O_{1.95}$ in TGA at 450ºC with reduction in H_2, argon purge, and air oxidation (all 20 sccm). Dotted lines in the panel show the sample weight that corresponds to various oxidation states of the carrier during redox operation. Comparison of (absolute) rates of carrier conversion during b) reduction with H_2 and, c) oxidation with air, for the various iron loaded-doped supports at 450ºC

Figure 29c shows the absolute oxidation rate (dX/dt) as a function of the degree of carrier reduction (X) for all carriers, where X is defined as before. Thus, for the oxidation half cycle the difference between the doped carriers and the undoped CeO_2 was much more apparent. Fe-CeO_2 was only oxidized up to X = ~0.6 as compared to the other carriers which were completely oxidized (X ~ 1). The rate of oxidation for all the doped carriers remained constant (dX/dt ~ 0.35) over the entire oxidation half cycle suggesting that oxidation (unlike reduction), does not proceed in a staggered manner. Typically, oxidation proceeds by reaction of gas phase oxygen with the metal atoms on the surface, thus forming an oxide film. Hence, the oxidation of the encapsulated metal requires diffusion of gas phase oxygen through the oxide film– the rate controlling step. Correspondingly, the oxidation of the undoped carrier proceeds rapidly upto X ~ 0.35 and then suddenly shuts down, possibly once an oxide layer of sufficient thickness is formed over all the particles. The addition of dopants results in formation of vacancies in the ceria lattice, thus enabling complete and efficient oxidation via “shuttling” of oxygen.

We further compare the effects of the dopant size in terms of their relative enhancements during reduction and oxidation. Figure 30 shows the time required for reduction of carrier up to X = 0.1 i.e. 90% reduction, and the time required for oxidation of carrier up to X = 0.9 i.e. 90% oxidation, plotted against the dopant size. We expect the doped carrier with the dopant size closest to cerium, would result in a relatively relaxed lattice and thereby the maximum reactive enhancement. However, on comparing the time required for reduction or oxidation, no clear trend can be seen with respect to the dopant ion size. Hence, this suggest that as long as the vacancies are created, the size of the dopant (or its chemical nature) does not have any appreciable impact on the reactive enhancements. Overall, these results indicate that the enhancements observed under these conditions are mainly due to the physical shuttling of oxygen and not due to any electronic effects.

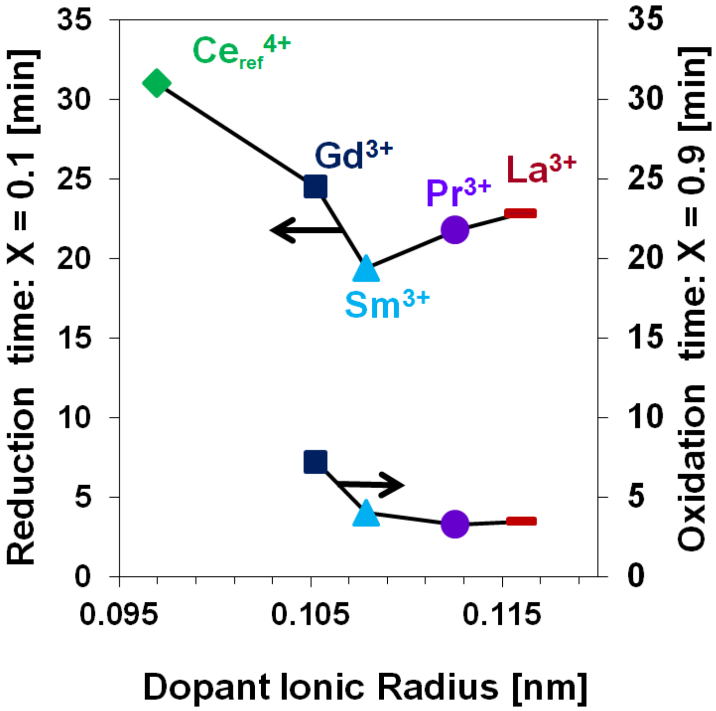

Figure 30. Comparison of time required for reduction (H_2, 20 sccm, 450°C) and oxidation (Air, 20 sccm, 450°C) in TGA for various doped carriers Fe-$D_xCe_{1-x}O_{2-x/2}$ (where D is the dopant, x = 0.1).

4.3.3 Reactive tests in fixed bed reactor

Although redox cycles in TGA provide useful information about carrier reactivity, they do not adequately represent gas– solid contacting patterns in a fixed bed or fluidized bed configuration. Hence, redox cycles in TGA cannot give meaningful insight into fuel conversion and product selectivity in the gas phase. In order to study the impact of dopant addition on the reactive parameters, we subject the carriers to reduction in methane. Moreover, since there was no appreciable difference in the reactivities of the various dopants, and going by the initial idea about reducing the lattice strain, we down-selected Pr as the dopant for the subsequent studies.

During fixed-bed reactor tests, the oxygen carrier bed was brought to the reaction temperature (900^{o}C) and then methane was flown over the pre-oxidized carriers until the carrier was reduced, i.e., until the selectivity for partial oxidation products (CO) starts dropping, indicating the depletion of solid phase oxygen.

Figure 31 compares the product selectivity as a function of the degree of carrier reduction for the undoped carrier (Fe-CeO_2) as well as the Pr-doped carrier (Fe-$Pr_{0.1}Ce_{0.9}O_{1.95}$). Fe-CeO_2 (Figure 31a) produces the mainly the total oxidation product CO_2 as the carrier reduces from Fe_2O_3 (carrier reduction = 0%) to Fe_3O_4 (carrier reduction = ~11%). This is reported widely in the literature and occurs due to the high rate of oxygen transfer during the transformation of Fe_2O_3 to Fe_3O_4. Subsequently, the product selectivity shifts to the partial oxidation product (CO) due to the relatively slower rate of oxygen transfer during conversion of Fe_3O_4 to FeO (carrier reduction ~ 33%). The product selectivity towards partial oxidation remains nearly constant up to ~80% carrier reduction, after which methane cracking is initiated (represented by the solid carbon produced). As expected, reduction of Fe–CeO_2 stops in close vicinity of the calculated carrier weight for fully reduced metallic iron suggesting little to no contribution from the support material.

The reduction of the Fe-$Pr_{0.1}Ce_{0.9}O_{1.95}$ carrier looks qualitatively similar to Fe-CeO_2. However, it is interesting to note that the CO_2 selectivity remains high (>80%) for up to ~33% carrier reduction as compared to 11% for Fe-CeO_2. Overall, all the transitions in selectivities are shifted to higher degrees of carrier reduction emphasizing the improved oxygen transport. It is furthermore remarkable that the shift of the selectivity ‘‘breaks” toward lower carrier weight (i.e. higher oxygen consumption) is already present for the very first transition, i.e. the transition from Fe_2O_3 to Fe_3O_4. This indicates that the carrier support contributes oxygen to the methane combustion from the very onset of the reaction and not only after the oxygen in the Fe-phase has been depleted. This suggests that the oxygen exchange between the Fe-phase and the support proceeds in a very facile way and agrees with earlier observations that doping results in the formation of oxygen vacancies which greatly facilitate oxygen transport inside the (doped) ceria lattice[81,90,100].

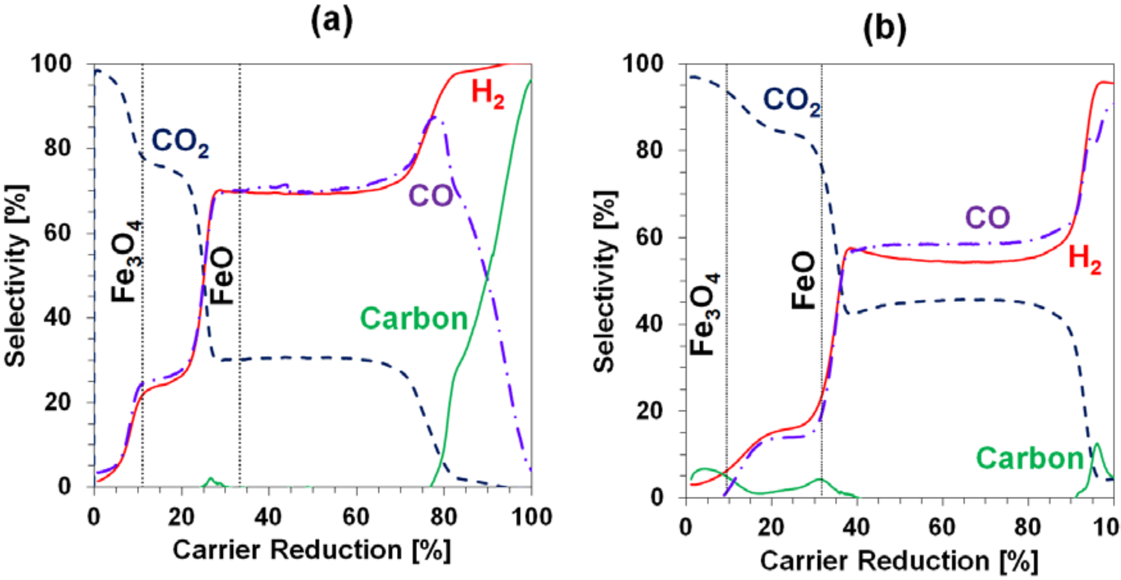

Figure 31. Comparison of product selectivity for a) Fe-CeO_2 and b) Fe-$Pr_{0.1}Ce_{0.9}O_{1.95}$ as a function of carrier reduction in a fixed bed reactor (100mg, 900ºC) during the reduction half cycle (CH_4, 1 sccm, 16.7 vol%).

4.3.4 Effect of doping on stability

Finally, it can be expected that doping of the support may affect – beyond the reactivity – also the carrier stability during redox cycling. It has been previously reported that doping ceria helps abate the deterioration of its textural properties which in turn helps preserve the oxygen defects in the support structure[83,89,107]. Therefore, multi-cycle TGA redox tests were used to investigate the effect of doping on the redox stability of the carriers at CLC conditions.

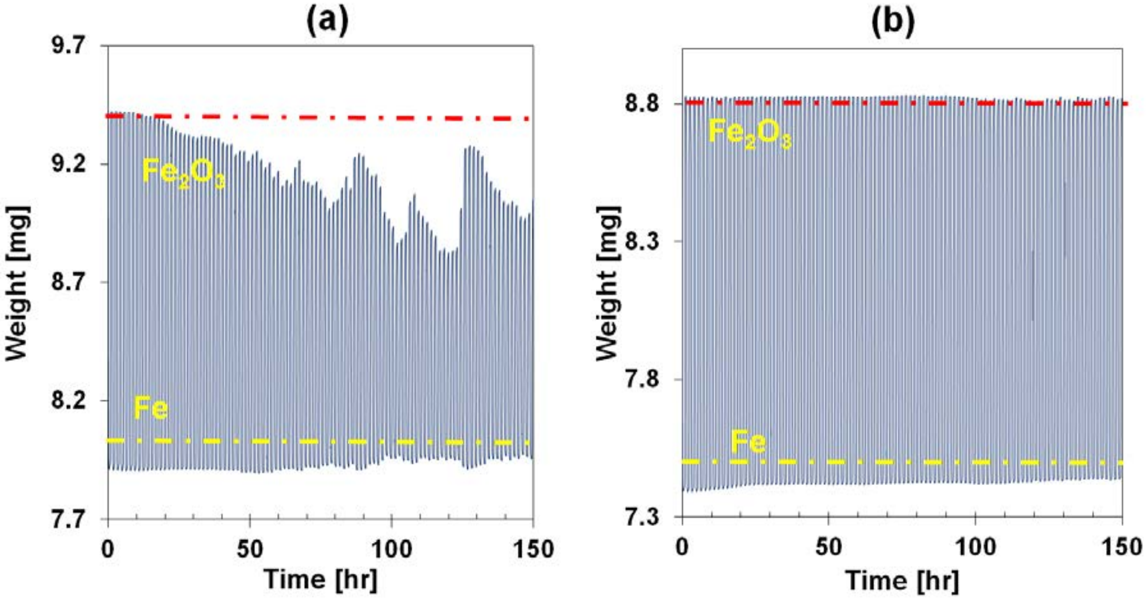

Figure 32. Comparison of 100 redox cycles for a) Fe-CeO_2 and b) Fe-$Pr_{0.1}Ce_{0.9}O_{1.95}$ at 900°C in TGA using H_2 and air.

Figure 32 compares performance of Fe–$Pr_{0.1}Ce_{0.9}O_{1.95}$ and undoped Fe–CeO_2 over 100 cycles using H_2 as model fuel at 900°C. The Pr-doped carrier shows stable operation, characterized by reproducible carrier weights in successive reduced and oxidized states, and is fully reduced and oxidized during the redox process (as indicated by the dotted lines representing the sample weights in various oxidation state of the metal). The carrier weight dips below the completely reduced carrier weight due to the reducible nature of the support.

In contrast to that, while Fe–CeO2 appears to be stable over the initial ~15 cycles, this carrier subsequently shows strong deactivation with incomplete re-oxidation of the carrier. This inability to re-oxidize completely suggests sintering/agglomeration, where the increasing particle size results in increasingly long pathways for solid state diffusion in order to access the oxygen contained in the carrier. The absence of a significant change in the redox kinetics over 100 cycles for the Pr-doped carrier suggests that Pr-doping helps to maintain a high oxygen mobility in the support structure and hence keeps the iron oxide phases easily accessible. Hence, overall the doped support materials will be of particular interest for large scale applications where identification of robust carriers is a key concern.

4.4 CONCLUSIONS

The identification of low-cost, highly active and stable oxygen carrier materials is critical for successful implementation of chemical looping technology in industrial practice. To-date, most studies have focused on monometallic carriers supported on simple oxides. In the present report we investigated the impact of various dopants on the redox kinetics of the supported active metal. Moreover, based on similar studies in the electrochemical literature, we hypothesized that dopant properties (ionic size and chemical nature) will influence the relative kinetic effects due to a combination of physical (lattice strain) as well as electronic effects.

Doped ceria supports ($D_xCe_{1-x}O_{2-x/2}$ where D = Pr, Gd, Sm or La) were synthesized using a straightforward hydrothermal synthesis approach and Fe was deposited onto the support matrix via deposition–precipitation. X-ray diffraction and lattice parameter calculations confirm the formation of a uniform solid solution of dopant in ceria, i.e. complete incorporation of dopants into the ceria cubic lattice. Upon deposition of iron onto the doped ceria supports, all the carriers showed good thermal stability. During redox cycling, all doped carriers showed strongly enhanced kinetics as compared to the undoped carrier, during the reduction as well as oxidation half-cycles. The enhancement during the oxidation half cycle was much more prominent as the undoped carrier was incompletely oxidized (~60%) at lower temperature (450^oC), whereas all the doped carriers were completely oxidized. This observation suggests that the vacancies created on addition of dopants, result in modification of the oxygen transport mechanism and thus enable efficient oxidation of iron oxide. However, amongst the various doped carriers, the relative redox kinetics followed no specific trend with respect to the dopant size or chemical nature, suggesting that the kinetic improvements were purely an effect of vacancy creation and the subsequent shuttling of oxygen. Hence, a single doped carrier (Pr-doped CeO_2) was down-selected for evaluation of gas-phase reactivity and long-term thermal stability. The gas-phase product selectivity during reduction with CH_4 for both the Pr-doped and the undoped carrier were qualitatively similar with a mixture of total and partial oxidation products being generated. The transitions in product selectivity for the Pr-doped carrier were shifted to higher degrees of carrier reduction as compared to the undoped carrier. Over the course of the complete carrier reduction, for the doped carrier, the improved oxygen transport results in results in production of larger quantities of the total oxidation product (CO_2) as compared to the partial oxidation products (CO).

Finally, from an applied perspective the current results suggest that doped carrier supports, which have to-date not found much attention in industrial research on chemical looping, offer a range of benefits in return for minimal added carrier cost (due to low dopant concentrations and straightforward synthesis of these carriers). At the same time, enhanced stability will allow utilization of the carrier over more cycles and hence reduction in carrier cost due to carrier replacement.

5.0 PRODUCTION OF INHERENTLY SEPARATED SYNGAS STREAMS VIA CHEMICAL LOOPING

The content of this chapter is taken from More et. al., Production of Inherently Separated Syngas Streams via Chemical Looping, in preparation.

5.1 INTRODUCTION

While syngas produced in both the chemical looping dry reforming (CLDR) processes (described earlier) is of the optimum ratio (H_2:CO ~2) for direct utilization in Fischer-Tropsch synthesis, it is further desired to make this ratio tailorable to support other downstream processes such as methanol synthesis (H_2:CO ~1), ammonia production (H_2 only), carbonylation (CO only) and so on. Hence, we propose a modification of the chemical looping process as shown in Figure 33. CH_4 can be converted to a pure hydrogen stream and solid carbon via thermo-catalytic cracking over a metal catalyst in a "cracker" reactor. The deposited carbon is selectively oxidized in an oxidizer using CO_2, thereby producing pure CO streams and regenerated metal can be recycled back to the cracker. The metal thus periodically cycled between the two reactors carrying carbon from one to another. Not only does this process produce separate streams of H_2 and CO (that can be combined in tailorable H_2:CO ratios), but the process allows for CO_2 activation by conversion to CO.

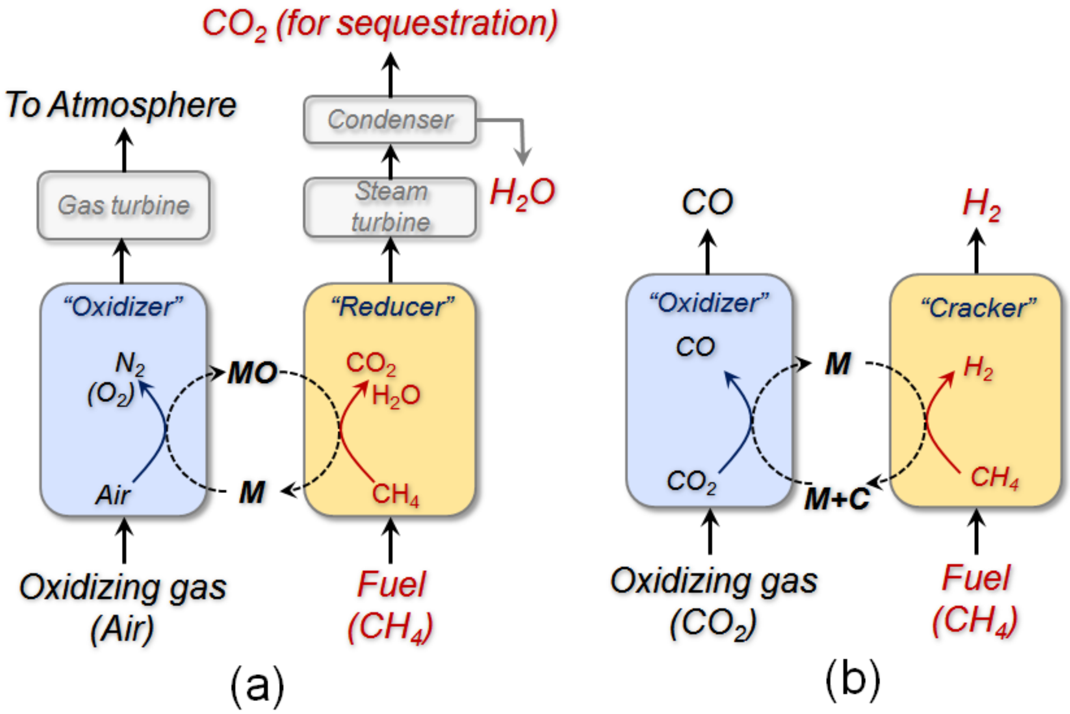

Figure 33. Chemical looping processes: a) chemical looping combustion and, b) proposed process for inherently separated syngas streams

Thermocatalytic cracking of methane for hydrogen production has been studied extensively over the past several decades, typically using transition metal based catalysts[108-112]. Due to the excellent C-H bond cleavage activity of Ni, supported Ni catalysts have widely been reported as the most favorable for this reaction. Typically, Ni dispersed on inert supports such as Al_2O_3, $MgAl_2O_4$ and SiO_2 have been investigated[113-116]. During the process of methane cracking, extensive carbon filament formation and concomitant H_2 production occurs, which avoids rapid deactivation of the catalyst and hence allows extended operation [74,77,117,118]. Eventually, however, the metal particles are encapsulated by carbon which results in deactivation. This deactivation is highly sensitive to the reaction temperature, with higher temperatures resulting in much faster deactivation. Hence, most cracking studies have focused on the temperature range between T= ~550-700°C to ensure sustained carbon (& hydrogen) formation[115,119-124]. However, in this temperature range methane conversion is typically ~50%, which is too low for economic implementation of this process since it results in a large separation requirement. Non–transition metal based catalysts such as carbon black have also been studied as a cheaper alternative, however the CH_4 conversions (5-30%) are even lower that for metal catalysts [125-129]. Irrespective of temperature, all the catalysts undergo eventual deactivation and require regeneration. Air regeneration (at ~600°C) has most commonly been reported an effective means to regenerate the catalysts[130-132]. In air regeneration, oxygen reacts with the deposited carbon to produce a mixture of carbon oxides (CO and CO_2), depending of the amount of excess air used. This process again results in CO/CO_2 emissions since the products cannot be separated easily from the N_2 in the air. Hence, a few studies used CO_2 as an oxidant. Takenaka et al. studied methane cracking over various nickel catalysts at 550°C and subsequent regeneration of the catalyst using CO_2 at elevated temperatures 650°C[133]. They reported incomplete removal of carbon possibly due to the weak oxidation capability of CO_2. Li and Smith also used CO_2 for regeneration of an alumina supported Ni catalyst, and reported extremely slow kinetics; at T~ 500°C oxidation with CO_2 was 20-times slower than with O_2/air[134]. Pinilla et al. used CO_2 to regenerate an activated carbon catalyst at high temperatures, but reported simultaneous burn-off of the catalyst[135]. Overall, while there have been some reports for cyclic operation of methane cracking processes, all of the reported processes suffer from low CH_4 conversion during catalytic cracking and large periodic temperature excursions during carbon burn-off in the oxidation half cycle.

The use of “active” supports is well established in heterogeneous catalysis, where in particular CeO_2 is in widespread use as a support for metal nanoparticles in oxidation and redox catalysis[136], such as automotive exhaust abatement[137], water gas shift[81,82] and catalytic methane oxidation[85]. Moreover, the strong metal support interactions for CeO_2 are known to help maintain smaller particle sizes, which are critical for most catalytic reactions[138]. However, few studies to-date have used CeO_2 as a support for the thermocatalytic cracking of methane. Li et al. investigated Ni-CeO_2 systems prepared by various methods and reported that interactions between Ni and CeO2 are critical for carbon formation[139]. Zapata et. al. reported that addition of CeO_2 to Ni-SiO_2 catalysts prevents the sintering of nickel particles during reduction process, thus improving the performance for catalytic cracking[140]. Finally, Ahmed et al. used Ni supported on ceria-modified alumina supports and reported improved carbon formation, again citing improved metal dispersion[141]. The above reasoning and the few encouraging reports, in combination with our own experience using ceria as a highly active support in chemical looping processes[42,46,57,100,142], motivate the investigation of CeO_2 as a potential support for the proposed process.

In the present report, we hence demonstrate the design of a chemical looping methane cracking process for the production of inherently separated syngas streams using a Ni-ceria “carbon carrier”. We demonstrate the impact of Ni weight loading on the reactive performance as well as the carbon morphology formed. Furthermore, we demonstrate simple control of Ni particle size by changing the size of the support for improving the catalytic performance. Finally, we investigate the impact of temperature on carbon production (and hence methane conversion) for Ni supported on CeO_2 vs $MgAl_2O_4$ as a reference for an “inert” support. Based on this, we identify and demonstrate conditions for operation of chemical looping methane cracking (carbon deposition and burn-off) in a periodically operated fixed bed reactor.

5.2 EXPERIMENTAL SECTION

5.2.1 Material synthesis:

CeO_2 and $MgAl_2O_4$ supports were synthesized from the corresponding salt precursors by dissolving in ethanol and vacuum drying overnight (100^oC). The resulting solid cake was ground using a mortar-pestle and then calcined in air (200 sccm) at 900^oC for 2hr. Additionally, commercially available CeO_2 powders (99+%, Alfa Aesar) were also used. The carriers were synthesized by a cheap and simple wet-impregnation approach. Briefly, appropriate quantities of the metal nitrate precursor ($Ni(NO_3)_2{\cdot}6H_2O$, 99+%, Sigma Aldrich) was dissolved in 1mL ethanol. The CeO_2 powder was then added to the solution, stirred continuously for 2 hours and vacuum dried overnight (100^oC). The resulting solid cake was ground using a mortar-pestle and then calcined in air (200 sccm) at 900^oC for 2hr. The carriers were synthesized with weight loading of 20%, 40%, 60% and 90%.

5.2.2 Material characterization:

X-Ray Diffraction Characterization. To confirm the phases present, the synthesized carriers were analyzed by a powder X-Ray diffractometer (Bruker D8) operating at 40kV and

40mA with Cu Kα radiation (λ=1.5418 Å). The data was recorded between 2Θ values of 20° and 90° with a scanning rate of 3.5 K/min. The phases were identified using the JCPDS database and the average crystallite size was determined by the Scherrer equation.

Surface area. BET (Brunauer-Emmett-Teller) surface area determination was conducted via Nitrogen adsorption/desorption in a Micrometrics ASAP 2020 gas adsorption analyzer at -196°C. The samples were pretreated by degassing under vacuum for 2hr at 130°C.

Electron Microscopy. A Transmission Electron Microscope (TEM) JEOL-200CX was used to image the particles. Bulk metal weight percentages and metal dispersion of the synthesized samples were analyzed by Energy Dispersive X-Ray Analysis (EDAX) performed using an Oxford INCA EDS system attached to a JSM-6510LV SEM.

5.2.3 Reactive testing

Solid-Phase Reactivity. Carrier reactivity was determined by a Thermo-Gravimetric Analyzer (SDT Q600, TA Instruments). Alumina pans containing 7-10mg of sample powders were loaded into the instrument. The temperature was ramped up to the reaction temperature at 100 °C/min and then held isothermally for the experiment duration. The gases used were: N_2 (Grade 5.0, 100sccm), Ar (Grade 5.0, 20sccm), H_2 (Grade 2.0, 20sccm) CH_4 (Grade 2.0, 5sccm) and CO_2 (Grade 2.0, 20sccm). The carrier gas (N_2) is flown continuously throughout the experiment. The reactive gases H_2/CH_4 and CO_2, are used for the reduction and oxidation of the carrier respectively, and the purge gas (Ar) is used to flush the system between consecutive reduction and oxidation cycles. For comparison between the various carriers, normalized weight of carbon (mg C/mg Ni) deposited, and the normalized rate (mg C/mg Ni-min) were calculated as follows:

$$Normalized\ Carbon = \frac{Sample\ Weight - Reduced\ Weight}{Oxidized\ Weight - Reduced\ Weight} \quad \text{Eq. (26)}$$

$$Normalized\ Rate = \frac{(Normalized\ Carbon)_{t_1} - (Normalized\ Carbon)_{t_2}}{t_1 - t_2} \quad \text{Eq. (27)}$$

The oxidation states of the samples were calculated from the sample weight by a simple mass balance relative to the fully oxidized sample weights.

Gas-Phase Reactivity. Conversion of the fuel (CH_4) and product selectivity were determined in a fixed bed reactor set-up. 20mg or 100mg of sample was packed between two glass wool plugs in a horizontal quartz tube (6.35mm ID) enclosed by a furnace (Thermo electron corporation-Lindberg/Blue M). The bed temperature was measured by a coke resistant, high-temperature therm^{oc}ouple (Omega Engineering). The gases used were: He (5sccm and 40sccm), CH_4 (Grade 2, 1 sccm) CO_2 (Grade 5.0, 1 sccm) and O_2 (Grade 5, 1 sccm). Outlet gas concentrations were measured by a mass spectrometer (Pfeiffer Omnistar QMS 200), and the corresponding molar flow rates (n_i) were calculated from the (calibrated) ion currents. The accuracy of the measurement was checked by performing carbon balances over the system and closed to within 10-12%.

The major reactions in the system during the reduction half cycle are total oxidation, partial oxidation and catalytic pyrolysis of CH_4:

Total Oxidation: $CH_4 + 4\ MeO \Leftrightarrow 4\ Me + CO_2 + 2\ H_2O$ (R11)

Partial Oxidation: $CH_4 + MeO \Leftrightarrow Me + CO + 2\ H_2$ (R12)

Methane Pyrolysis: $CH_4\ (+\ Me) \Leftrightarrow 2\ H_2 + C\ (+\ Me)$ (R13)

Hence, the carbon balance for the reduction half cycle was calculated as:

$$n_{CH_{4,in}} = n_{CH_{4,out}} + n_{CO_{2,out}} + n_{CO_{out}} + 0.5 \times (n_{H_{2,out}} - 2n_{CO_{out}})$$

Eq. (28)

The conversion and selectivity of the various gaseous products involved were calculated using the following formulae:

$$X_{CH_4} = \frac{n_{CH_{4,in}} - n_{CH_{4,out}}}{n_{CH_{4,in}}} \qquad S_{H_2} = \frac{n_{H_{2,out}}}{n_{CH_{4,in}} - n_{CH_{4,out}}}$$

Eq. (29), (30)

$$S_{CO} = \frac{n_{CO_{out}}}{n_{CH_{4,in}} - n_{CH_{4,out}}} \qquad S_{CO_2} = \frac{n_{CO_{2,out}}}{n_{CH_{4,in}} - n_{CH_{4,out}}}$$

Eq. (31), (32)

The major reactions in the system during the oxidation half cycle (with O_2) are:

Carbon partial oxidation: Me+ C + ½ O_2 = Me + CO (R14)

Carbon total oxidation: Me + C + O_2 = Me + CO_2 (R15)

Hence, the oxygen balance for the oxidation half cycle with O_2 was calculated as:

$$2 \times n_{O_{2,in}} = 2 \times n_{CO_{2,out}} + n_{CO_{out}}$$

Eq. (33)

And during oxidation cycle with CO_2 are:

Carbon oxidation: Me + C + CO_2 = Me + 2CO (R16)

Hence, the oxygen balance for the oxidation half cycle with CO_2 was calculated as:

$$2 \times n_{CO_{2,in}} = 2 \times n_{CO_{2,out}} + 0.5 \times n_{CO_{out}}$$

Eq. (34)

5.3 RESULTS AND DISCUSSION

5.3.1 Carrier reactivity with CH_4: Effect of Ni weight loading

The reactivity of the oxygen carriers with CH_4 was initially studied in a thermo-gravimetric analyzer (TGA) at 800°C. The weight change upon reacting the carriers with CH_4 was recorded and the amount of carbon (normalized to the amount of Ni in the carrier) was calculated and used to compare all carriers. Since Ni in the as-synthesized carriers is in the oxidized state, all carriers were reduced in a H_2 at 800°C in-situ before the start of the experiment.

As a first parameter, the impact of Ni loading was investigated, since chemical looping processes typically at much higher metal weight loadings than conventional catalytic processes. Figure 34a shows the mass of carbon deposited versus time during exposure of the Ni carriers (with varying Ni wt%) to CH_4 . The mass of carbon produced is normalized to the mass of Ni in the respective sample (as discussed in the methods section). Since Ni is the active component in the carriers, one might expect that the carbon produced per mass of Ni would remain constant as the Ni weight loading is increased. However, it can clearly be seen that the amount of carbon produced decreases with increasing Ni weight loading. Thus the sample with 20wt% Ni produces the most carbon (~0.8 mg C/ mg Ni over 60min) with higher Ni weight loading producing progressively lesser amounts of carbon. Figure 34b shows the rate of carbon deposition (again normalized to the Ni content) for these carriers. The rate of carbon formation for the 20wt% Ni sample is ~4 times higher than that for the 40wt% Ni and ~7 times than 60wt% Ni. Similar effects were reported for Ni-supported on SiO_2 catalysts by Venugopal et al[143]. Overall, the significantly higher amounts of carbon formed for the sample with the lowest weight loading strongly suggests that the active Ni particles in the different samples differ in their size or morphology (and hence their surface reactivity).

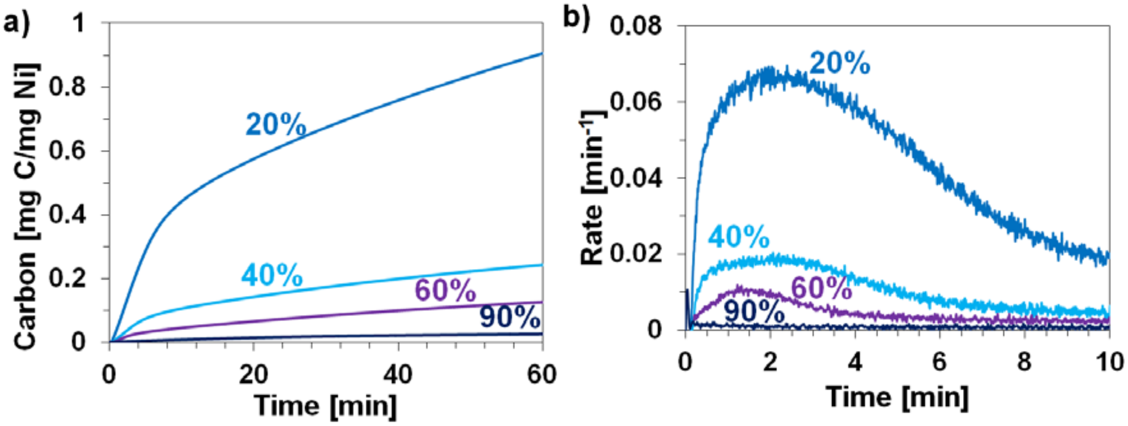

Figure 34. Comparison of the reactivity of various carriers with CH_4 in TGA at 800ºC. a) Comparison of the amount of carbon produced (mg C/mg Ni) show a decrease in amount of carbon produced with increasing Ni weight loadings and, b) comparison of rates of normalized carbon formation (mg C/mg Ni-min) shows that increased carbon formation is directly related to the rate of carbon formation**.**

To investigate the structural differences in the Ni particles present in the various samples, the "coked" samples after the TGA experiments were investigated under the TEM. Figure 35 shows representative TEM images of two such samples: a) & b) for 20wt% Ni, b) & d) for 60wt% Ni (with Ni particles showing up darker compared to carbon due to the differences in Z number). One can see that, as expected, the Ni particles for the higher Ni weight loading are larger than those for the lower weight loading. However, the size difference (and hence the increased surface area) alone do not account for the strong difference in carbon formation. Instead, the carbon formed on the two carriers is morphologically different. For the 20wt% Ni **(**Figure 35a and b**)**, carbon filaments are observed with Ni particles encapsulated within. These filaments are responsible for the large amount of carbon per Ni (on weight basis) that was observed during the course of the TGA experiments, since the carbon formation is hence not limited by the amount of Ni or the Ni surface area available. On the other hand, for 60wt% Ni carrier, carbon filaments are conspicuously absent. Instead, the Ni particles are directly encapsulated by a carbon film formed on the particle surface. Correspondingly, the amounts of carbon formed is limited by the available Ni surface area and hence much lower than for the 20wt% sample.

The TEM images show that the size of the Ni particles that result in carbon filament formation (i.e. for the 20 wt% Ni) and those that result in carbon film encapsulation (for the 60 wt% Ni) are very different. Virtually all Ni particles found in the carbon filaments are in the sub-50nm range, while those encapsulated by carbon films are >100nm. This suggests that the Ni particle size is critical in enabling carbon nanofiber growth and hence facilitating carbon production. The generally accepted mechanism for carbon filament formation involves activation of methane on Ni particles to form solid carbon and gaseous H_2[74,77,144,145]. The carbon diffuses through or over the Ni particle and precipitates on the support side thereby causing a particle lift-off. This process continues after lift-off of the particle, resulting in formation of carbon nanofibers. Small imbalances in carbon formation and carbon transport eventually result in carbon built-up and deactivation of the Ni particles. The carbon transport through or over the Ni particle is hence critical to filament formation and has been shown to be the rate limiting step of the process[74,146]. Consequently, it is expected that the carbon transport through or over larger Ni particles is much slower athn for smaller Ni particles, and hence results in much more rapid deactivation, and ultimately in formation of only carbon films. Similar effects have be reported for other Ni-based catalytic cracking systems. For example, Toesbes et al. show a dependence of carbon morphology on Ni particle size for CH_4 and C_2H_2 for Ni-SiO_2 [147]. Li et al. synthesized Ni particles with controlled size and demonstrated that Ni particles >>100 nm do not produce carbon[148]. Chen et al. used a series of hydrotalcite supported Ni catalysts and suggest that an optimum growth rate and yield of carbon nanofibers can be achieved for optimally sized Ni particles (~ 34 nm) [149]. Similarly, for our carriers, higher weight loadings of Ni resulted in formation of larger particles, likely due to ease in aggregation during high temperature operation, and hence caused strongly reduced carbon formation.

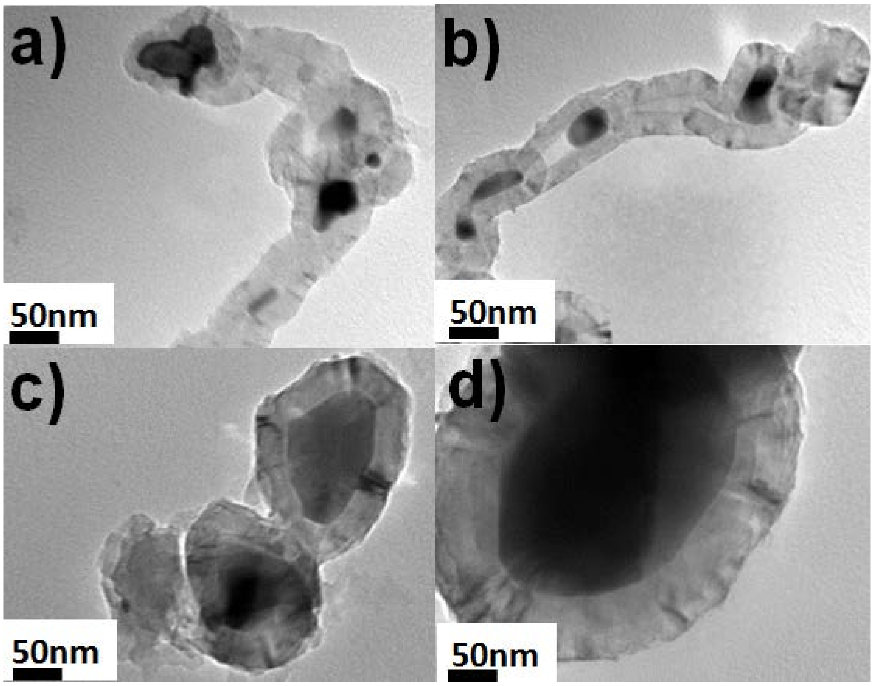

Figure 35. TEM images of carriers post CH_4 cracking in the TGA at 800ºC for: 60wt% Ni (a & b) and, 20wt% Ni (c & d). This shows a difference in carbon morphology (filament vs. encapsulation) depending on the Ni particle size.

5.3.2 Carrier reactivity with CH_4: Effect of CeO_2 size

If Ni particle size is directly dependent on the amount of Ni in the sample due to aggregation effects, as hypothesized above, the CeO_2 support should be expected to play an important role in controlling particle size by affecting dispersion via the available surface area. The ceria support used for the above discussed set of experiments was 52nm (as measured in XRD). To investigate the effect of CeO_2 particle size, two smaller ceria particle sizes (25nm and 35nm, respectively) of commercially available CeO_2 were used as supports. For comparison all carriers were loaded with the same 20 wt% Ni loading.

The as-synthesized carriers were reduced in H_2 to reduce the NiO to metallic Ni and analyzed in XRD to determine particle sizes of Ni and CeO_2. Figure 36 compares the Ni particle sizes (red crosses) as a function of the ceria support particle size. As expected, the sample with the smallest CeO_2 particles (~25nm) yields the smallest Ni particles (~27nm), and Ni particle size increases systematically with CeO_2 particle size. This hence agrees well with the hypothesis that increasing surface area of the support (which increases inversely proportional to the square of size, assuming a spherical geometry) results in improved Ni dispersion, i.e. smaller Ni particle size. In fact, the specific surface areas of the ceria supports were determined via nitrogen sorption and found to increase by a factor of 3 across the range of CeO_2 particle sizes, i.e. from ~10 m^2/g (52nm CeO_2) to ~ 35 m^2/g (25nm CeO_2), in good agreement with the calculated values of 15 m^2/g and 32 m^2/g (based on the assumption of spherical particles and the density of bulk ceria). Hence, for smaller CeO_2 particles, there is a significantly higher surface area available for Ni particle dispersion and thereby a reduced probability of Ni particle agglomeration.

Clearly, a reduced Ni particle size should manifest itself in much improved reactive performance. Hence, all the samples were subjected to the same TGA experiment as before: in-situ reduction in H_2 followed by CH_4 cracking at 800^{o}C. Figure 36a shows the mass of carbon deposited at the end of 5min, 10min, 15min and 20min for each carrier (blue diamonds, from bottom to top). On reducing the CeO_2 particle size from 52nm to 35nm, the (average) Ni particle size changes only marginally from 50nm to 43nm and the amount of carbon produced hence also increases marginally over the same time duration. However on further reducing the CeO_2 particle size to 25nm, the Ni particle size reduces much more significantly to 27nm and the corresponding amount of carbon produced increases strongly (by a factor of 2-3). Figure 36b shows photos of this sample before and after the experiment. The sample (~7mg) sits at the bottom of the white pan at the start of the experiment and is hence initially not visible. After the reaction, the carbon formed can be seen overflowing from the pan, visually confirming the strongly enhanced reactivity. Moreover, analyzing this sample under TEM (Figure 36b, bottom) shows carbon filaments, characteristic for strong carbon formation. Overall, these observations not only further confirm that Ni particle size directly influences carbon formation, but also indicates that the Ni particle size can be easily tailored by controlling the particle size of the CeO_2 support.

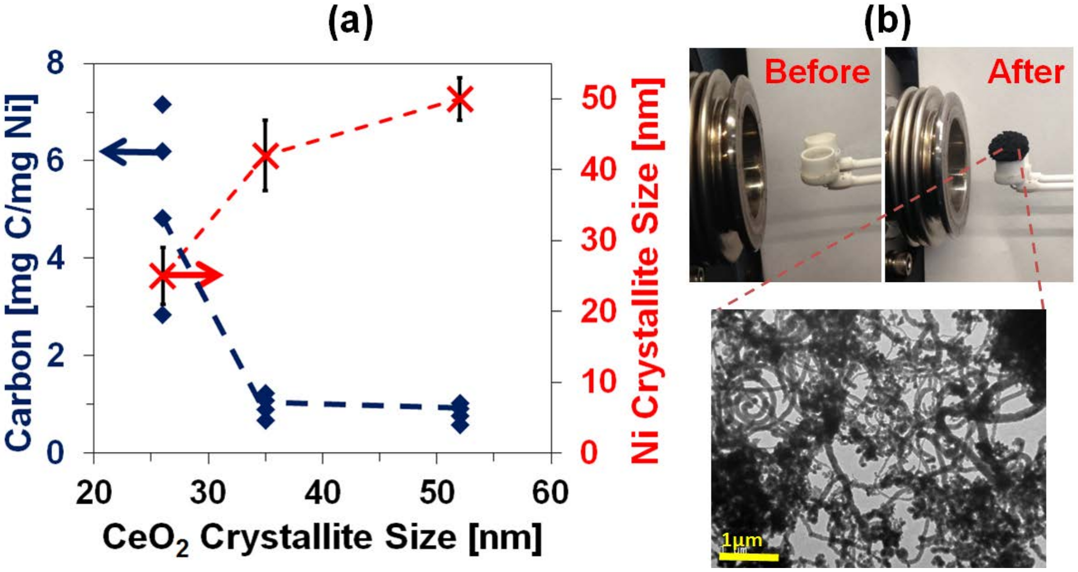

Figure 36. a) Comparison of carbon (mg C/mg Ni) deposited on Ni-CeO_2 samples (all 20wt% Ni) of different CeO_2 particle sizes in TGA (CH_4 at 800ºC). The blue diamonds represent the carbon produced at 5, 10, 15 and 20 min after the start of reduction. The red crosses indicate the average Ni particle size for each sample calculated using the Scherrer equation with the corresponding standard deviations. The CeO_2 particle size influences the Ni particle size and hence, is inversely related to the amount of carbon produced. b) Ni-CeO_2 sample (CeO_2 size 25nm), before and after flowing CH_4 in the TGA showing the amount and nature (TEM below) of carbon formed.

5.3.3 Evaluation of gas phase reactivity in a fixed bed reactor

Although the TGA tests yield important insights into the reactivity of the carrier materials, the flow configuration (and hence the gas−solid contacting pattern) in a TGA is not representative of that in a fixed-bed or fluidized bed reactor nor does it allow for studies of the selectivity of the reaction. Hence, as a next step, the reactivity of the carriers was tested in a fixed bed reactor at conditions otherwise similar those employed in the TGA..

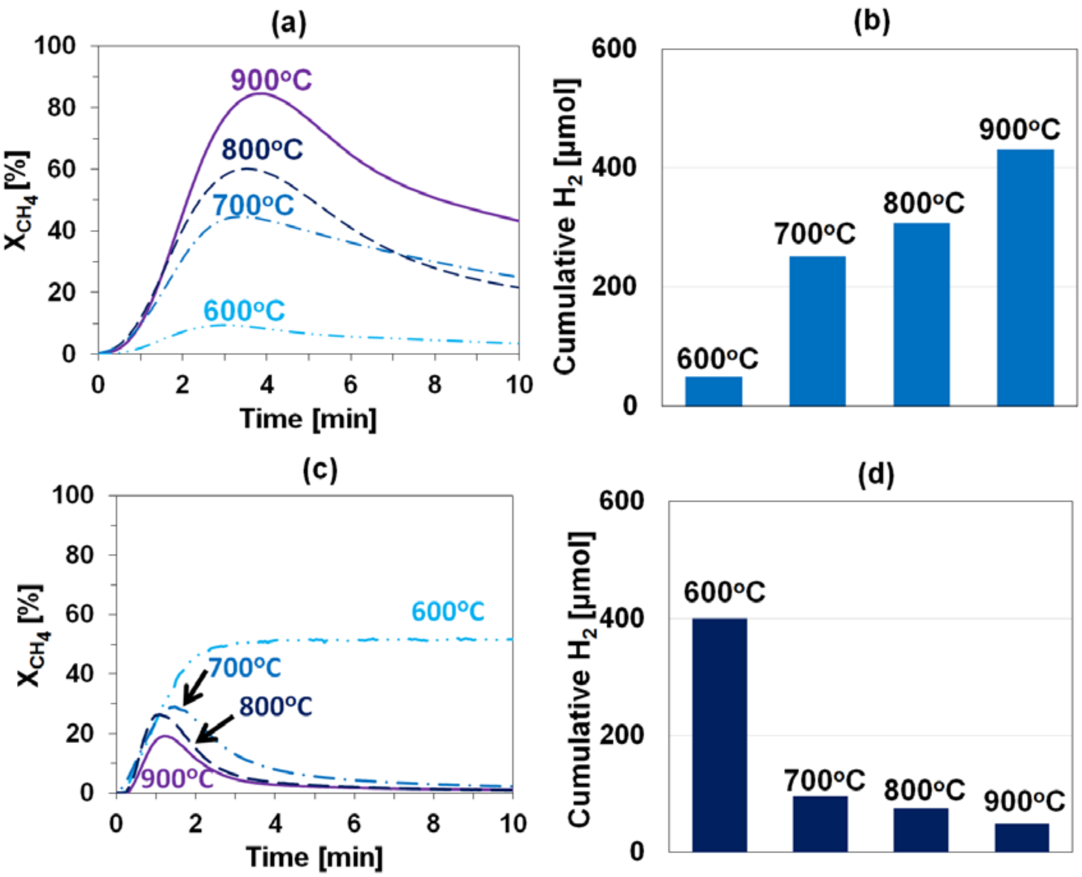

Figure 37. Comparison for methane conversions (X_{CH4}) and cumulative H_2 (over 10min) produced tested in a fixed bed reactor at various temperatures under CH_4 flow (1sccm, 16.7vol%) for 20wt% Ni-CeO_2 (a) & (b), and 20wt% Ni-$MgAl_2O_4$ (c) & (d) both for 20mg sample in the bed. Unlike Ni-$MgAl_2O_4$, the methane conversion and hence H_2 produced increases with temperature for Ni-CeO_2.

For the first set of experiments, the 20wt% Ni supported on the CeO_2 (52nm) synthesized in the lab is used (so as to enable comparison with similar sized $MgAl_2O_4$ as discussed below). Similar to the TGA experiment protocol, all samples were reduced in-situ using H_2 at 900°C, followed by flowing CH_4 (1sccm, 16.7vol%) at the respective temperature. Each experiment was run until the methane conversion dropped to less than 50%. Figure 37a shows the conversion-time traces for the first 10 min of this carrier at temperatures between 600-900°C. At the lowest temperature, CH_4 conversion is very low with a maximum value of ~10%. With increasing the temperature in steps of 100°C, the CH_4 conversion increases dramatically reaching ~80% at 900°C. The cumulative H_2 produced over the 10 min duration of the methane cracking experiment at various temperatures, shown in Figure 37b confirms this trend with strong increases with temperature from 600°C to at 900°C.

Interestingly, these trends contrast strongly with those observed for a similar Ni carrier using a non-reducible support: Figure 37c & d show results from the same experiments using a 20wt% Ni carrier supported on $MgAl_2O_4$. Clearly, the opposite trend with temperature is observed: Methane conversion is highest at 600°C with ~50%. Notably, the cracking cycle continued for ~60min at that constant conversion before rapidly shutting down (not shown). However, increasing the temperature drastically *decreases* the methane conversion (to ~20% at 900°C). Similar observations have been reported previously[116,119,150,151] and are the primary reason why methane cracking has been carried out to-date preferably between ~550°C-650°C.

The reason for the rapid decrease in reactivity with increasing temperature for non-reducible supports has been suggested to be a rapid encapsulation of Ni particles at high temperatures due to the much higher rates of carbon deposition compared to the rate of carbon diffusion through (or over) the Ni particle. At this point, we do not have a firm explanation why such a deactivation does not occur for the Ni-CeO_2 system. However, it is tempting to speculate that a difference in metal-support interactions might be responsible for this interesting observation. It has been reported before that metal particles are bound strongly to CeO_2 due to strong metal support interactions (SMSI)[138,152-154]. However, carbon filament formation occurs via Ni particle elongation due to the favorable interfacial energy of carbon adsorption on Ni[74], i.e. the ease of this elongation can be expected to rely on a competition between the Ni-C and Ni-support interfacial energies. Moreover, it has also been shown that Ni facet re-alignment is critical to the growth of the filaments. Ni (110) is a highly active face for carbon formation while Ni (100) has much lower activity, and Ni (111) shows no activity at all[155]. Hence, the Ni (100) facet is oriented towards the filament growth, while the (111) facet forms in the tail part of the crystal. This (111) facet is the most favorable surface for the formation of graphite due to the coinciding symmetry between the parameters of Ni {111} plane and graphite {002} plane[156]. We hence hypothesize that at low temperatures the strong metal support interactions in the Ni-CeO_2 system do not allow the required changes in Ni particle morphology and hence impede carbon filament growth. However, higher temperatures provide thermal energy to overcome the SMSI for the particle realignment to occur and hence facilitate filamentous carbon production. Barrault et al. have shown that the metal support interaction for Ni supported on CeO_2 are much stronger than those for SiO_2 or Al_2O_3 supports[157]. For the Ni-$MgAl_2O_4$ system the metal-support interactions can be expected to be even weaker due to passivation of Al atoms by Mg addition. Hence, Ni on $MgAl_2O_4$ will tend to form carbon filaments much more easily at lower temperatures due to a combination of two factors: ease in Ni particle restructuring, and an optimum between carbon formation and transport rates. Increasing temperature facilitates Ni particle restructuring but the transport of carbon is not able to keep up with carbon formation, and the system hence shuts down rapidly.

In the CeO_2 system, the impeded restructuring of the Ni nanoparticles due to SMSI slows carbon formation at low temperatures, which is removed with increasing temperature. Why this impediment at lower temperature does not result in a rapid shut down of the reaction is not entirely clear yet (while one might speculate that the “active” ceria could help removal of carbon via oxidation, none of the experiments showed significant formation of CO_x at these conditions). However, our results suggest the morphological change occurring for the Ni particle at the moment of particle lift-off may be key to obtaining further mechanistic insights for this process.

5.3.4 Periodic operation in a fixed bed reactor: cracking and oxidation

Up to this point, the focus of the investigation was on identifying major controlling factors for the performance of the Ni-CeO_2 carriers in catalytic cracking of methane. As expected, the catalytic performance of the carriers deteriorates over time due to slow carbon built-up, resulting in reduced methane conversion/H_2 production. Hence, the carrier needs to be regenerated periodically by burning off the deposited carbon using an oxidizing gas. We hence proceeded to investigate the full periodic “chemical looping” process. For these investigations, 20wt% Ni supported on commercial CeO_2 (particle size=25 nm) was used due to the superior CH_4 cracking performance (see above).

First tests were performed with CH_4-O_2 cycles at 900^{o}C to demonstrate the validity of the process. Figure 38 shows the concentration traces during periodic operation in a fixed bed reactor. CH_4 (1 sccm, 16.7 vol%) and O_2 (1sccm, 16.7 vol%) were used as fuel and oxidizing gases, respectively. The flow of methane was stopped as soon as the CH_4 conversion dropped below 30% and the reactor was flushed with He (20sccm). The subsequent oxidation was continued until O_2 breakthrough was observed. The catalyst is fully regenerated in the oxidation half-cycle, as demonstrated by the CO, CO_2 products formed (see t = 20-36 min for the first cycle) and by the close match of the performance of the subsequent reduction half cycle in terms of the peak shapes and heights. Somewhat surprisingly, the oxidation of the carbon in the oxidation half cycle result predominantly in CO formation (rather than full oxidation to CO_2).

This periodic process, which effectively results in an overall methane partial oxidation process, hence could be operated in a stable way and results already in fairly efficient separation of CO production during the oxidation half-cycle and H_2 production during the reduction half-cycle. However, as the concentration time-traces in figure 6 indicate, the product stream from the cracking half-cycle still contains significant amounts of unconverted methane feed and an initial strong CO_2 peak from methane oxidation, both of which need to be reduced significantly in order to make the process industrially relevant.

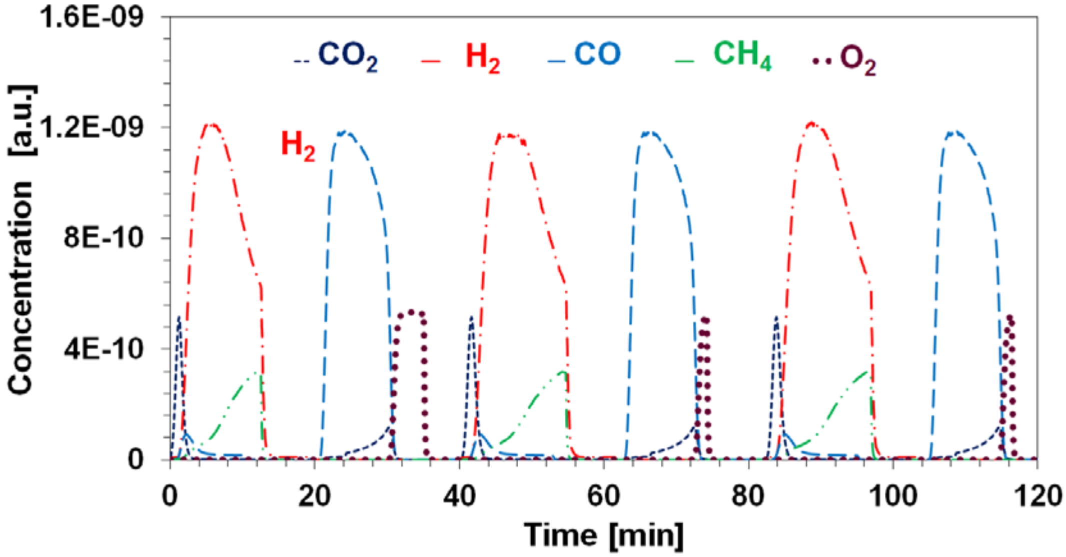

Figure 38. Concentration traces of outlet gases produced during periodic operation in a fixed bed reactor with 20mg of Ni-CeO_2 (20wt%). Alternating cycles of CH_4 (1 sccm, 16.7 vol%) and O_2 (1 sccm, 16.7vol%) at 900ºC are used to demonstrates successive cracking and oxidation of the carrier.

5.3.5 Effect of Oxidant: O_2 vs. CO_2

As a next step, we hence compared operation of the process with oxygen and with CO_2 as oxidants. Figure 39 shows effluent flow rates during a typical full cycle, i.e. cracking and oxidation, in a fixed bed with O_2 and CO_2, respectively, as oxidizing gases. In both cases the carrier is in the coked state at the start of the experiment (t =0 min). For oxidation with O_2 (figure 7a), CO is initially detected in the oxidation half cycle (t= 2-20min), indicating partial oxidation of the deposited carbon by O_2. Only a small fraction of carbon is converted to CO_2 during the latter part of the regeneration, i.e. once the majority of the carbon is burnt off and the ratio of carbon to available O_2 is reduced dramatically. Finally, CO_x production drops rapidly and oxygen breakthrough is observed (t = ~15min).

During the subsequent cracking half-cycle, CO2 formation is seen at the very onset of the cycle. This indicates that Ni in the carrier material was (partially) oxidized during the oxidation half-cycle with air, and the CH_4 feed hence reacts with NiO to produce predominantly CO_2 (and smaller amounts of CO), as reported and discussed in detail previously[42]. Once NiO is fully reduced to Ni, i.e. all the solid phase oxygen is consumed, catalytic cracking of CH_4 is observed (t = ~29min). While the cracking continues over the next ~10min, as indicated by the continued H_2 production, there is a gradually increasing CH_4 breakthrough, indicating that the carrier has started to deactivate. Finally, when the CH_4 flow rate reaches ~30umol/min (i.e. the CH_4 conversion drops below 30%), the cracking half cycle is terminated and the reactor is flushed with inert gas. Overall, as shown in the schematic (Figure 39a**,** inset), the coked carrier (Ni+C) is hence oxidized by O_2 to regenerate Ni, accompanied by the undesired re-oxidation of Ni to NiO. In the cracking cycle, the oxidized carrier hence first reacts with CH_4 to form (undesired) CO_2, followed by the desired H_2 production via cracking and hence re-forming the coked carrier (Ni + C).

Figure 39b shows in comparison effluent flow rates during a typical full cycle when CO_2 is used as oxidant. As before, the carrier is in the coked state at the start of the experiment (t =0min). When the CO_2 flow is started, CO_2 readily reacts with the carbon, producing CO over the next ~7 min. Gradually increasing CO_2 breakthrough occurs during this time until t =12min when the CO_2 flow rate equals the feed flow, indicating that the oxidation is complete. In contrast to the operation with air, the subsequent cracking half cycle shows H_2 production from the very onset (t = 20min), indicating that the carrier is in the "active" metallic phase. This agree with prior studies in which we have shown that Ni oxidation by CO_2 is thermodynamically hindered at these conditions, and thus, unlike for O_2, the carrier remains in the reduced state (Ni-CeO_2) during the oxidation with CO_2 [26,57]. The small initial amount of CO (t = ~20-24min) likely results from the reducible nature of CeO_2 which can contribute a small fraction of its lattice oxygen during the reaction[42]. This is supported by the fact that the CO peak was completely absent for samples reduced in H_2, due to maximum reduction of CeO_2. Previous reports suggest that CeO_2 can be oxidized by CO_2, which would hence explain the CO produced in the cracking cycle[158]. The overall product yield to H_2 when the coked sample (Ni+C) is oxidized by CO_2 is ~53% as compared to the ~42% when air is used as an oxidant. Therefore, using CO_2 as a "soft" oxidant in the periodic cycles not only enable CO_2 activation via reduction to CO in the oxidation half cycle, but also strongly enhances the overall product yield in the cracking half cycle

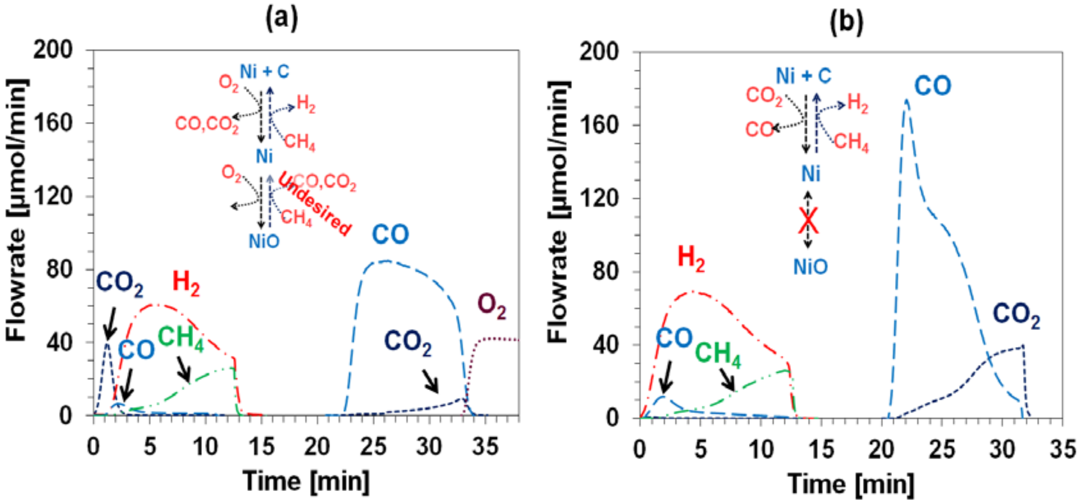

Figure 39. Comparison of a typical full cycle: cracking (CH_4, 1sccm, 16.7 mol%) and oxidation using a) O_2 (1sccm, 16.7 vol%) and b) CO_2 (1sccm, 16.7vol%) in a fixed bed reactor at 900°C. CO_2 as an oxidant improves selectivity of the subsequent reduction half cycle due to suppression of the Ni oxidation to NiO.

5.3.6 Proof of concept: Inherently separated streams of CO & H_2

The present work aimed to demonstrate a process which allows for efficient production of separated syngas streams, i.e. production of high-purity H_2 and CO effluent streams. However, in the experiments discussed above, the oxidation half cycle shows gradual CO_2 breakthrough just ~2 minutes after the start of the oxidation, indicating incomplete conversion. More importantly, during the cracking half-cycle, methane conversion is also still rather low, with the duration of maximum CH_4 conversion only a very short fraction of the half-cycle (~1-2 min, t = 23-25min in Figure 39b). In order to increase conversion and hence achieve high purity H_2 and CO streams, we increased the contact time, i.e. decreased the weight hourly space velocity (WHSV = mass flow of gases/mass of carrier), by a factor of 5 by extending the carrier bed to 100mg Ni-CeO_2 and keeping all other conditions the same.

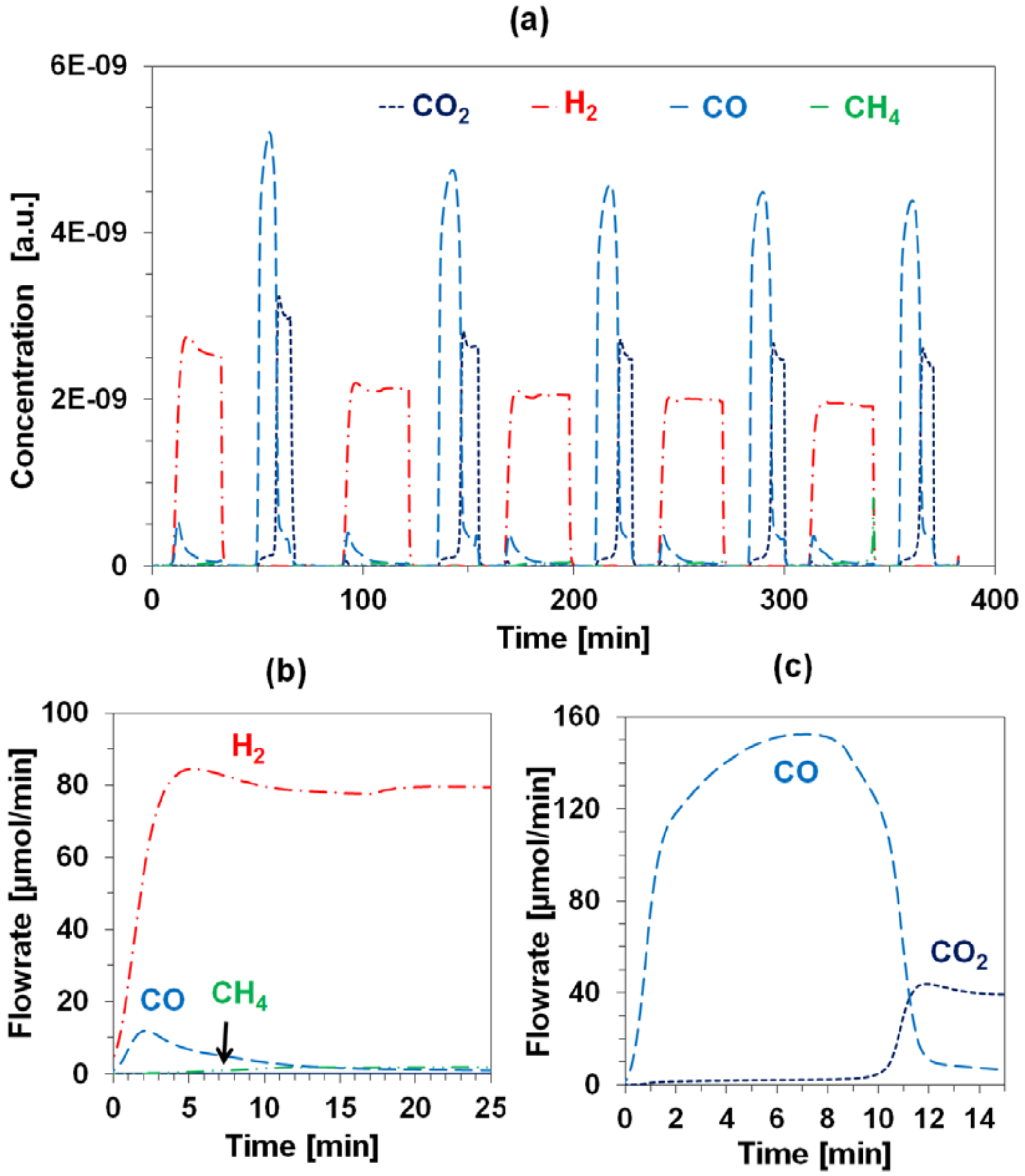

Figure 40. a) Concentration traces during periodic operation in a fixed bed reactor for successive cracking-oxidation cycles with CH_4 (1sccm, 16.7 vol%) and CO_2 (1sccm, 16.7 vol%) over 100mg of Ni-CeO_2 (20wt%) at 900°C. The outlet gas flow rates for: b) cracking half cycle and, c) oxidation half cycle are shown. Highly pure streams of H_2 and CO are produced demonstrating the proof-of-concept.

Figure 40a shows again the concentration traces obtained during fixed bed reactor tests for five successive cracking-oxidation cycles with CH_4 (1sccm, 16.7 vol%) and CO_2 (1sccm, 16.7 vol%) at 900^{o}C. The concentration traces are similar in peak shape and heights (following a slight initial decrease for the fresh carrier), hence suggesting successful cracking and oxidation reactions. Figure 40b shows effluent flow rates during a single cracking cycle for better visibility. As discussed before, a small CO peak is detected at the onset of cracking (t = 0-10min) due to the reducibility of the CeO_2 support. However, after t ~12min, a high-purity stream of H_2 is obtained with hydrogen purity ~94% and a CH_4 conversion of ~95%. The cracking cycle was manually terminated at t = 26min to avoid potential plugging of the reactor due to carbon production.

The reactor is flushed with He before starting the oxidation half cycle which is shown in Figure 40c. A high-purity stream of CO (~98%) at high CO_2 conversion (~99%) is formed over the entire oxidation half cycle, up until CO_2 breakthrough at t = 10min. Overall, the combination of the cracking and oxidation cycles hence demonstrate the proof-of-concept for the formation of a separated syngas stream with high product selectivity at high feed conversions. Clearly, further optimization of process parameters (which was not the aim of the present study) is likely to yield further improvements.

5.3.7 Process Energetics:

In addition to the process parameters such as conversion and selectivity, the viability of the proposed process also depends on the net energy demands. The heats of reactions (at 900^{o}C) for the various reactions involved are as follows:

$$CH_4 + Ni = (Ni{+}C) + 2H_2 \qquad \Delta H_R = 93.8\ kJ/mol \qquad Eq.\ (35)$$

$$(Ni{+}C) + CO_2 = 2CO + Ni \qquad \Delta H_R = 166.3\ kJ/mol \qquad Eq.\ (36)$$

$$Ni + CH_4 + CO_2 = 2H_2 + 2CO + Ni \qquad \Delta H_R = 260.1\ kJ/mol \qquad Eq.\ (37)$$

Both, methane cracking (Eq 35) as well as carbon oxidation by CO_2 (Eq 36) are endothermic. While the overall process using CO_2 as oxidant "consumes" (i.e. activates) CO_2 very efficiently (1 mol CO_2 / mol CH_4 rather than 1/3 mol CO_2 per mol of CH_4 as for conventional dry reforming processes), the net reaction is a highly endothermic methane dry reforming. While renewable energy sources, such as concentrated solar power, could be used to supply the heat for this process in order to assure a net negative carbon footprint, such technologies are immature at this point and not likely to become industrially viable at sufficient scale over at least the next decade. However, in the absence of mature renewable energy based technologies, it is hence important to conceptualize fossil energy based alternatives which still minimize the carbon footprint.

$$CH_4 + 2O_2 = CO_2 + 2H_2O \qquad \Delta H_R = -801.4\ kJ/mol \qquad Eq.\ (38)$$

In the simplest configuration, one could consider using an externally fired natural gas burner to supply the required process heat (Eq 4). Comparing the heats of reaction (Eq 3 and Eq 4), we can see that for 1 mol of CH_4 burnt (or 1 mol of CO_2 produced) during combustion, ~3 mol of CH_4 can be converted or (~3 mol of CO_2 consumed) in the net dry reforming process. Assuming a ~50% efficiency of the heat transfer from the burner, the overall process could hence still run autothermally with a net CO_2 utilization (~1.5 mol CO_2 consumed per mol of CO_2 produced). However, such a process would consume high-purity CO_2 feeds and produce dilute CO_2 combustion emissions and hence yield an efficiency penalty in an overall life-cycle analysis.

A more desirable alternative would make the process inherently energy "self-sufficient". Figure 41 shows a proposed alternative which would operate the process with net CO_2 utilization while ensuring overall autothermal operation. In this configuration the oxidation is carried out in a 2-step manner. First, enough carbon is burnt off using O_2 to yield the energy needed to balance the endothermal heat of the cracking and CO_2 reduction steps. Since this combustion occurs within the carrier bed, which would hence act as a—drastically more efficient—regenerative heat exchanger, the energy efficiency would strongly increase due to this heat integration. An energy balance allows to estimate that ~92% of the deposited carbon would have to be converted with O_2 to CO to enable autothermal operation. By optimizing the weight hourly space velocity, selective CO production can be achieved (as seen in Figure 39a). While we saw above that O_2 can readily oxidize Ni to NiO and thus hamper the selectivity in the subsequent cracking cycle, in this configuration the oxidation would switch back to CO_2 as oxidant for the remaining carbon before the Ni would be exposed to the oxygen stream, hence keeping Ni in its active metallic state. The downside of this configuration is the need for an (expensive) air separation unit and a significant reduction in CO production. However, there are definite possibilities to ensure an energy efficient process.

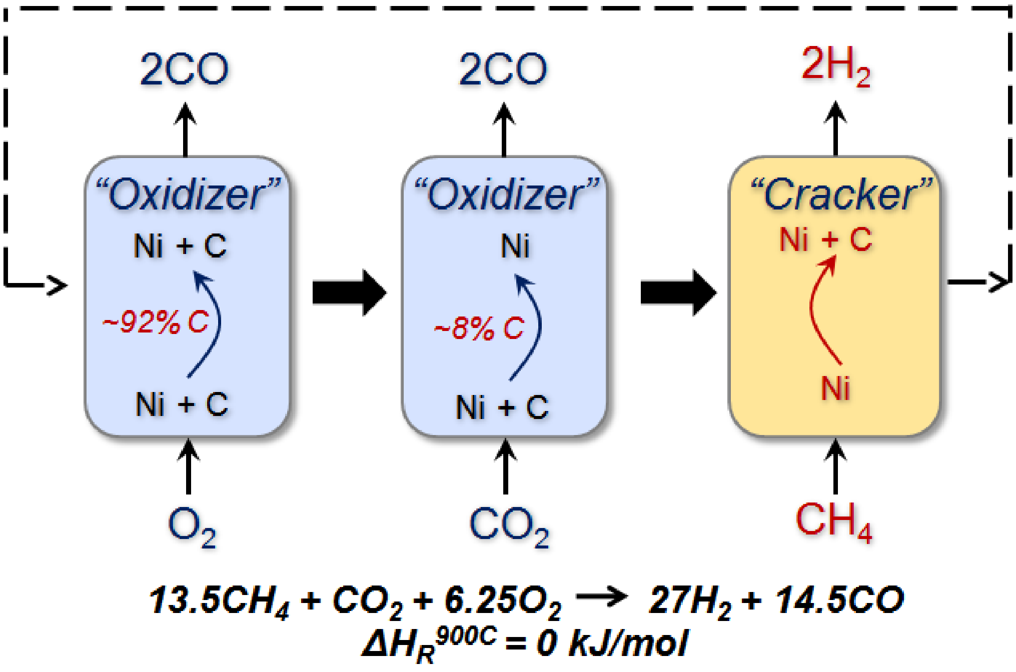

Figure 41. Schematic of the modified process operation to produce high purity H_2 & CO streams, with a net CO_2 utilization with an overall autothermal operation.

5.4 CONCLUSIONS

Increased shale gas production has renewed interest in conversion of methane to valuable chemicals. In the absence of economical direct routes for chemicals production from methane, there is interest in development of scalable technologies for conversion of methane to syngas as the first and most energy and capital intensive step in indirect methane upgrading routes. We have previously demonstrated that chemical looping enables production of syngas from methane via CLPOM and via CLDR, the chemical looping equivalents of partial oxidation and dry reforming processes, respectively[46,57,142]. While both processes can produce syngas with a desirable H_2:CO ratio of 2 (required for major downstream processes such as Fischer-Tropsch and methanol synthesis), further increase in the flexibility of the process could be obtained by producing syngas of tailorable compositions.

In the current study, we propose a process for production of completely separated syngas streams, i.e. production of inherently separated streams of H_2 and CO, via chemical looping methane cracking. Thermocatalytic methane cracking is carried out using CeO_2 supported Ni carriers, resulting in the production of high purity H_2 streams along with carbon deposition. Utilizing a reducible support with strong metal support interactions (i.e. ceria) allows efficient production of carbon (and hydrogen) at elevated temperatures and thus high fuel conversion at high throughput, making the process well suited for scalable, decentralized application. The deposited carbon can be effectively removed by reaction with either O_2 or CO_2 to regenerate the active Ni species. Using CO_2 as a “soft” oxidant not only allows for CO_2 activation via reduction to CO (enhancing the CO yield from the process and enabling CO_2 utilization), but also improves the overall process selectivity by selectively oxidizing carbon while keeping Ni in its metallic state active and selective for catalytic cracking.

While the overall process is similar to conventional dry reforming of methane, it builds kinetically on two different, spatially or temporally separated reactions: catalytic cracking and the reverse Boudouard reaction, coupled together using a “carbon carrier”. The use of a reducible support (CeO_2) in place of conventional support (such as $MgAl_2O_4$), not only facilitates a more efficient production of hydrogen via thermocatalytic methane decomposition, but also opens up possibilities for further process optimization via a modified growth mechanism of the carbon filaments as a function of the metal-support interactions.

Finally, on a conceptual basis, it seems worthwhile noting again that in this proposed process Ni effectively acts like a “carbon” carrier, which shuttles carbon (produced from methane in the “cracker”) to the oxidizer, where it is oxidized to CO. Thus, the current process constitutes an extension of the chemical looping concept beyond the realm of oxygen carriers and hence, oxidation reactions. Furthermore, while most chemical looping processes take advantage of the ability of chemical looping to separate a feed stream (such as N_2 and O_2 in process air), the current configuration utilizes the inherent separation in chemical looping to separate the stream of produced gases to yield an inherently separated product stream. Given the crucial role of separation for the chemical process industry (both for efficiency, cost, and environmental footprint)[159], it seems that application of the chemical looping principle with a focus on product separation may constitute a fruitful area for development of next-generation highly intensified chemical processes.

6.0 SUMMARY AND CONCLUSIONS

The burgeoning global population and the rapidly developing world economies are together expected to increase the demand for commodity chemicals. Recent advances in drilling technology have made shale gas (>95% CH_4) a cheap and widely available feedstock for chemical production. However, in the absence of proven commercial technologies for direct conversion of CH_4 to chemicals, all current processes require conversion of CH_4 to syngas (mixture of CO + H_2) a first-step. Downstream syngas utilization requires specific H_2:CO ratios (1 or 2), pure H_2 streams or pure CO streams depending on the chemicals produced, and thus tremendously increasing the separation and energy costs. Hence, alternative syngas production techniques are required which can sustainable chemical production with CO_2 utilization.

‘Chemical Looping Combustion’ is a clean combustion technology, which enables fossil fuel combustion with inherent CO_2 capture based on the cyclic oxidation and reduction of an oxygen carrier. While most efforts in chemical looping (CL) are focused on combustion, in this work we investigated and compared two different operating modes of CL beyond combustion. In the first scheme, CO_2 reduction is coupled with CH_4 oxidation by using mixtures of Fe and Ni (as alloys or simple physical mixtures) to produce CO and syngas product streams. In the second operating scheme, monometallic Ni carriers are utilized to catalytically crack CH_4, producing pure H_2 streams. The solid carbon deposits are then burnt off with CO_2, overall producing separate CO and H_2 product streams. In both the operating modes, the overall reaction is a modification of dry reforming of methane ($CH_4 + CO_2 \rightarrow 2CO + 2H_2$) called chemical looping dry reforming (CLDR). The crucial advantage of the chemical looping configuration lies in the inherent separation of the product streams. In the first mode of CLDR operation, streams of syngas (H_2:CO ~2) and pure CO are produced which can be used separately: syngas for gasoline (via Fischer-Tropsch synthesis) and methanol production, and CO for acetic acid production (Monsanto process); or mixed together (H_2:CO =1) for use in formaldehyde manufacture. In the second mode of operation, the separated H_2 and CO streams can be used virtually in any combination, or pure H_2 can be used individually for NH_3 synthesis. Overall, CLDR generates directly usable syngas streams, which can dramatically improve the process flexibility and avoid the need for expensive gas separations.

Since the "solid" oxygen availability in metal oxide carriers influences gaseous product selectivity, rational carrier design was an important goal of this work. The gas-solid reaction is mass transfer controlled via the metal-oxygen bond strength, with the high temperatures of operation negating any possibility of kinetic limitations. Our work demonstrates that while FeO_x can selectively convert CH_4 to syngas, the presence of a small fraction of reactive Ni centers (as in a Fe-Ni alloy), can significantly improve CH_4 activation and the overall reactivity. Conversely, the presence of Fe enables the Ni reoxidation with CO_2 and thereby facilitates its conversion to CO. This concept of synergistic combination using alloys is relatively new in chemical looping, as opposed to the field of heterogeneous catalysis where it has been explored widely[160,161]– primarily due to influence of modified electronic properties on reactant activation[162]. Interestingly, the chemical looping system utilizes the intermetallic association beyond reactant activation and towards co-operative oxygen transport (which occurs during the redox processes). It is also worthwhile to point out that while the CLDR process facilitates the

CO_2 utilization, the weaker oxidant CO_2 in turn enables the process by controlling alloy oxidation and improving syngas selectivity. This suggests that CO_2 can have desirable properties as an oxidant for a broad spectrum of selective oxidation reactions (oxidative dehydrogenation of ethane to ethylene), since a majority of them suffer from over oxidation and usually require discriminating control over reactant oxidation. Broadly, our results suggest that the alloyed carriers likely hold much broader potential for redox processes in a “looping” configuration than one might anticipate, as a smart combination of two metals might allow the reconciliation of contradictory demands in the two, coupled half-cycles.

While the alloys are stable over extended cyclic operation, it is likely that the intermetallic phases are dynamic under the periodically changing reactive conditions. This hinders a thorough understanding of the mechanistic aspects of the reactions which can be crucial for a successful process scale-up. Hence, physical mixtures of metal components can represent a simpler alternative to alloys in terms of the carrier design. We demonstrated that, surprisingly, the use of simple physical mixtures of two monometallic carriers (Fe and Ni) can yield similar synergies, albeit based on a completely different coupling mechanism: While the Fe-Ni alloy carriers in the earlier study relied on the “shared” use of lattice oxygen between the coexisting metals in the oxide lattice, the physical mixture relies on a gas-phase mediated cooperative mechanism, where the initial activation of one reactant over the first metal is coupled with the subsequent conversion of the intermediates over the second metal. The product from this secondary conversion is then undergoing another reaction step, forming the final product. Overall, the physical mixture components work cooperatively to convert CH_4 to syngas. Broadly, this concept can be considered similar to bifunctional asymmetric catalysts, where cooperative Lewis acid and Lewis base pairs work together to promote a specific reaction[163,164].

However, better analogies are few interesting zeolite/metal-oxide systems[165,166] for Fischer Tropsch synthesis: Syngas is converted to an active intermediate over one catalyst/active site and transported via gas-phase to the second catalyst/active site for a final conversion to olefins/dimethyl ether. However, the key difference is while the physical mixture components in these studies are catalysts that act successively, the physical mixture components in our work are a catalyst-“oxygen” reservoir combination which acts in a cyclic manner (see Chapter 3 for more details). In general, the use of simple physical mixtures opens another window for rational process design which can build on an ever increasing number of published studies on (monometallic) oxygen carriers in chemical looping oxidation processes and on the availability of thermodynamic databases for a large number of metal/oxide systems.

The configuration for separated streams of CO and H_2 consists of two different, spatially or temporally separated reactions: catalytic cracking ($CH_4 \rightarrow C + 2H_2$) and the reverse Boudouard reaction ($CO_2 + C \rightarrow 2CO$), coupled together using a “carbon carrier”. This represents an extension of the chemical looping concept beyond the realm of “oxygen carriers” and hence, oxidation reactions. More importantly, this configuration demonstrates the true potential of chemical looping in completing eliminating downstream product separation. Syngas separation to H_2 and CO is primarily done using Pressure Swing Adsorption (PSA) process at high pressures and near ambient temperatures[167]. Syngas is almost always produced at $T > 800^oC$ which needs to be cooled down to room temperature and then separated using PSA. The separated components need to be heated back up to reaction temperatures (typically $>300^oC$) for downstream utilization, thus making the overall process highly inefficient. Similarly, polymeric membranes used for non-condensable gas separation also operate at a maximum $T \sim 70^oC$, with high temperature-stable ceramic membranes costing ~10-100 times as much[168]. On the contrary, chemical looping process not only offers inherent separation, but also produces streams that can be used directly or with minimal heat manipulation. Given the crucial role of separation for the chemical process industry for efficiency, cost, and environmental footprint[159], it is likely that other “carrier” systems (like “sulfur carriers” discussed in Chapter 6.2) can present cost-effective alternatives.

The inherent separation of product streams offered by the chemical looping platform, requires operation in a cyclic manner. From an applied perspective, periodically operated batch-wise processes are more complicated than continuously operated steady-state processes. However, periodic operation can sometimes offer sufficiently improved reactor performance to offset any higher operating or capital costs. Improvements in terms of synthesis rates[169], yield[170,171], catalyst life time [172] or even disposal of dilute by-products[173], has been reported in the literature. Correspondingly, a successful commercial demonstration of a cyclic process has been partial oxidation of butane to maleic anhydride (a polymer precursor) by DuPont[174]– at the time (~year 1999) producing 180million pounds per year. In recent years, demonstrations of chemical looping combustion for power generation have also been successfully operated in a cyclic manner at pilot plant scale operations for an extended time (~ 150kWh for 4000 hr)[53,55,175]. While the largest demonstration (~1MW)[176] is still far from a commercial scale operation (~500MW), these reports suggest a steadily growing expertise in automated cyclic operations. The vigorous operating conditions in the circulating fluidized bed used made solid (catalyst) loss via attrition an initial concern. Yet, modified synthesis techniques such as spray drying, have been successfully implemented for developing attrition resistant catalysts.

Catalytic dry reforming (DR) of methane, where CH_4 and CO_2 streams are co-fed continuously over a catalyst bed, is the steady-state equivalent of the chemical looping dry reforming (CLDR) process described in this work. Since one of the major challenges in conventional dry reforming is catalyst deactivation due to carbon deposition, a small fraction (1-3%) of precious metals (Rh) is typically incorporated into the catalyst to prevent carbon deposition. Recent reports suggest that such Rh-containing catalysts typically show conversions of ~95% with reduced carbon deposition over ~8h operation at 750°C[177]. In comparison, the CLDR process using Fe-Ni alloys produces similar conversion numbers while operating at 1000°C. Since, both studies were carried out in a similar fashion, viz. fixed bed reactors on a lab scale (~100mg bed), approximate comparisons can be made. While the operating temperature for the DR process is significantly (250°C) lower than CLDR, Rh is ~1500 times more expensive than Ni and Fe. By a conservative estimate for the metal loading, i.e. ~1wt% Rh for DR and ~40wt% Fe for CLDR, the DR catalyst is ~35 times more expensive than the CLDR carrier on a catalyst weight basis. While the turn-over number (mol of syngas/g catalyst) for the DR catalyst is ~2.3 times that of CLDR carrier, using ~3 times the amounts of carrier in CLDR process can also potentially offer similar turnover numbers. Overall, the DR process operates continuously (steady-state) at a lower temperature (lower operating costs) and the CLDR process offers flexible H_2:CO ratios in a batch-wise manner at lower carrier/catalyst costs. A detailed process and economic analysis at a larger operating scale will be required to further elucidate the benefits of either process. On the other hand, both the dry reforming processes, will offer CO_2 utilization albeit at the cost of energy input ($CH_4 + CO_2 \rightarrow 2CO + 2H_2$; ΔH_R ~250 kJ/mol). A quick calculation shows that an externally-fired CH_4 furnace can supply the required energy while still keeping the overall process i.e. external combustion + dry reforming, a net CO_2 consumer; autothermal operation with a slightly lower CO_2 utilization ~0.5 mol CO_2 consumed/mol CH_4 as compared to 1 mol CO_2/ mol of CH_4 for the original dry reforming process. Alternatively, energy derived from renewable sources such as concentrated solar power (CSP) can also be used. In any case, both configurations (conventional and cyclic) of dry reforming processes offers a pathway to upgrade CO_2 to syngas and further on to liquid fuels such as gasoline (via Fischer-Tropsch processes), thereby conceptually closing the CO_2 cycle.

In the long run, it is unlikely that any single technology will offer a total solution for efficient CO2 utilization. More importantly, the magnitude of CO2 emissions (mainly from power plants), is significantly higher than any current market for CO2 utilization. Hence, technologies like dry reforming, are directed towards sustainable chemical production and prevention of additional CO2 emissions. The chemical looping platform presents an exciting opportunity towards this goal. However, the incorporation of CO2 in the chemical process industry will not only require strict regulations on future emissions, but also incentives for CO2 utilization.

7.0 OUTLOOK

7.1 CRYSTAL GROWTH AND DESIGN FOR HOLLOW AND NON-HOLLOW CERIA PARTICLES

Production of inherently separated streams of H_2 and CO via chemical looping involves coupling of two reactions– catalytic cracking of methane to produce solid carbon and H_2 (in “cracker”) and carbon removal via CO_2 oxidation thereby producing CO (in “oxidizer”). During catalytic cracking, carbon filaments are formed which “lift-off” the metal particle from the support. Thus, oxidation of these filaments can potentially result in loss of the metal particles with the product gases (Figure 42). In order to avoid the metal particle loss and thereby make the overall process sustainable over a large number of cycles, we proposed development of novel core-shell structures with the metal particle enclosed within the shell. Based on our earlier studies, the Ni-CeO_2 system was chosen as the potential candidate for this process and hence the end-goal of this work was to produce a core-shell structure (Ni@CeO_2).

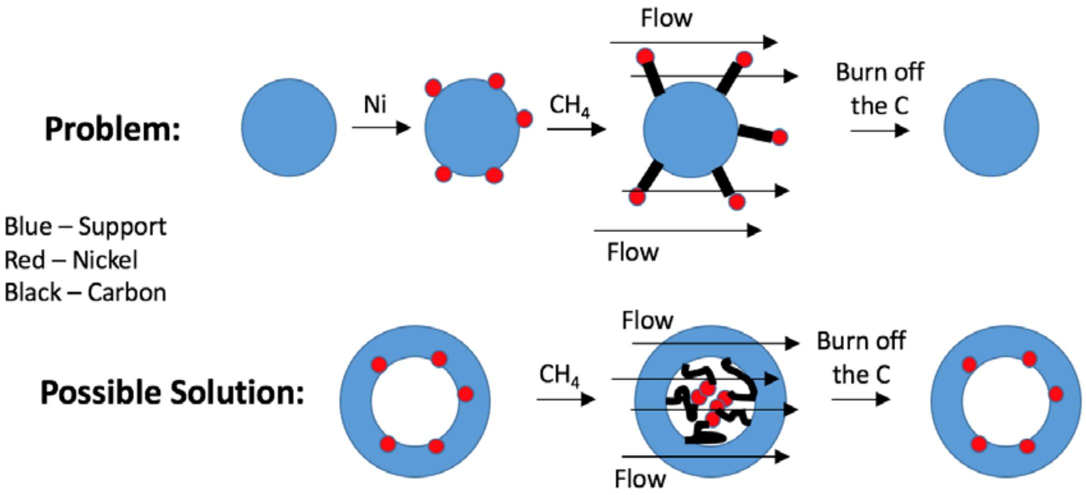

Figure 42. Schematic of the proposed synthesis.

It is by now well established that the relative high abundance has made ceria a very popular material in variety of chemical processes such as automotive exhaust catalysis[178,179], water-gas shift (WGS) reaction[180,181], fuel cells[182,183], as well as in the fields of biotechnology[184], environmental chemistry[185,186], and medicine[187]. Moreover, decreasing the ceria particle size strongly reduces the energetics for defect formation, thus dramatically influencing the generation electronic carriers which are potentially responsible for the enhanced catalytic activity[188]. Correspondingly, there has been significant work on development of ceria nano-structures. Hydrothermal synthesis is an easy, scalable and effective technique for synthesis of ceria structures. However, a majority of techniques rely on use of surfactants or structure directing agents to achieve the desired shape[189-191].

Reports in the literature suggested a SiO_2 template based approach for generation of core-shell ($SiO_2@CeO_2$) structures followed by a selective removal of the SiO_2 to form hollow ceria spheres ($@CeO_2$). Hence, by depositing Ni on SiO_2 as a first step and following the same approach, we can in principle form the desired Ni@CeO_2 structures. However, to gain a better control of the synthesis, we focused on creation of the hollow CeO_2 spheres as a starting point. Two separate protocols were used– controlled precipitation of cerium precursor via drop wise addition and hydrothermal synthesis. The first approach resulted in successful production of the core-shell SiO_2@CeO_2 structures, although the removal of SiO_2 template caused the crumbling of the shells due to the small shell thickness. Subsequent efforts to increase the shell thickness were unsuccessful, since they resulted in formation of extraneous CeO_2 particles. The hydrothermal synthesis was carried out in two different sized reactors (90mL and 45mL) using synthesis protocols scaled according to the reactor volume. The reactor with the larger volume resulted in formation of extraneous spherical CeO_2 particles (~150nm) without any apparent ceria deposition on the SiO_2 template (Figure 43). On the other hand, the smaller reactor volume resulted in formation of a mix of core-shell SiO_2@CeO_2 structures and spontaneously formed hollow CeO_2 (@CeO_2) structures (Figure 44). At this point, it is not entirely clear what causes the formation of these structures. It is likely that the relative rates of nucleation and agglomeration, which are controlled by the reaction conditions (reactor volume, temperature and reducing agents) play an important role in the process.

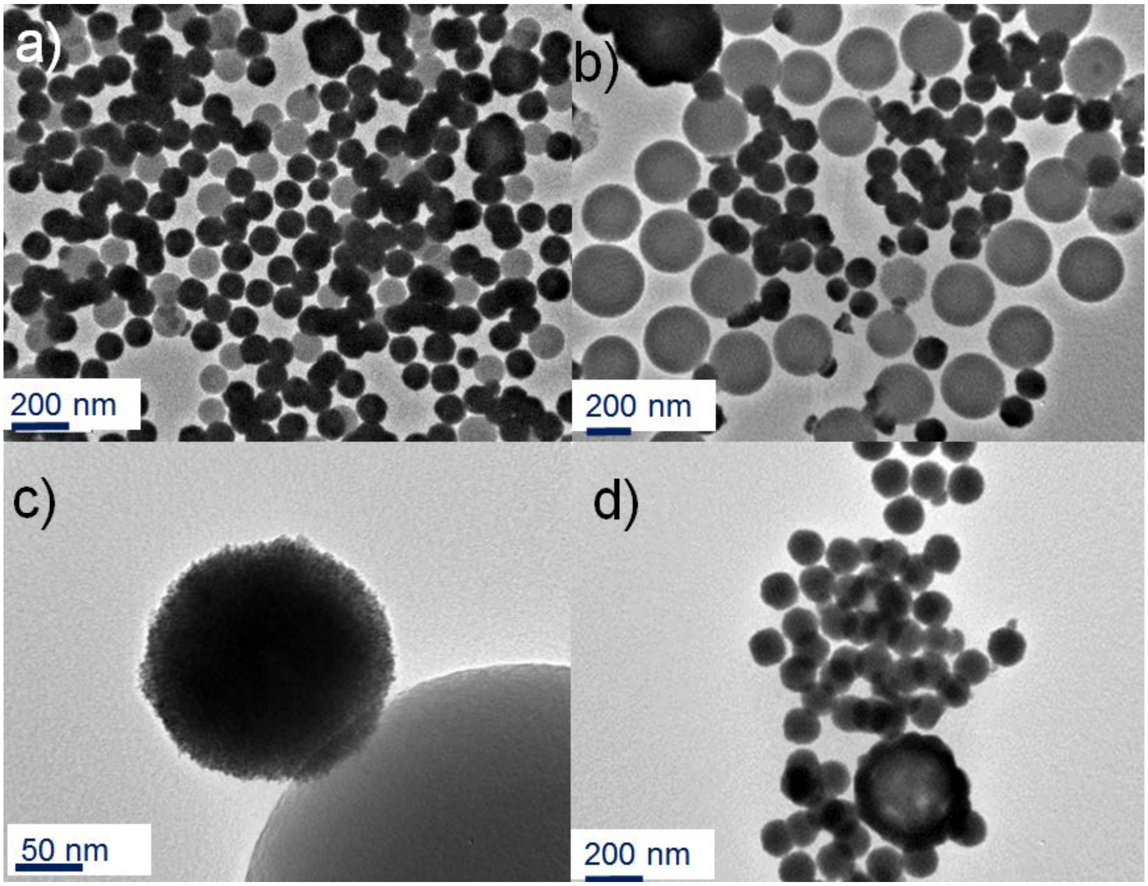

Figure 43. TEM images of samples produced using hydrothermal synthesis: a) using smaller SiO_2 (231nm±12nm), b) using bigger SiO_2 (387±34nm) showing the presence of bare SiO_2 spheres (lighter contrast), spherical CeO_2 particles (darker contrast) and a small fraction of core-shell structures (top left), c) No visible layer of ceria on SiO_2 sphere and the ceria particle is possibly formed by self-assembly of the smaller (~2-3nm) ceria nuclei visible around the edges, and d) Post NaOH etching results in complete removal of SiO_2 particles without the removal of CeO_2 particles or core-shell structures

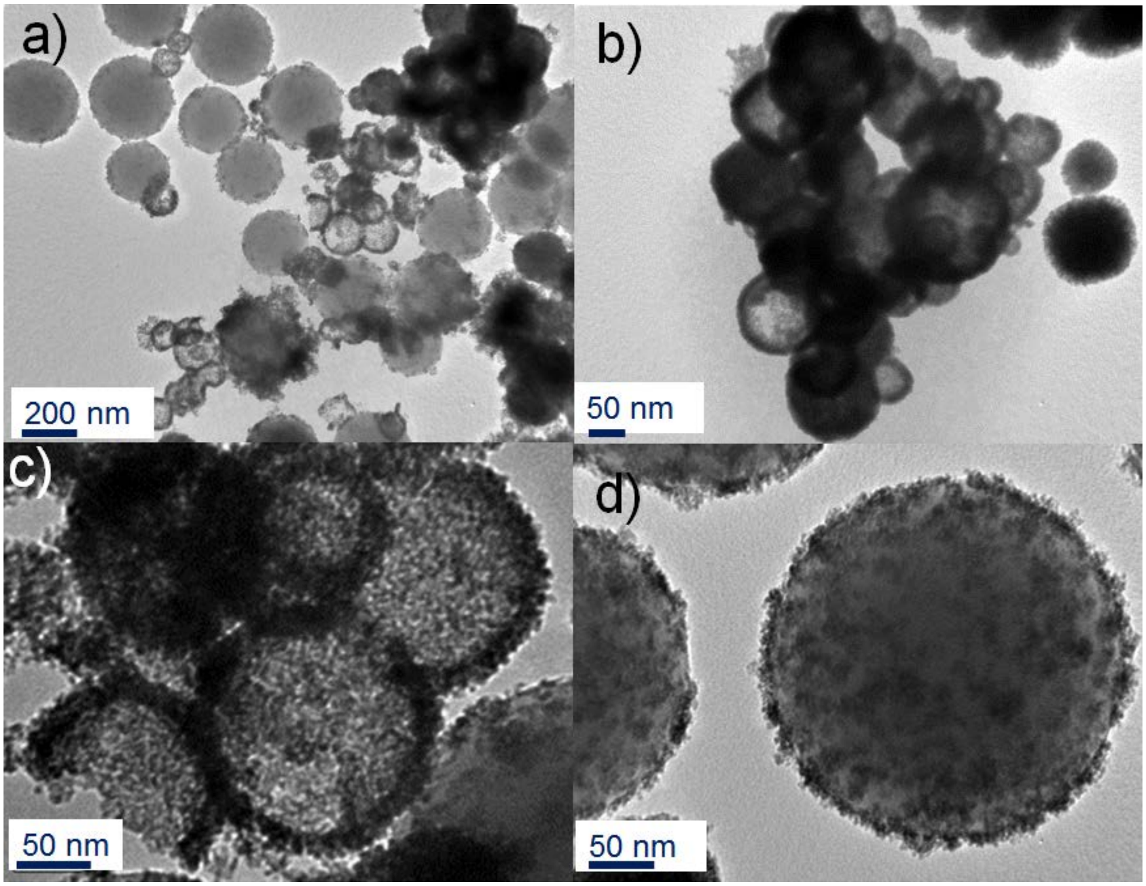

Figure 44. TEM images of samples produced in scaled hydrothermal synthesis a) with SiO_2, b) without SiO_2, c) spontaneously formed ceria shell (with SiO_2), and d) ceria covering on SiO_2 spheres.

Our current results show a simultaneous presence of three different structures– solid CeO_2, hollow ceria (@CeO_2) and core-shell (SiO_2@CeO_2. Understanding the formation mechanisms will thus allow better control over reaction pathway for a particular structure. Li and co-workers have reported the synthesis of hollow ceria nano-spheres without the use of surfactant[192]. However, they offer no explanation about how the various reaction parameters (temperature, reducing agent, reactor volume etc.) control the crystallization-nucleation process. Clearly, a balance between the rate of nuclei formation and agglomeration will not only control the size of the solid ceria particles, but also influence the propensity towards hollow shell formation. Simplistically, the underlying processes can be considered a series of simultaneous and parallel reactions, which could be modelled mathematically to develop correlations relating particle size as well as structure to the reaction parameters. Although non-trivial, a computational study of this kind will not only provide a better understanding of the process, but also better direct future experiments towards a successful synthesis.

7.2 SULFUR CARRIERS FOR ETHYLENE PRODUCTION VIA CHEMICAL LOOPING

In addition to syngas, ethylene (C_2H_4) is one of the most important chemicals in terms of volume as well as value for production of a number of chemical derivatives. Thus, a reduction in the price of ethylene or its parent compounds (natural gas) will significantly affect the cost of a number of consumer products. The ~70% drop in natural gas prices due to the shale gas discoveries is expected to result in a nearly equivalent drop in the cost of ethylene production, making the economics very competitive on the global level (PWC)[193]. Hence, it is highly desirable to develop a process that can convert natural gas directly to ethylene.

Recently, research groups of Marks & Neurock reported elemental sulfur as a promising oxidant for selective methane conversion to ethylene over MoS_2, RuS_2, TiS_2, PdS and Pd/ZrO_2 catalysts[194]. In comparison to O_2, the thermodynamic driving force for methane over-oxidation by S_2 is significantly less, thus it is a 'softer' oxidant. Moreover, the oxidative coupling of CH_4 by S_2 to form C_2H_4 ($2CH_4 + S_2 \rightarrow C_2H_4 + 2H_2S$, $\Delta G_{1073K} = -4.9$ kJ mol^{-1}) is thermodynamically viable, while that to form C_2H_6 ($2CH_4 + 1/2S_2 \rightarrow C_2H_6 + H_2S$, $\Delta G_{1073K} = 33.9$ kJ mol^{-1}) is a thermodynamically uphill reaction and the over-oxidation of methane to CS_2 or other species is far less favorable than the analogous over-oxidation by O_2. Subsequent work by Peter and Marks showed transition metal sulfides (Fe, Ti, Cr) show ethylene selectivity >25%[195]. However, both these studies are based on reaction of gas-phase sulfur with CH_4. With a boiling point of ~450^{o}C, a commercial process of this kind would require heated and insulated lines to ensure the condensation of sulfur is avoided. On the other hand, H_2S is a gas under all the relevant conditions making the handling much easier. It is hence proposed to utilize the concept of using “sulfur” as a soft oxidant for conversion of methane to ethylene, in a chemical looping scheme with H_2S (sulfur feedstock).

Metal oxides have been used as sorbents for removal of H_2S from coal-derived synthesis gas and thus have been studied widely. Mangnus et al. reported that it is easier to sulfide the surface and core of Ni(0) than that with Ni(II), and NiS could be readily formed at the temperature range of 370-850 K[196]. Reshetenko et al. found that the H_2S decomposition reaction on α-Fe_2O_3 leads to reduction of oxides and simultaneous formation of surface Fe(II)S[197]. The interaction of H_2S and CuO was more complex: CuS was the main product, but Cu_2S and elemental Cu were formed at high temperature (>400 °C) and higher H_2S concentration. As for manganese, $MnCO_3$ is the stable solid below 400 °C, while MnO is stable above 400 °C. Importantly, manganese shows sulfidation potential at the higher temperature range of 600-700 °C[198]. On the other hand, previous work in our lab and by others has shown that metal sulfide can react easily with air to regenerate the metal oxide in a cyclic manner suggesting suitable stability of these “sulfur” carriers in a H_2S/air cyclic configuration[199,200].

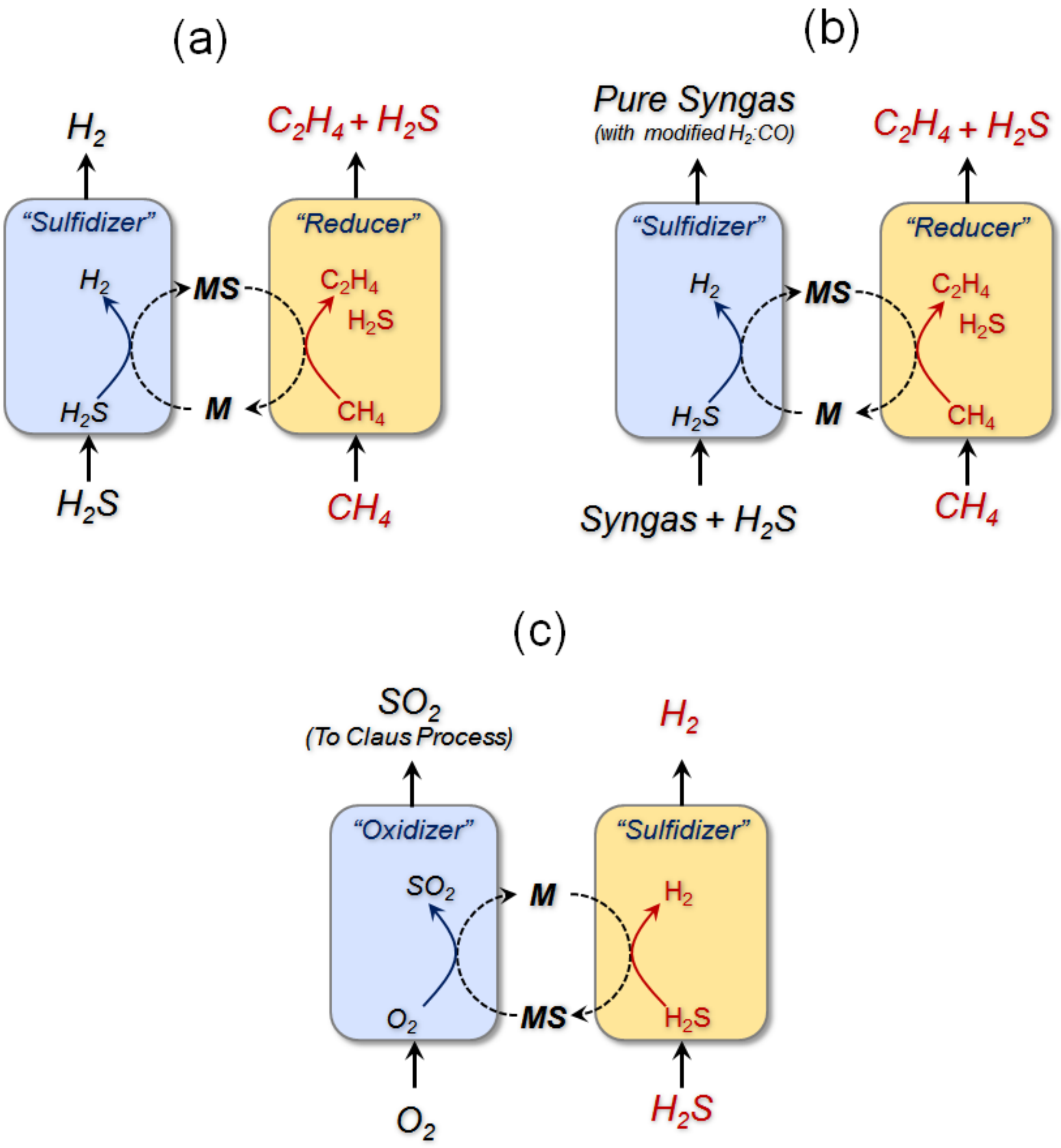

Figure 45. Various process scheme for “sulfur” carriers in chemical looping: a) ethylene production with hydrogen recovery, b) ethylene production with syngas purification, and c) SO_2 (for Claus process) with hydrogen recovery.

The concept of such a process is shown in Figure 45a, for a metal “M” which is reacted with H_2S to generate a metal sulfide, which serves as a “source” of sulfur. The metal sulfide then can facilitate coupling of methane to produce ethylene and H_2S. The “sulfidizer” thereby produces a stream of hydrogen which can be directly used for S recovery in the hydro-desulfurization (HDS)– required for sweetening of “sour” natural gas i.e. natural gas containing sulfur products. Unconverted H_2S in the H_2 stream would not need to be separated beforehand as the desulfurization process is amenable to all sulfur containing products and H_2S is the major byproduct of HDS. On the other hand, the stream from the “reducer” contains equimolar H_2S and C_2H_4. Clearly, separation of H_2S is crucial for any downstream use of the C_2H_4 stream. This separation although non trivial, it is in principle, possible using the existing commercial technologies for natural gas processing. The economic penalties of this separation may largely be offset by any marginal improvements in the selectivity and conversions in the sulfidizer– producing a high value product (C_2H_4) from a very cheap reactant (CH_4).

As a second configuration (Figure 45b), it also possible to use the “sulfidizer” for purification of sour syngas, which is typically formed when sulfur containing coal is used. We have successfully demonstrated a similar concept for combined conduction and desulfurization concept in our earlier work [199]. Here, we suggest a way to simultaneous desulfurize syngas combined with ethylene production. Since the carrier comes to the sulfidizer in a reduced (metallic state), the CO & H_2 components of the syngas stream do not react with the metal. However, the H_2S from the syngas can readily react with the metal to regenerate the sulfide and simultaneously produce hydrogen. Thus the outlet of the sulfidizer would consist of syngas with a higher H_2:CO ratio than the inlet. This modification can significantly increase the overall calorific value of syngas depending on the H_2S concentration. Performing a quick thermodynamic analysis shows that the overall process is endothermic (ΔH_R = ~ 202 kJ/mol)– for both the configuration (a) and (b). Although, not exactly ideal, such a process can be either driven by renewable sources such as concentrated solar power or by external firing. Moreover, using a chemical looping combustion (CLC) or an oxy-fuel technology will fulfil the energy needs in addition to efficient CO_2 capture.

A third configuration for this process can attempt a simultaneous production of hydrogen and SO_2. While the sulfidizer remains the same as before, an oxidizer is used to selectively burn off the sulfur producing a pure SO_2 stream. This SO_2 stream can be utilized downstream in the Claus process for sulfur recovery[201]. Claus process consists of two steps: SO_2 production– $2\ H_2S + 3\ O_2 \rightarrow 2\ SO_2 + 2\ H_2O$ (ΔH^R = -1036 kJ/mol), followed by the Claus reaction– $2\ H_2S + SO_2 \rightarrow 3\ S + 2\ H_2O$. Since the required H_2S: SO_2 ratio for the Claus process is 2:1, a stream of a third of the total H_2S is generally separated beforehand and converted to SO_2 in a free-flame (i.e. lot of flames) and highly exothermic combustion, before being mixed with the remaining H_2S stream. On the contrary, the proposed configuration can produce the required SO_2 stream in addition to a useful hydrogen stream. The overall reaction $H_2S + O_2 = SO_2 + H_2$ (ΔH_R = -276 kJ/mol) is significantly less exothermic, flame-free (i.e. no flame) in both reactors and hence can be operated with improved safety.

Overall, based on the existing studies in the literature and in our lab, the proposed configurations can potentially be tried out using a Fe/Ni supported on CeO_2. Initial tests would have to be conducted in the thermogravimetric analyzer (TGA) to study the sulfidization of these metals in H_2S stream. Characterization of the sulfides using X-ray diffraction (XRD), Scanning electron microscopy (SEM), Transmission electron microscopy (TEM) would help determine the physicochemical properties of the carrier. As a first step, cyclic experiments with air/O_2

oxidation will establish the stability of carrier towards repetitive sulfidization-oxidation cycles. Finally, fixed-bed reactor experiments would be carried out to study the gas-phase selectivity/conversion of the process.

APPENDIX A

SYNTHESIS OF CORE-SHELL SIO_2@CEO_2 STRUCTURES

A.1.1 Material Synthesis and Characterization

The synthesis methodology of the hollow Ni@CeO_2 structures is shown in Figure 46. However, to achieve a better control over the various synthesis parameters, the Ni addition step was eliminated and hence the initial goal was to produce hollow CeO_2 shells. SiO_2 was synthesized using Stöber synthesis[202]. Briefly, H_2O (36 mL), NH_4OH (7 mL) and Ethanol (150 mL) were added to a round-bottom flask and stirred at room temperature to create a homogenous mixture. Then TEOS (6.6 mL) was added to the mixture and stirred vigorously for 3 h. A wet cake was obtained after 3 cycles of washing (with H_2O) and centrifuging, which was dried overnight in a vacuum oven (90^oC). The dried cake was crushed and ground using a mortar-pestle and calcined at 500^oC (2 h, 0.2 SLM air). Re-hydroxylation of SiO_2 was performed by suspending 200mg of SiO_2 in 40mL of DI water, and held at 100^oC for 2 h under continuous stirring. This suspension was then subjected to three cycles of washing-centrifugation and dried overnight in a vacuum oven (90^oC). This cake was ground again using a mortar-pestle to yield the SiO_2 powder.

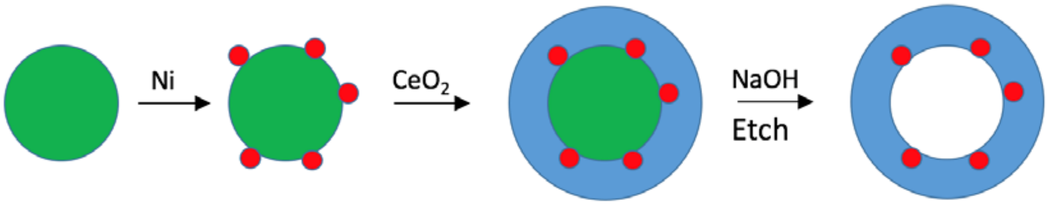

Figure 46. Schematic of the proposed synthesis.

The first synthesis method (denoted as method 1 henceforth) for templated synthesis of CeO_2 shells ($SiO_2@CeO_2$) was adapted from work by Zhang et al[203]. The re-hydroxylated SiO_2 (100 mg) was dispersed in a pH-controlled buffer solution of MOPS (99.5%+, Sigma Aldrich; 0.5232 g in 50 mL H_2O) and sodium hydroxide (added until pH = 7.35). After heating to 70°C, cerium(III)sulfate (240 mg, 99.5%+ purity, Sigma Aldrich) was added to the buffer solution under N_2 atmosphere. The mixture was allowed to react for 2 h under vigorous stirring, at which point it was washed with DI water and centrifuged three times. The final product was dried in a vacuum oven overnight at 90°C, crushed and ground to produce a fine powder. This powder was calcined at 400^{o}C (2 h and 0.2 SLM air).

The second synthesis method (denoted by method 2 henceforth) was adapted from the work by Strandwitz and Stucky[204]. Briefly, 300mg of re-hydroxylated SiO_2 was mixed with 43mL of ethylene glycol to create a suspension. 2.25mL of 1M solution of cerium(III)nitrate (99.5%+ purity, Sigma Aldrich) was added and the mixture was stirred for 10min. Afterwards, the slurry was transferred into a 50 ml autoclave, heated to 130^{o}C under autogenous pressure for 15 h, and then allowed to cool to room temperature. The product was washed by DI water and collected after multiple washing-centrifuging cycles (until solution pH ~7), dried overnight at 90^{o}C, crushed and ground to produce a fine powder. This powder was calcined at 400°C (2 h and 0.2 SLM air).

To test the etching process, samples were dispersed in 5 M sodium hydroxide (NaOH) and stirred for 1, 3, or 5 h. They were then washed, centrifuged, dried, and characterized as before. All the samples were analyzed by JOEL 200CX Transmission Electron Microscopy (TEM).

APPENDIX B

ALTERNATIVE INTERPRETATION OF FE-NI ALLOY OXIDATION IN CO_2

During the thesis defense presentation there was a discussion of the oxygen transport mechanism for the oxidation of Fe-Ni alloys by CO_2. It was suggested that the proposed mechanism (Chapter 2) be presented in an alternative manner.

B.1 EXPLANATION

In the Fe-Ni alloy, Fe is responsible for “extracting” oxygen from CO_2 by breaking the carbon-oxygen bond. The solid oxygen atom thus produced can bond with either Ni or Fe atoms present in the lattice. Since the reaction takes place at high temperatures (~1000^{o}C), it is mass transfer controlled (no kinetic limitations). The oxidation of the Fe-Ni alloy is hence thermodynamically driven, and the presence of Fe enables the oxidation of Ni.

BIBLIOGRAPHY

1. Grasselli RK. Advances and future trends in selective oxidation and ammoxidation catalysis. *Catalysis Today.* 1999;49(1–3):141-153.

2. Gerland P, Raftery AE, Ševčíková H, et al. World population stabilization unlikely this century. *Science.* 2014;346(6206):234-237.

3. Cayuela Valencia R. The Chemical Industry by 2050. *The Future of the Chemical Industry by 2050*: Wiley-VCH Verlag GmbH & Co. KGaA; 2013:221-306.

4. Wilhelm DJ, Simbeck DR, Karp AD, Dickenson RL. Syngas production for gas-to-liquids applications: technologies, issues and outlook. *Fuel Processing Technology.* 2001;71(1–3):139-148.

5. Ren T, Patel MK, Blok K. Steam cracking and methane to olefins: Energy use, CO2 emissions and production costs. *Energy.* 2008;33(5):817-833.

6. Recent Global Monthly Mean CO_2. National Oceanic & Atmospheric Administration-Earth System Research Laboratory (NOAA-ESRL) Physical Sciences Division.

7. Spath PL, Dayton DC. *Preliminary screening-technical and economic assessment of synthesis gas to fuels and chemicals with emphasis on the potential for biomass-derived syngas.* DTIC Document;2003.

8. Hossain MM, de Lasa HI. Chemical-looping combustion (CLC) for inherent separations—a review. *Chemical Engineering Science.* 2008;63(18):4433-4451.

9. Adanez J, Abad A, Garcia-Labiano F, Gayan P, de Diego LF. Progress in Chemical-Looping Combustion and Reforming technologies. *Progress in Energy and Combustion Science.* 2012;38(2):215-282.

10. Zeng L, Luo S, Sridhar D, Fan L-S. Chemical looping processes — particle characterization, ionic diffusion-reaction mechanism and reactor engineering. *Reviews in Chemical Engineering.* Vol 282012:1.

11. Moghtaderi B. Review of the Recent Chemical Looping Process Developments for Novel Energy and Fuel Applications. *Energy & Fuels.* 2012;26(1):15-40.

12. Bhavsar S, Najera M, More A, Veser G. Chapter 7 - Chemical-looping processes for fuel-flexible combustion and fuel production. In: Shi F, ed. *Reactor and Process Design in Sustainable Energy Technology*. Amsterdam: Elsevier; 2014:233-280.

13. Ryden M, Lyngfelt A, Mattisson T. Synthesis gas generation by chemical-looping reforming in a continuously operating laboratory reactor. *Fuel.* 2006;85(12-13):1631-1641.

14. Rydén M, Lyngfelt A, Mattisson T. Chemical-looping combustion and chemical-looping reforming in a circulating fluidized-bed reactor using Ni-based oxygen carriers. *Energy & Fuels.* 2008;22(4):2585-2597.

15. Jin H, Ishida M. Reactivity study on natural-gas-fueled chemical-looping combustion by a fixed-bed reactor. *Industrial & engineering chemistry research.* 2002;41(16):4004-4007.

16. Pröll T, Bolhàr-Nordenkampf J, Kolbitsch P, Hofbauer H. Syngas and a separate nitrogen/argon stream via chemical looping reforming – A 140 kW pilot plant study. *Fuel.* 2010;89(6):1249-1256.

17. Reitmeier RE, Atwood K, Bennett H, Baugh H. Production of Synthetic Gas - Reaction of Light Hydrocarbons with Steam and Carbon Dioxide. *Industrial & Engineering Chemistry.* 1948;40(4):620-626.

18. Wang S, Lu G, Millar GJ. Carbon dioxide reforming of methane to produce synthesis gas over metal-supported catalysts: state of the art. *Energy & Fuels.* 1996;10(4):896-904.

19. Nematollahi B, Rezaei M, Lay EN, Khajenoori M. Thermodynamic analysis of combined reforming process using Gibbs energy minimization method: In view of solid carbon formation. *Journal of Natural Gas Chemistry.* 2012;21(6):694-702.

20. Pakhare D, Spivey J. A review of dry (CO_2) reforming of methane over noble metal catalysts. *Chemical Society Reviews.* 2014;43(22):7813-7837.

21. Rostrup NJ, Inventor; Topsoe Haldor As, assignee. Process for the production of a reforming catalyst. 1974.

22. Kehres J, Jakobsen JG, Andreasen JW, et al. Dynamical properties of a $Ru/MgAl_2O_4$ catalyst during reduction and dry methane reforming. *The Journal of Physical Chemistry C.* 2012;116(40):21407-21415.

23. Jones G, Jakobsen JG, Shim SS, et al. First principles calculations and experimental insight into methane steam reforming over transition metal catalysts. *Journal of Catalysis.* 2008;259(1):147-160.

24. Ferreira-Aparicio P, Marquez-Alvarez C, Rodrıguez-Ramos I, Schuurman Y, Guerrero-Ruiz A, Mirodatos C. A transient kinetic study of the carbon dioxide reforming of methane over supported Ru catalysts. *Journal of Catalysis.* 1999;184(1):202-212.

25. Lewis WK, Gilliland ER, Reed WA. Reaction of Methane with Copper Oxide in a Fluidized Bed. *Industrial & Engineering Chemistry.* 1949;41(6):1227-1237.

26. Najera M, Solunke R, Gardner T, Veser G. Carbon capture and utilization via chemical looping dry reforming. *Chemical Engineering Research and Design.* 2011;89(9):1533-1543.

27. Galvita VV, Poelman H, Detavernier C, Marin GB. Catalyst-assisted chemical looping for CO_2 conversion to CO. *Applied Catalysis B: Environmental.* 2015;164:184-191.

28. Bhavsar S, Najera M, Veser G. Chemical Looping Dry Reforming as Novel, Intensified Process for CO_2 Activation. *Chemical Engineering & Technology.* 2012;35(7):1281-1290.

29. Dharanipragada NA, Buelens LC, Poelman H, De Grave E, Galvita VV, Marin GB. Mg–Fe–Al–O for advanced CO_2 to CO conversion: carbon monoxide yield vs. oxygen storage capacity. *Journal of Materials Chemistry A.* 2015;3(31):16251-16262.

30. Daza YA, Kent RA, Yung MM, Kuhn JN. Carbon Dioxide Conversion by Reverse Water–Gas Shift Chemical Looping on Perovskite-Type Oxides. *Industrial & Engineering Chemistry Research.* 2014;53(14):5828-5837.

31. Lavoie J-M. Review on dry reforming of methane, a potentially more environmentally-friendly approach to the increasing natural gas exploitation. *Frontiers in Chemistry.* 2014;2:81.

32. Rostrup-Nielsen J. Natural Gas: Fuel or Feedstock? In: Derouane E, Parmon V, Lemos F, Ramôa Ribeiro F, eds. *Sustainable Strategies for the Upgrading of Natural Gas: Fundamentals, Challenges, and Opportunities.* Vol 191: Springer Netherlands; 2005:3-24.

33. Rostrup-Nielsen JR, Sehested J, Nørskov JK. Hydrogen and synthesis gas by steam- and C02 reforming. *Advances in Catalysis.* Vol Volume 47: Academic Press; 2002:65-139.

34. Ross JH. Syngas Production Using Carbon Dioxide Reforming: Fundamentals and Perspectives. In: Bhanage BM, Arai M, eds. *Transformation and Utilization of Carbon Dioxide*: Springer Berlin Heidelberg; 2014:131-161.

35. Rostrup-Nielsen JR. New aspects of syngas production and use. *Catalysis Today.* 2000;63(2–4):159-164.

36. Bhavsar S, Najera M, Solunke R, Veser G. Chemical looping: To combustion and beyond. *Catalysis Today.* 2014;228:96-105.

37. Fan LS, Zeng L, Luo S. Chemical-looping technology platform. *AIChE Journal.* 2015;61(1):2-22.

38. Cho P, Mattisson T, Lyngfelt A. Comparison of iron-, nickel-, copper- and manganese-based oxygen carriers for chemical-looping combustion. *Fuel.* 2004;83(9):1215-1225.

39. Zafar Q, Mattisson T, Gevert B. Integrated hydrogen and power production with CO_2 capture using chemical-looping reforming-redox reactivity of particles of CuO, Mn_2O_3, NiO, and Fe_2O_3 using SiO_2 as a support. *Industrial & Engineering Chemistry Research.* 2005;44(10):3485-3496.

40. Bhavsar S, Tackett B, Veser G. Evaluation of iron- and manganese-based mono- and mixed-metallic oxygen carriers for chemical looping combustion. *Fuel.* 2014;136(0):268-279.

41. Bhavsar S, Veser G. Bimetallic Fe–Ni Oxygen Carriers for Chemical Looping Combustion. *Industrial & Engineering Chemistry Research.* 2013;52(44):15342-15352.

42. Bhavsar S, Veser G. Reducible Supports for Ni-based Oxygen Carriers in Chemical Looping Combustion. *Energy & Fuels.* 2013;27(4):2073-2084.

43. Mattisson T, Johansson M, Lyngfelt A. The use of NiO as an oxygen carrier in chemical-looping combustion. *Fuel.* 2006;85(5–6):736-747.

44. Sehested J. Four challenges for nickel steam-reforming catalysts. *Catalysis Today.* 2006;111(1–2):103-110.

45. Vang RT, Honkala K, Dahl S, et al. Controlling the catalytic bond-breaking selectivity of Ni surfaces by step blocking. *Nat Mater.* 2005;4(2):160-162.

46. Bhavsar S, Veser G. Chemical looping beyond combustion: production of synthesis gas via chemical looping partial oxidation of methane. *RSC Advances.* 2014;4(88):47254-47267.

47. Nordhei C, Mathisen K, Safonova O, van Beek W, Nicholson DG. Decomposition of Carbon Dioxide at 500 °C over Reduced Iron, Cobalt, Nickel, and Zinc Ferrites: A Combined XANES−XRD Study. *The Journal of Physical Chemistry C.* 2009;113(45):19568-19577.

48. Kato H, Kodama T, Tsuji M, Tamaura Y, Chang SG. Decomposition of carbon dioxide to carbon by hydrogen-reduced Ni(II)-bearing ferrite. *J Mater Sci.* 1994;29(21):5689-5692.

49. Lin K-S, Adhikari AK, Tsai Z-Y, Chen Y-P, Chien T-T, Tsai H-B. Synthesis and characterization of nickel ferrite nanocatalysts for CO_2 decomposition. *Catalysis Today.* 2011;174(1):88-96.

50. Tamaura Y, Tahata M. Complete reduction of carbon dioxide to carbon using cation-excess magnetite. *Nature.* 1990;346(6281):255-256.

51. Fan L-S, Zeng L, Wang W, Luo S. Chemical looping processes for CO_2 capture and carbonaceous fuel conversion - prospect and opportunity. *Energy & Environmental Science.* 2012;5(6):7254-7280.

52. Linderholm C, Abad A, Mattisson T, Lyngfelt A. 160 h of chemical-looping combustion in a 10 kW reactor system with a NiO-based oxygen carrier. *International Journal of Greenhouse Gas Control.* 2008;2(4):520-530.

53. Kolbitsch P, Bolhàr-Nordenkampf J, Pröll T, Hofbauer H. Operating experience with chemical looping combustion in a 120 kW dual circulating fluidized bed (DCFB) unit. *International Journal of Greenhouse Gas Control.* 2010;4(2):180-185.

54. Adánez J, Gayán P, Celaya J, de Diego LF, García-Labiano F, Abad A. Chemical Looping Combustion in a 10 kW_{th} Prototype Using a CuO/Al_2O_3 Oxygen Carrier: Effect of Operating Conditions on Methane Combustion. *Industrial & Engineering Chemistry Research.* 2006;45(17):6075-6080.

55. Lyngfelt A. Oxygen Carriers for Chemical Looping Combustion-4000 h of Operational Experience. *Oil & Gas Science and Technology–Revue d'IFP Energies nouvelles.* 2011;66(2):161-172.

56. Solunke RD, Veser G. Hydrogen production via chemical looping steam reforming in a periodically operated fixed-bed reactor. *Industrial & Engineering Chemistry Research.* 2010;49(21):11037-11044.

57. More A, Bhavsar S, Veser G. Iron–Nickel Alloys for Carbon Dioxide Activation by Chemical Looping Dry Reforming of Methane. *Energy Technology.* 2016;*10*(14):1147-1157.

58. Garcia-Labiano F, Adánez J, de Diego LF, Gayán P, Abad A. Effect of pressure on the behavior of copper-, iron-, and nickel-based oxygen carriers for chemical-looping combustion. *Energy & Fuels.* 2006;20(1):26-33.

59. Jerndal E, Mattisson T, Lyngfelt A. Thermal Analysis of Chemical-Looping Combustion. *Chemical Engineering Research and Design.* 2006;84(9):795-806.

60. Lyngfelt A. Oxygen carriers for chemical-looping combustion. In: Fennell P, Anthony B, eds. *Calcium and chemical looping technology for power generation and carbon dioxide (CO_2) capture, Woodhead Publishing*: Elsevier; 2015:221-254.

61. Mattisson T, Lyngfelt A, Cho P. The use of iron oxide as an oxygen carrier in chemical-looping combustion of methane with inherent separation of CO_2. *Fuel.* 2001;80(13):1953-1962.

62. Mattisson T, Johansson M, Lyngfelt A. The use of NiO as an oxygen carrier in chemical-looping combustion. *Fuel.* 2006;85(5-6):736-747.

63. Son SR, Kim SD. Chemical-looping combustion with NiO and Fe_2O_3 in a thermobalance and circulating fluidized bed reactor with double loops. *Industrial & engineering chemistry research.* 2006;45(8):2689-2696.

64. Kuo Y-L, Hsu W-M, Chiu P-C, Tseng Y-H, Ku Y. Assessment of redox behavior of nickel ferrite as oxygen carriers for chemical looping process. *Ceramics International.* 2013;39(5):5459-5465.

65. Niu X, Shen L, Jiang S, Gu H, Xiao J. Combustion performance of sewage sludge in chemical looping combustion with bimetallic Cu–Fe oxygen carrier. *Chemical Engineering Journal.* 2016;294:185-192.

66. Evdou A, Zaspalis V, Nalbandian L. Ferrites as redox catalysts for chemical looping processes. *Fuel.* 2016;165:367-378.

67. Fan Y, Siriwardane R. Novel new oxygen carriers for chemical looping combustion of solid fuels. *Energy & Fuels.* 2014;28(3):2248-2257.

68. Qin L, Majumder A, Fan JA, Kopechek D, Fan L-S. Evolution of nanoscale morphology in single and binary metal oxide microparticles during reduction and oxidation processes. *Journal of Materials Chemistry A.* 2014;2(41):17511-17520.

69. Mungse P, Saravanan G, Rayalu S, Labhsetwar N. Mixed Oxides of Iron and Manganese as Potential Low-Cost Oxygen Carriers for Chemical Looping Combustion. *Energy Technology.* 2015;3(8):856-865.

70. Monazam ER, Breault RW, Tian H, Siriwardane R. Reaction Kinetics of Mixed CuO–Fe_2O_3 with Methane as Oxygen Carriers for Chemical Looping Combustion. *Industrial & Engineering Chemistry Research.* 2015;54(48):11966-11974.

71. Johansson M, Mattisson T, Lyngfelt A. Creating a synergy effect by using mixed oxides of iron-and nickel oxides in the combustion of methane in a chemical-looping combustion reactor. *Energy & fuels.* 2006;20(6):2399-2407.

72. Pans MA, Gayán P, Abad A, García-Labiano F, de Diego LF, Adánez J. Use of chemically and physically mixed iron and nickel oxides as oxygen carriers for gas combustion in a CLC process. *Fuel Processing Technology.* 2013;115:152-163.

73. Moghtaderi B, Song H. Reduction Properties of Physically Mixed Metallic Oxide Oxygen Carriers in Chemical Looping Combustion. *Energy & Fuels.* 2010;24(10):5359-5368.

74. Helveg S, Lopez-Cartes C, Sehested J, et al. Atomic-scale imaging of carbon nanofibre growth. *Nature.* 2004;427(6973):426-429.

75. Abild-Pedersen F, Nørskov JK, Rostrup-Nielsen JR, Sehested J, Helveg S. Mechanisms for catalytic carbon nanofiber growth studied by *ab initio* density functional theory calculations. *Physical Review B.* 2006;73(11):115419.

76. Bengaard HS, Nørskov JK, Sehested J, et al. Steam Reforming and Graphite Formation on Ni Catalysts. *Journal of Catalysis.* 2002;209(2):365-384.

77. Helveg S, Sehested J, Rostrup-Nielsen JR. Whisker carbon in perspective. *Catalysis Today.* 2011;178(1):42-46.

78. Hofmann S, Sharma R, Ducati C, et al. *In situ* observations of catalyst dynamics during surface-bound carbon nanotube nucleation. *Nano Letters.* 2007;7(3):602-608.

79. Trovarelli A. Catalytic properties of ceria and CeO2-containing materials. *Catal. Rev.-Sci. Eng.* 1996;38(4):439-520.

80. Kaspar J, Fornasiero P, Hickey N. Automotive catalytic converters: current status and some perspectives. *Catal. Today.* 2003;77(4):419-449.

81. Liang S, Veser G. Mixed Lanthana/Ceria Nanorod-Supported Gold Catalysts for Water–Gas-Shift. *Catal Lett.* 2012;142(8):936-945.

82. Fu Q, Saltsburg H, Flytzani-Stephanopoulos M. Active nonmetallic Au and Pt species on ceria-based water-gas shift catalysts. *Science.* 2003;301(5635):935-938.

83. Pengpanich S, Meeyoo V, Rirksomboon T, Bunyakiat K. Catalytic oxidation of methane over CeO2-ZrO2 mixed oxide solid solution catalysts prepared via urea hydrolysis. *Applied Catalysis A: General.* 2002;234(1–2):221-233.

84. Zhu TL, Flytzani-Stephanopoulos M. Catalytic partial oxidation of methane to synthesis gas over Ni-CeO2. *Appl. Catal. A-Gen.* 2001;208(1-2):403-417.

85. Dong W-S, Jun K-W, Roh H-S, Liu Z-W, Park S-E. Comparative Study on Partial Oxidation of Methane over Ni/ZrO_2, Ni/CeO_2 and Ni/Ce–ZrO_2 Catalysts. *Catal Lett.* 2002;78(1-4):215-222.

86. Vayssilov GN, Lykhach Y, Migani A, et al. Support nanostructure boosts oxygen transfer to catalytically active platinum nanoparticles. *Nature Materials.* 2011;10(4):310-315.

87. Wang XQ, Shen MQ, Wang J, Fabris S. Enhanced Oxygen Buffering by Substitutional and Interstitial Ni Point Defects in Ceria: A First-Principles DFT plus U Study. *J. Phys. Chem. C.* 2010;114(22):10221-10228.

88. Mamontov E, Egami T, Brezny R, Koranne M, Tyagi S. Lattice defects and oxygen storage capacity of nanocrystalline ceria and ceria-zirconia. *J. Phys. Chem. B.* 2000;104(47):11110-11116.

89. Fornasiero P, Balducci G, Di Monte R, et al. Modification of the Redox Behaviour of CeO2Induced by Structural Doping with ZrO_2. *Journal of Catalysis.* 1996;164(1):173-183.

90. Liang S, Broitman E, Wang Y, Cao A, Veser G. Highly stable, mesoporous mixed lanthanum–cerium oxides with tailored structure and reducibility. *J Mater Sci.* 2011;46(9):2928-2937.

91. Hernández WY, Laguna OH, Centeno MA, Odriozola JA. Structural and catalytic properties of lanthanide (La, Eu, Gd) doped ceria. *Journal of Solid State Chemistry.* 2011;184(11):3014-3020.

92. Eguchi K, Setoguchi T, Inoue T, Arai H. Electrical properties of ceria-based oxides and their application to solid oxide fuel cells. *Solid State Ionics.* 1992;52(1):165-172.

93. Inaba H, Tagawa H. Ceria-based solid electrolytes. *Solid State Ionics.* 1996;83(1–2):1-16.

94. Subbarao E, Maiti H. Solid electrolytes with oxygen ion conduction. *Solid State Ionics.* 1984;11(4):317-338.

95. Ou DR, Mori T, Ye F, Zou J, Auchterlonie G, Drennan J. Oxygen-vacancy ordering in lanthanide-doped ceria: Dopant-type dependence and structure model. *Physical Review B.* 2008;77(2):024108.

96. Hedayati A, Azad A-M, Rydén M, Leion H, Mattisson T. Evaluation of Novel Ceria-Supported Metal Oxides As Oxygen Carriers for Chemical-Looping Combustion. *Industrial & Engineering Chemistry Research.* 2012;51(39):12796-12806.

97. Chueh WC, Haile SM. Ceria as a thermochemical reaction medium for selectively generating syngas or methane from H_2O and CO_2. *ChemSusChem.* 2009;2(8):735-739.

98. Li K, Wang H, Wei Y, Yan D. Syngas production from methane and air via a redox process using Ce–Fe mixed oxides as oxygen carriers. *Applied Catalysis B: Environmental.* 2010;97(3–4):361-372.

99. Li K, Wang H, Wei Y, Yan D. Transformation of methane into synthesis gas using the redox property of Ce–Fe mixed oxides: Effect of calcination temperature. *International Journal of Hydrogen Energy.* 2011;36(5):3471-3482.

100. Bhavsar S, Isenberg N, More A, Veser G. Lanthana-doped ceria as active support for oxygen carriers in chemical looping combustion. *Applied Energy.* 2016;168:236-247.

101. Balazs GB, Glass RS. ac impedance studies of rare earth oxide doped ceria. *Solid State Ionics.* 1995;76(1):155-162.

102. Kuharuangrong S. Ionic conductivity of Sm, Gd, Dy and Er-doped ceria. *Journal of Power Sources.* 2007;171(2):506-510.

103. Shannon R. Revised effective ionic radii and systematic studies of interatomic distances in halides and chalcogenides. *Acta Crystallographica Section A.* 1976;32(5):751-767.

104. Ahn K, Yoo DS, Prasad DH, Lee H-W, Chung Y-C, Lee J-H. Role of Multivalent Pr in the Formation and Migration of Oxygen Vacancy in Pr-Doped Ceria: Experimental and First-Principles Investigations. *Chemistry of Materials.* 2012;24(21):4261-4267.

105. Sadykov VA, Frolova YV, Alikina GM, et al. Mobility and reactivity of the lattice oxygen of Pr-doped ceria promoted with Pt. *Reaction Kinetics and Catalysis Letters.* 2005;86(1):21-28.

106. Bernal S, Blanco G, Cauqui M, et al. Oxygen buffering capacity (OBC) of praseodymium-modified CeO_2: influence of the Pr distribution in the ceria host lattice. *Surface and interface analysis.* 2000;30(1):85-89.

107. Mamontov E, Egami T, Brezny R, Koranne M, Tyagi S. Lattice Defects and Oxygen Storage Capacity of Nanocrystalline Ceria and Ceria-Zirconia. *The Journal of Physical Chemistry B.* 2000;104(47):11110-11116.

108. Amin AM, Croiset E, Epling W. Review of methane catalytic cracking for hydrogen production. *International Journal of Hydrogen Energy.* 2011;36(4):2904-2935.

109. Abbas HF, Wan Daud WMA. Hydrogen production by methane decomposition: A review. *International Journal of Hydrogen Energy.* 2010;35(3):1160-1190.

110. Li Y, Li D, Wang G. Methane decomposition to CO_x-free hydrogen and nano-carbon material on group 8–10 base metal catalysts: A review. *Catalysis Today.* 2011;162(1):1-48.

111. Ashik UPM, Wan Daud WMA, Abbas HF. Production of greenhouse gas free hydrogen by thermocatalytic decomposition of methane – A review. *Renewable and Sustainable Energy Reviews.* 2015;44:221-256.

112. Muradov NZ, Veziroğlu TN. From hydrocarbon to hydrogen–carbon to hydrogen economy. *International Journal of Hydrogen Energy.* 2005;30(3):225-237.

113. Takenaka S, Ogihara H, Yamanaka I, Otsuka K. Decomposition of methane over supported-Ni catalysts: effects of the supports on the catalytic lifetime. *Applied Catalysis A: General.* 2001;217(1–2):101-110.

114. Choudhary T, Sivadinarayana C, Chusuei CC, Klinghoffer A, Goodman D. Hydrogen production via catalytic decomposition of methane. *Journal of catalysis.* 2001;199(1):9-18.

115. Zhang T, Amiridis MD. Hydrogen production via the direct cracking of methane over silica-supported nickel catalysts. *Applied Catalysis A: General.* 1998;167(2):161-172.

116. Guo J, Lou H, Zheng X. The deposition of coke from methane on a Ni/MgAl 2 O 4 catalyst. *Carbon.* 2007;45(6):1314-1321.

117. Alstrup I. A new model explaining carbon filament growth on nickel, iron, and Ni□Cu alloy catalysts. *Journal of Catalysis.* 1988;109(2):241-251.

118. Snoeck JW, Froment GF, Fowles M. Steam/CO_2 Reforming of Methane. Carbon Filament Formation by the Boudouard Reaction and Gasification by CO_2, by H_2, and by Steam: Kinetic Study. *Industrial & Engineering Chemistry Research.* 2002;41(17):4252-4265.

119. Shah N, Panjala D, Huffman GP. Hydrogen Production by Catalytic Decomposition of Methane. *Energy & Fuels.* 2001;15(6):1528-1534.

120. Monnerat B, Kiwi-Minsker L, Renken A. Hydrogen production by catalytic cracking of methane over nickel gauze under periodic reactor operation. *Chemical Engineering Science.* 2001;56(2):633-639.

121. Ermakova M, Ermakov DY. Ni/SiO_2 and Fe/SiO_2 catalysts for production of hydrogen and filamentous carbon via methane decomposition. *Catalysis Today.* 2002;77(3):225-235.

122. Takenaka S, Ogihara H, Otsuka K. Structural Change of Ni Species in Ni/SiO_2 Catalyst during Decomposition of Methane. *Journal of Catalysis.* 2002;208(1):54-63.

123. Takenaka S, Kobayashi S, Ogihara H, Otsuka K. Ni/SiO_2 catalyst effective for methane decomposition into hydrogen and carbon nanofiber. *Journal of Catalysis.* 2003;217(1):79-87.

124. Suelves I, Lázaro MJ, Moliner R, Corbella BM, Palacios JM. Hydrogen production by thermo catalytic decomposition of methane on Ni-based catalysts: influence of operating conditions on catalyst deactivation and carbon characteristics. *International Journal of Hydrogen Energy.* 2005;30(15):1555-1567.

125. Suelves I, Lázaro M, Moliner R, Pinilla J, Cubero H. Hydrogen production by methane decarbonization: carbonaceous catalysts. *International journal of hydrogen energy.* 2007;32(15):3320-3326.

126. Serrano D, Botas J, Fierro J, Guil-López R, Pizarro P, Gómez G. Hydrogen production by methane decomposition: origin of the catalytic activity of carbon materials. *Fuel.* 2010;89(6):1241-1248.

127. Pinilla J, Suelves I, Lázaro M, Moliner R. Kinetic study of the thermal decomposition of methane using carbonaceous catalysts. *Chemical Engineering Journal.* 2008;138(1):301-306.

128. Kim MH, Lee EK, Jun JH, et al. Hydrogen production by catalytic decomposition of methane over activated carbons: kinetic study. *International journal of hydrogen energy.* 2004;29(2):187-193.

129. Lee KK, Han GY, Yoon KJ, Lee BK. Thermocatalytic hydrogen production from the methane in a fluidized bed with activated carbon catalyst. *Catalysis Today.* 2004;93–95:81-86.

130. Aiello R, Fiscus JE, zur Loye H-C, Amiridis MD. Hydrogen production via the direct cracking of methane over Ni/SiO_2: catalyst deactivation and regeneration. *Applied Catalysis A: General.* 2000;192(2):227-234.

131. Otsuka K, Takenaka S, Ohtsuki H. Production of pure hydrogen by cyclic decomposition of methane and oxidative elimination of carbon nanofibers on supported-Ni-based catalysts. *Applied Catalysis A: General.* 2004;273(1–2):113-124.

132. Villacampa JI, Royo C, Romeo E, Montoya JA, Del Angel P, Monzón A. Catalytic decomposition of methane over Ni-Al2O3 coprecipitated catalysts: Reaction and regeneration studies. *Applied Catalysis A: General.* 2003;252(2):363-383.

133. Takenaka S, Tomikubo Y, Kato E, Otsuka K. Sequential production of H_2 and CO over supported Ni catalysts. *Fuel.* 2004;83(1):47-57.

134. Li J, Smith KJ. Methane decomposition and catalyst regeneration in a cyclic mode over supported Co and Ni catalysts. *Applied Catalysis A: General.* 2008;349(1):116-124.

135. Pinilla J, Suelves I, Utrilla R, Gálvez M, Lázaro M, Moliner R. Hydrogen production by thermo-catalytic decomposition of methane: regeneration of active carbons using CO 2. *Journal of power sources.* 2007;169(1):103-109.

136. Trovarelli A. Catalytic properties of ceria and CeO_2-containing materials. *Catalysis Reviews.* 1996;38(4):439-520.

137. Kašpar J, Fornasiero P, Hickey N. Automotive catalytic converters: current status and some perspectives. *Catalysis Today.* 2003;77(4):419-449.

138. Farmer JA, Campbell CT. Ceria Maintains Smaller Metal Catalyst Particles by Strong Metal-Support Bonding. *Science.* 2010;329(5994):933-936.

139. Li Y, Zhang B, Tang X, Xu Y, Shen W. Hydrogen production from methane decomposition over Ni/CeO2 catalysts. *Catalysis Communications.* 2006;7(6):380-386.

140. Zapata B, Valenzuela MA, Palacios J, Torres-Garcia E. Effect of Ca, Ce or K oxide addition on the activity of Ni/SiO2 catalysts for the methane decomposition reaction. *International Journal of Hydrogen Energy.* 2010;35(21):12091-12097.

141. Ahmed W, Awadallah AE, Aboul-Enein AA. Ni/CeO_2–Al_2O_3 catalysts for methane thermo-catalytic decomposition to CO_x-free H_2 production. *International Journal of Hydrogen Energy.* 2016;41(41):18484-18493.

142. More A, Veser G. Physical mixtures as simple and efficient alternative to alloy carriers in chemical looping processes. *AIChE Journal.* 2016.

143. Venugopal A, Naveen Kumar S, Ashok J, et al. Hydrogen production by catalytic decomposition of methane over. *International Journal of Hydrogen Energy.* 2007;32(12):1782-1788.

144. Saadi S, Abild-Pedersen F, Helveg S, et al. On the Role of Metal Step-Edges in Graphene Growth. *The Journal of Physical Chemistry C.* 2010;114(25):11221-11227.

145. Snoeck J-W, Froment G, Fowles M. Kinetic study of the carbon filament formation by methane cracking on a nickel catalyst. *Journal of Catalysis.* 1997;169(1):250-262.

146. Helveg S, Hansen PL. Atomic-scale studies of metallic nanocluster catalysts by in situ high-resolution transmission electron microscopy. *Catalysis Today.* 2006;111(1–2):68-73.

147. Toebes ML, Bitter JH, van Dillen AJ, de Jong KP. Impact of the structure and reactivity of nickel particles on the catalytic growth of carbon nanofibers. *Catalysis Today.* 2002;76(1):33-42.

148. Li Y, Zhang B, Xie X, Liu J, Xu Y, Shen W. Novel Ni catalysts for methane decomposition to hydrogen and carbon nanofibers. *Journal of Catalysis.* 2006;238(2):412-424.

149. Chen D, Christensen KO, Ochoa-Fernández E, et al. Synthesis of carbon nanofibers: effects of Ni crystal size during methane decomposition. *Journal of Catalysis.* 2005;229(1):82-96.

150. Nuernberg GDB, Foletto EL, Campos CEM, Fajardo HV, Carreño NLV, Probst LFD. Direct decomposition of methane over Ni catalyst supported in magnesium aluminate. *Journal of Power Sources.* 2012;208:409-414.

151. Amin AM, Croiset E, Constantinou C, Epling W. Methane cracking using Ni supported on porous and non-porous alumina catalysts. *International Journal of Hydrogen Energy.* 2012;37(11):9038-9048.

152. Sanchez M, Gazquez J. Oxygen vacancy model in strong metal-support interaction. *Journal of Catalysis.* 1987;104(1):120-135.

153. Gonzalez-DelaCruz VM, Holgado JP, Pereñíguez R, Caballero A. Morphology changes induced by strong metal–support interaction on a Ni–ceria catalytic system. *Journal of Catalysis.* 2008;257(2):307-314.

154. Caballero A, Holgado JP, Gonzalez-delaCruz VM, Habas SE, Herranz T, Salmeron M. In situ spectroscopic detection of SMSI effect in a Ni/CeO_2 system: hydrogen-induced burial and dig out of metallic nickel. *Chemical Communications.* 2010;46(7):1097-1099.

155. Beebe Jr TP, Goodman DW, Kay BD, Yates Jr JT. Kinetics of the activated dissociative adsorption of methane on the low index planes of nickel single crystal surfaces. *The Journal of chemical physics.* 1987;87(4):2305-2315.

156. Li Y, Liu Q, Shen W. Morphology-dependent nanocatalysis: metal particles. *Dalton transactions.* 2011;40(22):5811-5826.

157. Barrault J, Alouche A, Paul-Boncour V, Hilaire L, Percheron-Guegan A. Influence of the support on the catalytic properties of nickel/ceria in carbon monoxide and benzene hydrogenation. *Applied Catalysis.* 1989;46(2):269-279.

158. Sharma S, Hilaire S, Vohs J, Gorte R, Jen H-W. Evidence for oxidation of ceria by CO 2. *Journal of Catalysis.* 2000;190(1):199-204.

159. Sholl DS, Lively RP. Seven chemical separations to change the world. *Nature.* 2016;532(7600):435-437.

160. Ferrando R, Jellinek J, Johnston RL. Nanoalloys: From Theory to Applications of Alloy Clusters and Nanoparticles. *Chemical Reviews.* 2008;108(3):845-910.

161. Sankar M, Dimitratos N, Miedziak PJ, Wells PP, Kiely CJ, Hutchings GJ. Designing bimetallic catalysts for a green and sustainable future. *Chemical Society Reviews.* 2012;41(24):8099-8139.

162. Greeley J, Mavrikakis M. Alloy catalysts designed from first principles. *Nat Mater.* 2004;3(11):810-815.

163. Paull DH, Abraham CJ, Scerba MT, Alden-Danforth E, Lectka T. Bifunctional asymmetric catalysis: Cooperative Lewis acid/base systems. *Accounts of chemical research.* 2008;41(5):655-663.

164. Shibasaki M, Kanai M, Matsunaga S, Kumagai N. Recent progress in asymmetric bifunctional catalysis using multimetallic systems. *Accounts of chemical research.* 2009;42(8):1117-1127.

165. Jiao F, Li J, Pan X, et al. Selective conversion of syngas to light olefins. *Science.* 2016;351(6277):1065-1068.

166. Yang G, Tsubaki N, Shamoto J, Yoneyama Y, Zhang Y. Confinement Effect and Synergistic Function of H-ZSM-5/Cu-ZnO-Al2O3 Capsule Catalyst for One-Step Controlled Synthesis. *Journal of the American Chemical Society.* 2010;132(23):8129-8136.

167. Wiessner FG. Basics and industrial applications of pressure swing adsorption (PSA), the modern way to separate gas. *Gas Separation & Purification.* 1988;2(3):115-119.

168. Baker RW. Future Directions of Membrane Gas Separation Technology. *Industrial & Engineering Chemistry Research.* 2002;41(6):1393-1411.

169. Rambeau G, Amariglio H. Improvement of the catalytic performance of a ruthenium powder in ammonia synthesis by the use of a cyclic procedure. *Applied Catalysis.* 1981;1(5):291-302.

170. Silveston P, Hudgins R, Adesina A, Ross G, Feimer J. Activity and selectivity control through periodic composition forcing over Fischer-Tropsch catalysts. *Chemical engineering science.* 1986;41(4):923-928.

171. Silveston PL, Forissier M. Influence of composition modulation on product yields and selectivity in the partial oxidation of propylene over an antimony-tin oxide catalyst. *Industrial & Engineering Chemistry Process Design and Development.* 1985;24(2):320-325.

172. Ilinich O, Ruettinger W, Liu X, Farrauto R. Cu–Al_2O_3–$CuAl_2O_4$ water–gas shift catalyst for hydrogen production in fuel cell applications: mechanism of deactivation under start–stop operating conditions. *Journal of Catalysis.* 2007;247(1):112-118.

173. Matros YS, BUNIMOVICH GA. Reverse-flow operation in fixed bed catalytic reactors. *Catalysis Reviews.* 1996;38(1):1-68.

174. Contractor RM. Dupont's CFB technology for maleic anhydride. *Chemical Engineering Science.* 1999;54(22):5627-5632.

175. Tong A, Bayham S, Kathe MV, Zeng L, Luo S, Fan L-S. Iron-based syngas chemical looping process and coal-direct chemical looping process development at Ohio State University. *Applied Energy.* 2014;113:1836-1845.

176. Ströhle J, Orth M, Epple B. Design and operation of a 1 MWth chemical looping plant. *Applied Energy.* 2014;113:1490-1495.

177. Gaur S, Haynes DJ, Spivey JJ. Rh, Ni, and Ca substituted pyrochlore catalysts for dry reforming of methane. *Applied Catalysis A: General.* 2011;403(1–2):142-151.

178. Gandhi H, Graham G, McCabe RW. Automotive exhaust catalysis. *Journal of Catalysis.* 2003;216(1):433-442.

179. Gorte RJ. Ceria in catalysis: from automotive applications to the water–gas shift reaction. *AIChE journal.* 2010;56(5):1126-1135.

180. Gorte R, Zhao S. Studies of the water-gas-shift reaction with ceria-supported precious metals. *Catalysis Today.* 2005;104(1):18-24.

181. Ratnasamy C, Wagner JP. Water gas shift catalysis. *Catalysis Reviews.* 2009;51(3):325-440.

182. Shao Z, Haile SM. A high-performance cathode for the next generation of solid-oxide fuel cells. *Nature.* 2004;431(7005):170-173.

183. Ghenciu AF. Review of fuel processing catalysts for hydrogen production in PEM fuel cell systems. *Current opinion in solid state and materials science.* 2002;6(5):389-399.

184. Karakoti A, Monteiro-Riviere N, Aggarwal R, et al. Nanoceria as antioxidant: synthesis and biomedical applications. *Jom.* 2008;60(3):33-37.

185. Zhong L-S, Hu J-S, Cao A-M, Liu Q, Song W-G, Wan L-J. 3D flowerlike ceria micro/nanocomposite structure and its application for water treatment and CO removal. *Chemistry of Materials.* 2007;19(7):1648-1655.

186. Cao C-Y, Cui Z-M, Chen C-Q, Song W-G, Cai W. Ceria hollow nanospheres produced by a template-free microwave-assisted hydrothermal method for heavy metal ion removal and catalysis. *The Journal of Physical Chemistry C.* 2010;114(21):9865-9870.

187. Kim CK, Kim T, Choi IY, et al. Ceria nanoparticles that can protect against ischemic stroke. *Angewandte Chemie International Edition.* 2012;51(44):11039-11043.

188. Tuller HL. Ionic conduction in nanocrystalline materials. *Solid State Ionics.* 2000;131(1–2):143-157.

189. Taniguchi T, Katsumata K-i, Omata S, Okada K, Matsushita N. Tuning Growth Modes of Ceria-Based Nanocubes by a Hydrothermal Method. *Crystal Growth & Design.* 2011;11(9):3754-3760.

190. Lin M, Fu ZY, Tan HR, Tan JPY, Ng SC, Teo E. Hydrothermal Synthesis of CeO_2 Nanocrystals: Ostwald Ripening or Oriented Attachment? *Crystal Growth & Design.* 2012;12(6):3296-3303.

191. Mai H-X, Sun L-D, Zhang Y-W, et al. Shape-Selective Synthesis and Oxygen Storage Behavior of Ceria Nanopolyhedra, Nanorods, and Nanocubes. *The Journal of Physical Chemistry B.* 2005;109(51):24380-24385.

192. Liang X, Wang X, Zhuang Y, Xu B, Kuang S, Li Y. Formation of CeO2−ZrO2 Solid Solution Nanocages with Controllable Structures via Kirkendall Effect. *Journal of the American Chemical Society.* 2008;130(9):2736-2737.

193. Gellrich T. *Shale gas Reshaping the US chemicals industry.* 2012.

194. Zhu Q, Wegener SL, Xie C, Uche O, Neurock M, Marks TJ. Sulfur as a selective ‘soft’oxidant for catalytic methane conversion probed by experiment and theory. *Nature chemistry.* 2013;5(2):104-109.

195. Peter M, Marks TJ. Platinum Metal-Free Catalysts for Selective Soft Oxidative Methane → Ethylene Coupling. Scope and Mechanistic Observations. *Journal of the American Chemical Society.* 2015;137(48):15234-15240.

196. Mangnus P, Poels E, Van Langeveld A, Moulijn J. Comparison of the sulfiding rate and mechanism of supported NiO and Ni^o particles. *Journal of Catalysis.* 1992;137(1):92-101.

197. Reshetenko T, Khairulin S, Ismagilov Z, Kuznetsov V. Study of the reaction of high-temperature H_2S decomposition on metal oxides (γ-Al_2O_3, α-Fe_2O_3, V_2O_5). *International journal of hydrogen energy.* 2002;27(4):387-394.

198. Westmoreland PR, Gibson JB, Harrison DP. Comparative kinetics of high-temperature reaction between hydrogen sulfide and selected metal oxides. *Environmental Science & Technology.* 1977;11(5):488-491.

199. Solunke RD, Veser G. Integrating desulfurization with CO_2-capture in chemical-looping combustion. *Fuel.* 2011;90(2):608-617.

200. Tian H, Simonyi T, Poston J, Siriwardane R. Effect of Hydrogen Sulfide on Chemical Looping Combustion of Coal-Derived Synthesis Gas over Bentonite-Supported Metal−Oxide Oxygen Carriers. *Industrial & Engineering Chemistry Research.* 2009;48(18):8418-8430.

201. Nehb W, Vydra K. Sulfur. *Ullmann's Encyclopedia of Industrial Chemistry*: Wiley-VCH Verlag GmbH & Co. KGaA; 2000.

202. Stöber W, Fink A, Bohn E. Controlled growth of monodisperse silica spheres in the micron size range. *Journal of colloid and interface science.* 1968;26(1):62-69.

203. Zhang W, Yang L-P, Wu Z-X, Piao J-Y, Cao A-M, Wan L-J. Controlled formation of uniform CeO_2 nanoshells in a buffer solution. *Chemical Communications.* 2016;52(7):1420-1423.

204. Strandwitz NC, Stucky GD. Hollow microporous cerium oxide spheres templated by colloidal silica. *Chemistry of Materials.* 2009;21(19):4577-4582.